
**Simulated Holocene climate variability:
insights from the long-term ocean
circulation and the Caribbean climate**

Dissertation

submitted to

Department of Physics/Electrical Engineering,

University of Bremen

for the degree of

Doctor of Natural Sciences

By

Wei Wei

Bremen, July 2011

Supervisor: **Prof. Dr. Gerrit Lohmann**

Alfred Wegener Institute for Polar and Marine Research,
Bremerhaven, and Department of Physics/Electrical Engineering,
University of Bremen

Referees: **Prof. Dr. Gerrit Lohmann**

Alfred Wegener Institute for Polar and Marine Research,
Bremerhaven, and Department of Physics/Electrical Engineering,
University of Bremen

Prof. Dr. Michael Schulz

MARUM - Center for Marine Environmental Sciences, and
Faculty of Geosciences, University of Bremen

*The biggest thrill in life is making scientific
breakthroughs. No other reward can compare
with that satisfaction.*

--by John Craig Venter

Acknowledgements

I would like first to sincerely appreciate my supervisor Prof. Dr. Gerrit Lohmann, giving me the opportunity to undertake this PhD project. Thank you for always supporting me and advising me throughout my PhD study.

The Deutsche Forschungsgemeinschaft (DFG) under the Special Priority Programme INTERDYNAMIK is acknowledged for funding this research. Special thank goes to Prof. Dr. Michael Schulz for reviewing this dissertation.

This study is also a contribution to the "Earth System Science Research School (ESSReS)", an initiative of the Helmholtz Association of German research centres (HGF) at the Alfred Wegener Institute for Polar and Marine Research. I would like to thank Dr. Klaus Grosfeld for organizing helpful lectures and soft-skill trainings during the last three years, which expand my knowledge in the Earth system science and enable me to improve my scientific performance.

I am greatly thankful to my colleagues Dr. Martin Werner, Dr. Grogor Knorr, Dr. Petra Langebroek and Xu Xu, who are always ready to answer the technical problems I met, Prof. Dr. Mihai Dima for the fruitful discussion and the collaboration on the publication, Dr. Monica Ionita-Scholz, Dr. Thomas Lapple and Dr. Norel Rimbu for their great help with the statistic methods and software, and all the other colleagues in Paleoclimate Dynamics group, at AWI, without your accompany, my PhD study will not be as joyful and successful as it is.

Many thanks go to Dr. Thomas Felis, Dr. Cyril Ciry and Dr. Claudia Fensterer for the wonderful collaboration and fruitful discussion in the framework of the CaribClim project from INTERDYNAMIK.

I would also like to thank all the Chinese colleagues and friends, working at AWI. Sharing the life in Bremerhaven with you makes me feel at home.

在此我要感谢我的父母和祖父母，您们在我的成长过程和早年的教育中倾注了全部的精力。谨以此文献给仙逝的祖父，您是我从事科研工作的启蒙老师。

Abstract

Climate variability during the Holocene has become a hot spot in the frame of the paleoclimate research. The relatively stable background climate condition in this period enables us to gain more knowledge for the present climate, by a better comprehension of the internal variability of the climate system. Contemporarily, understanding of the long-term climate change during the Holocene, attributed to the external forcing, can assist us to better constrain the prediction of future climate change. Climate modeling studies, with the advantage of high resolution in both spatial and temporal, can supply essential information for the physical mechanisms involved in each process and thus contribute to such an effort, which cannot be achieved only by proxy data.

Several long-term simulations for the different Holocene periods have been performed with the coupled general circulation model COSMOS. Comparison among the simulations reveals that change in the orbital forcing is the primary factor that drives the climate evolution during the Holocene. The most intriguing feature is that the seasonality is increased significantly over the North Hemisphere, in particular the mid-high latitude. Even over the low latitude, e.g. the Caribbean region, such a change can result in approximately 1°C stronger seasonality in the sea surface temperature of the Caribbean Sea, supported by coral based reconstruction. Existence of the Laurentide ice sheet (LIS) and its melting have strong cooling effect on the regional scale. This influence can be extended globally by ocean-atmosphere circulation. Large amount of water trapped by the LIS, together with the orbital induced movement of the Intertropical Convergence Zone, cause a shift in fractionation of the water isotope from early to mid-Holocene, observed in different proxy records. The ocean circulation is greatly modulated by these forcing, with decreased by more than 2 Sv during the mid-Holocene due to the orbital forcing and further weakened by freshwater injection from the LIS melting during the early Holocene.

Although the external induced climate mean states exhibit distinct global and regional features, the internal variability of the climate system shows no remarkable change during the Holocene. The Atlantic Multidecadal Oscillation, associated with the long-term variation in the Atlantic meridional overturning circulation, has a similar quasi periodicity of 50-80 years in each simulation as indicated by observation. Another long-term variation in the global meridional overturning circulation, associated with the Southern Hemisphere westerly winds, demonstrate a similar pattern in both pre-industrial and mid-Holocene conditions. On shorter time scales, the El Niño-Southern Oscillation and North Atlantic Oscillation, indentified as the major forcing mechanisms controlling the seasonal and interannual variability of the Caribbean climate, show a common feature during the Holocene as found in the present-day studies. However, the climate influence of these phenomena could vary in the magnitude and regional scale under different background climate conditions. The results suggest that a larger fluctuation in the mean climate induced by the external forcing might amplify the influence of the internal variability, and eventually add it to the mean climate as a positive feedback.

Table of contents

1. Introduction	1
2. Data and model setup	7
2.1 Instrumental data	7
2.2 Model description and experimental setup	8
2.2.1 Coupled model description	8
2.2.2 Water isotope simulation setup	13
2.3 Proxy data	14
3. Simulated Atlantic Multidecadal Oscillation during the Holocene	 17
3.1 Introduction	17
3.2 Mean climate during the Holocene	19
3.3 Periodicity of the AMO indices	24
3.4 Spatial patterns of the temperature and AMOC associated with the AMO28	
3.5 Climate influence of the AMO	31
3.6 Discussion and summary	34
4. Distinct modes of internal variability in the Global Meridional Overturning Circulation associated with the Southern Hemisphere westerly winds	 35
4.1 Introduction	35
4.2 Data and Methods	38
4.3 Results	39
4.3.1 Mean state of the GMOC and AMOC	39
4.3.2 Global modes of the overturning circulation	41

4.3.3 Wind perturbation experiments.....	45
4.3.4 The SO mode and the NH mode.....	47
4.3.5 Response of the SST and the sea ice to different modes.....	52
4.4 Discussion.....	53
4.5 Conclusions.....	58
5. Caribbean climate variation during the Holocene.....	59
5.1 The Caribbean climatology during the Holocene.....	59
5.1.1 Caribbean climatology in the present.....	60
5.1.2 The Caribbean climatology during the mid-Holocene.....	71
5.1.3 The Caribbean climatology during the early Holocene.....	78
5.2 The Caribbean climate variability during the Holocene.....	89
5.2.1 Seasonal and interannual variability.....	90
5.2.2 Decadal to centennial variability.....	108
5.3 Summary.....	109
6. Conclusions and future perspectives.....	111
Reference.....	115

1. Introduction

The Holocene, a geological epoch which starts from about 11.7 kyr before present (BP) and last to the present or pre-industrial time, is often referred as a relatively climatically stable period [Dansgaard *et al.*, 1993]. However, like any other geological epochs, the climate during the Holocene displays considerable fluctuations and varies in different ways.

Generally, the Holocene is subdivided into three periods, although there are more chronostratigraphic terms proposed for the subdivision, which cannot apply to represent the global scale climate evolution [Wanner *et al.*, 2008]. The first period lasts from 11.7 to 9 kyr BP, coinciding with the Preboreal and Boreal chronozones. The second period coincides with the Atlantic chronozone, also called Alti- or Hypsithermal or Holocene climate optimum, covering the time from 9 to 6 kyr BP. It is followed by Neoglacial, coinciding with the Subboreal and Subatlantic chronozones. This third period lasted from about 5-6 kyr BP to the present or pre-industrial time [Wanner *et al.*, 2008].

The forcing factors that control the evolution of the climate during the Holocene involve external forcing and internal variability of the climate system. Orbital forcing, solar forcing, volcanic forcing, land cover change forcing and greenhouse gas forcing are contributed to the external forcing [Wanner *et al.*, 2008]. For each period of the Holocene, the climate condition is dominated by different forcing, which has been taken as the main factor for the Holocene subdivision. In a global scale, the orbital forcing dominates the whole Holocene climate evolution. The orbital-induced high summer insolation in the North Hemisphere (NH) reaches a maximum around 11 kyr BP (Figure 1.1), due to a coincidence of the precession and obliquity cycles [Wanner *et al.*, 2008].

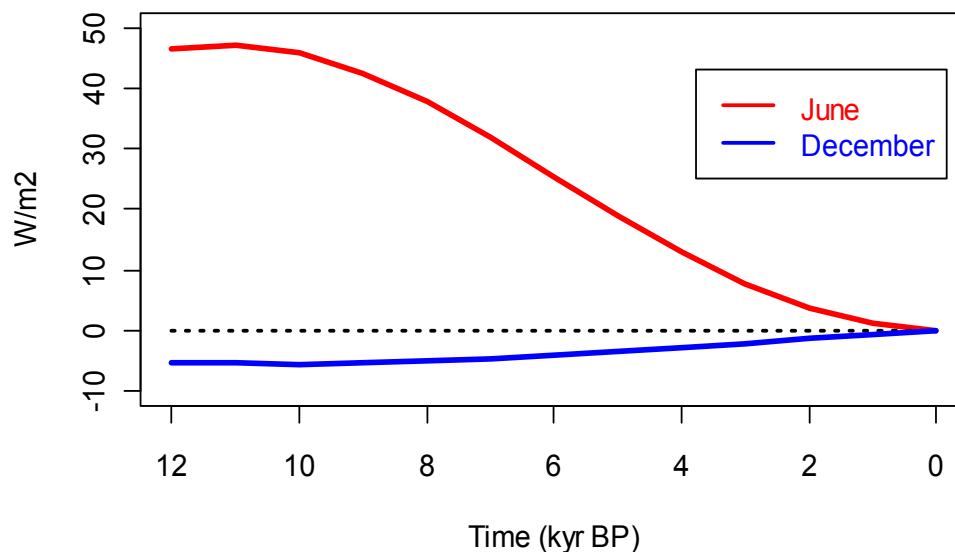


Figure 1.1 Orbital forced insolation at 60°N [Berger, 1978] for June and December during the Holocene.

However, the spatial and temporal pattern of the Holocene thermal maximum is quite different over the NH, caused by the existing of the Laurentide ice sheet (LIS; Figure 2.1) and the climate influence of its melting [Renssen *et al.*, 2009]. This early Holocene ice sheet has not only a strong local cooling effect, which can overcompensate the warming resulting from more insolation, but even large influence in the high-latitude Southern Hemisphere through oceanic teleconnection [Renssen *et al.*, 2010]. Melting of the LIS contributes approximately 50m sea level change during the last 10 kyr (Figure 1.2), which in turn could also generate considerable influence on the Holocene climate evolution. The last remnants of the LIS vanishes around 7 kyr BP [Carlson *et al.*, 2008], followed by a period with more summer insolation over the NH high latitudes. With the NH high-latitude insolation decreasing afterward, a cooling trend covers most of the NH mid-high latitude [S J Lorenz *et al.*, 2006] until the anthropogenic CO₂ release induced warming after the pre-industrial time.

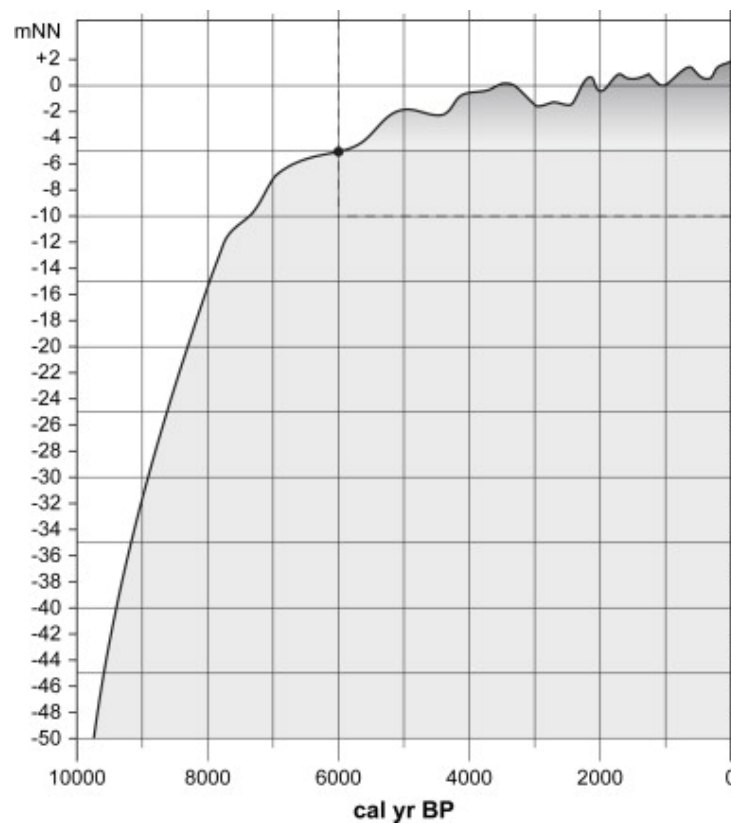


Figure 1.2 Sea level changes in the area of the southern North Sea over the last 10 kyr. Figure adapted from Wanner et al. [2008], which has been modified after Berhe [2003].

Change in the greenhouse gas concentration (Figure 1.3) has a slightly warming trend during the Holocene, but its magnitude is rather insignificant compared with the orbital induced climate change [e.g. *Renssen et al.*, 2009].

The solar forcing is important for the investigation to the short timescale climate variability. However, the physical process that links the solar activity and solar forcing is still unclear, and knowledge of the past solar activity can be only obtained from the proxy data [*Wanner et al.*, 2008]. The volcanic forcing can have incredible regional or even global-scale climate influence after the explosion. But it happens only very occasionally, and its climate influence on the Holocene climate evolution on longer timescales is relatively negligible compared with the other forcing factors.

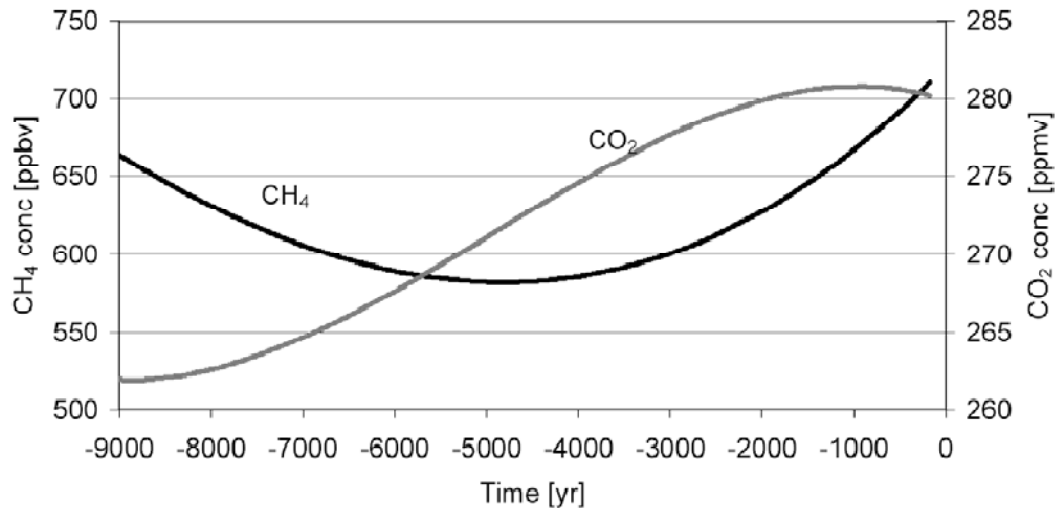


Figure 1.3 Greenhouse gas concentration over the last 9 kyr based on the ice-core measurement [Raynaud *et al.*, 2000]. Figure adapted from Renssen *et al.* [2009].

The relative stable background climate condition during the Holocene, in particular its late part, provides us the fundamental requirement to understand the internal variability of climate system, which is highly important to constrain the underlying anthropogenic climate change.

The well known internal variability associated phenomena under the present-day climate condition include the El Niño-Southern Oscillation (ENSO), the North Atlantic Oscillation (NAO), the Antarctic Oscillation (AO) or the Southern Annual Mode (SAM), the Tropical Atlantic Variation (TAV), the Atlantic Multidecadal Oscillation (AMO), variation related to the ocean meridional overturning circulation (MOC) and so on, ranging from seasonal and interannual to decadal and centennial timescales. They can have distinct climate impact on global and regional scales. Previous studies based on proxy data [e.g. *A. C. Clement et al.*, 2000; *Moy et al.*, 2002; *Rimbu et al.*, 2003; *G. Lohmann et al.*, 2005; *Knudsen et al.*, 2011] have demonstrated that these phenomena undergo some trend during the Holocene, induced by the different background climate. However, it is difficult to examine the possible feedback as climate influence due to the relative coarse temporal or spatial resolution of the proxy records. Modeling studies, on the other hand, can provide an alternative approach to solve this problem and, at the same time, help us to gain more

comprehensive understanding of the physical mechanisms behind each phenomenon. In this study, several numerical experiments are conducted using the coupled general circulation models COSMOS, with proper boundary conditions prescribed for different Holocene periods. Both external and internal induced variability on global and regional scales are examined. The detailed experiment setup will be given in Chapter 2, together with a short introduction of instrumental data and proxy data used in this study. In Chapter 3, the global features of the mean climate state under each Holocene period will be presented. Special focus on the AMO and its climate influence during the Holocene enables us to give some hint for a better prediction of this phenomenon in the future. Chapter 4 discusses the distinct modes of internal variability in the global meridional overturning circulation, which are found to be associated with the Southern Hemisphere westerly winds on multidecadal and centennial timescales. Chapter 5 elaborates the forcing mechanisms of seasonality and interannual to centennial climate variability in the Caribbean region during the Holocene, based on model-proxy data comparison. Conclusion and outlook will finally be given in Chapter 6.

2. Data and model setup

2.1 Instrumental data

The spatial and temporal variability of the surface air temperature and winds are represented by NCEP/NCAR reanalysis monthly mean dataset, which uses a state-of-the-art analysis/forecast system to perform data assimilation using past data from 1948 to the present [Kalnay *et al.*, 1996]. The spatial resolution of the dataset is $2.5^{\circ} \times 2.5^{\circ}$.

The Hadley Center Sea Ice and Sea Surface Temperature data set (HadISST) [Rayner *et al.*, 2006], taken from the Met Office Marine Data Bank (MDB), is analyzed to characterize the variability of the sea surface temperature (SST). It replaces the Global Sea Ice and Sea Surface Temperature (GISST) data sets, and is a unique combination of monthly globally-complete fields of SST and sea ice concentration on a $1^{\circ} \times 1^{\circ}$ latitude-longitude grid from 1870 to 2010.

We use two datasets for the precipitation analyses in this study. One is the monthly CPC Merged Analysis of Precipitation (CMAP) data set [Xie and Arkin, 1997], which consists of two files containing monthly averaged precipitation rate values. Values are obtained from 5 kinds of satellite estimates (GPI, OPI, SSM/I scattering, SSM/I emission and MSU). The other is taken from the Hulme Monthly Precipitation based on the Climatic Research Unit (CRU) data set [Hulme *et al.*, 1998], which has been constructed based on the station data set from an extension of the original CRU/US DOE data described in Eischeid *et al.* [1991]. For the $2.5^{\circ} \times 3.75^{\circ}$ resolution version of this dataset, a total of 1520 gridboxes possessed time series of which 726 had complete data between 1900 and 1998, by merging two gridded datasets.

For the sea level pressure, we use the Kaplan's SLP data set [Kaplan *et al.*, 2000], which is derived from the global sea level pressure (SLP) record of COADS averaged on $4^{\circ} \times 4^{\circ}$ grid by applying reduced space optimal interpolation procedure. The data covers the period from 1854 to 1992.

The vertical integrated water vapor transport (WVT) for the period 1962-2000 are calculated by Ionita et al. [2008] using zonal wind, meridional wind and specific humidity, which are generated from the NCEP/NCAR model in a resolution of $2.5^{\circ} \times 2.5^{\circ}$ [Kalnay et al., 1996].

All the datasets used in this study are summarized in Table 2.1.

Table 2.1 Datasets used in this study

Variable	Dataset	Reference
surface air temperature	NCEP/NCAR reanalysis	Kalnay et al. 1996
surface wind	NCEP/NCAR reanalysis	Kalnay et al. 1996
sea surface temperature	HadISST	Rayner et al. 2006
precipitation	NCEP/NCAR reanalysis	Kalnay et al. 1996
	Hulme CRU	Hulme et al. 1998
sea level pressure	Kaplan	Kaplan et al. 2000
water vapor transport	NCEP/NCAR reanalysis	Ionita et al. 2008

2.2 Model description and experimental setup

2.2.1 Coupled model description

In this study, we use the coupled general circulation model (CGCM) -Community Earth System Models (COSMOS) developed by the Max-Planck-Institute for Meteorology that describes the dynamics of the atmosphere-ocean-sea ice-vegetation system. The atmospheric component is the spectral atmosphere model ECHAM5 [Roeckner et al., 2003] with the resolution of T31, corresponding to $3.75^{\circ} \times 3.75^{\circ}$ in horizontal, and 19 hybrid sigma pressure level in vertical. The land processes are integrated into the atmosphere model using the land surface model JSBACH [Raddatz et al., 2007] except for river routing, for which the hydrological discharge model is responsible [Hagemann and Dümenil, 1998; Hagemann and Gates, 2003]. The

ocean-sea ice component is the ocean general circulation model MPI-OM [Marshall *et al.*, 2003] with the resolution of GR30 in horizontal and 40 unevenly spaced vertical levels, which includes the dynamics of sea ice formulated using viscous-plastic rheology [Hibler III, 1979]. An orthogonal curvilinear grid allows for an arbitrary placement of the grid poles in the ocean model. In our setup, the North Pole is shifted to Greenland, and the South Pole to the center of the Antarctic continent. The effect of mixing by advection with the unresolved mesoscale eddies is parameterized after Gent *et al.* [1995]. The atmosphere and the ocean components interact through the OASIS3 coupler [Valcke, 2006].

2.2.1.1 Holocene experiments setup

Several long-term timeslice experiments are performed: a pre-industrial control experiment CTL, a mid-Holocene one H6K (i.e. 6 kilo years before 1950 AD, short for 6ka BP) and three different early-Holocene runs (i.e. 9 kilo years before 1950 AD, short for 9ka BP), by prescribing the appropriate boundary conditions (Table 2.2). Orbital parameters are calculated according to Berger [1978]. In CTL and H6K experiments, the GHGs are prescribed according to Paleoclimate Modeling Intercomparison Project (PMIP) [Crucifix *et al.*, 2005]. For the early-Holocene experiments, the GHGs are taken from the ice core measurement [Indermühle *et al.*, 1999; Brook *et al.*, 2000; Sowers *et al.*, 2003]. Compared to the H9KO experiment, H9KT and H9KM experiments use the orography at 9ka BP based on the ICE-5G(VM2) dataset [Peltier, 2004], where the global mean sea level height in 9 kyr BP is approximately 30 meters lower than that under the present-day condition, and also include the Laurentide ice sheet (LIS) (Figure 2.1) and its feedback, e.g. albedo. In H9KM experiment, we additionally prescribed a freshwater forcing describing the LIS background meltflux by adding 0.09 Sv ($1 \text{ Sv} = 1 \times 10^6 \text{ m}^3/\text{s}$) [Licciardi *et al.*, 1999] freshwater into the North Atlantic ocean between 40° N and 60° N .

The atmospheric model is initialized by the mean climatology from an AMIP

(Atmospheric Model Intercomparison Project)-style experiment, which is performed using observed monthly sea surface temperatures and sea-ice cover for the time period 1978-1999 [Roeckner *et al.*, 2004]. The ocean model is initialized using the Ocean Model Intercomparison Project (OMIP) forcing, which is derived from the European Centre for Medium-Range Weather Forecasts (ECMWF) reanalysis dataset [Gibson *et al.*, 1997]. Each experiment is run for 1000 years to reach the equilibrium and further integrated for 2000 years. Once the runs are initiated, no changes are permitted to the forcing. Consequently, all the simulated climatic fluctuations are generated by internal climate variability in the coupled system.

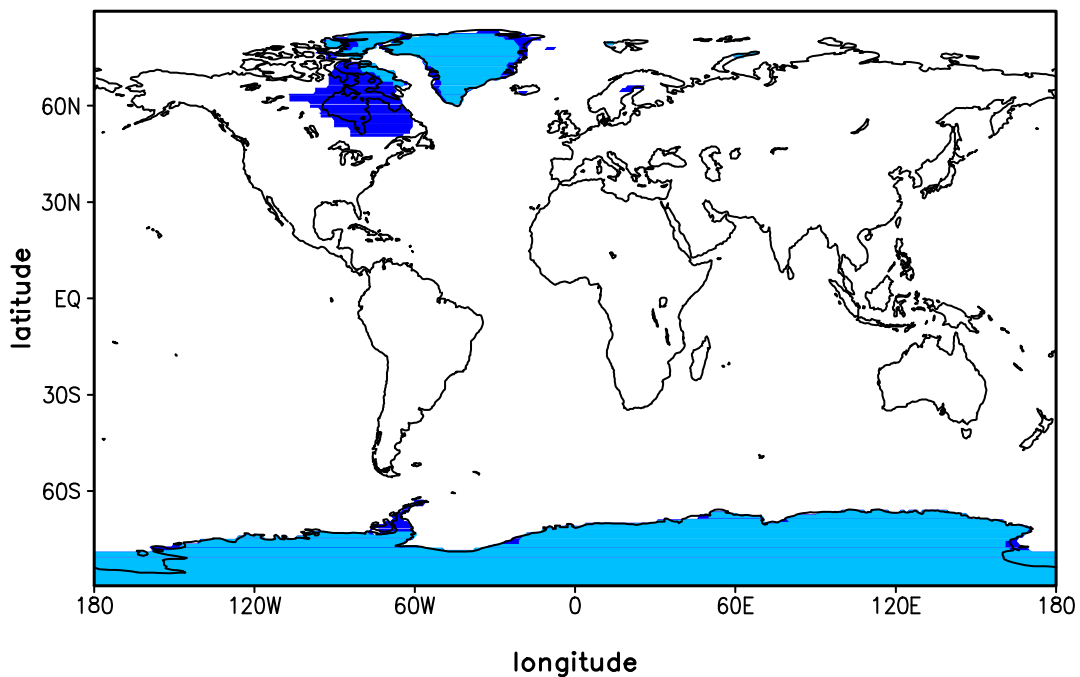


Figure 2.1 The ice sheet coverage used in the simulation. Light blue represents the ice sheet coverage in the present-day condition; dark blue is the ice sheet coverage anomaly in 9ka BP, prescribed in experiments H9KT and H9KM.

Table 2.2 Boundary conditions used in the timeslice experiments.

Experiment	Boundary conditions					
	Orbital	Greenhouse gases			Orography	Meltflux (Sv)
		CO ₂ (ppm)	CH ₄ (ppb)	N ₂ O (ppb)		
CTL	Present	280	760	270	Present	0
H6K	6 ka BP		650			
H9KO	9ka BP	265	700	245	Present	0
H9KT					9ka BP	
H9KM						0.09

2.2.1.2 Wind perturbation experiment setup

To support our findings in section 4.1.1, we additionally perform three wind perturbation experiments to support our hypotheses by modifying the magnitude and position of the Southern Hemisphere westerly wind (SWW) stress in the ocean model. In the CTL experiment, the zonal averaged wind stress maximum is located near 50°S (Figure 2.2), which is consistent with most GCMs and observation data [e.g. *Fyfe and Saenko, 2006*]. For our SWW perturbation experiments, the wind stress anomalies are applied in the latitude bands between 30°S and 70°S, through an amplification of a 1.5 times of the CTL wind stress in the experiment $W_{x1.5}$, through a two ocean-grid points (approximately 3.5°) southward shift in the experiment W_{PLWD} , and through both these changes in the experiment $W_{PLWDx1.5}$ (Figure 2.2). Here, the wind stress anomalies are applied only to the ocean surface where there is water but not sea ice. The atmosphere is not directly influenced by this change. However, some feedback between the atmosphere and the ocean cannot be precluded after the perturbation, which might have impact on the air-sea heat flux and moisture transport in the atmosphere. The boundary conditions for orbital parameters and greenhouse gases in these wind perturbation experiments are identical with CTL. To guarantee that the

atmosphere and the ocean, especially in the NH, experience the feedback from any change in the SWW stress, each perturbation experiment is integrated for 600 years, with continuous perturbation starting from the last year of the 3000-year CTL experiment.

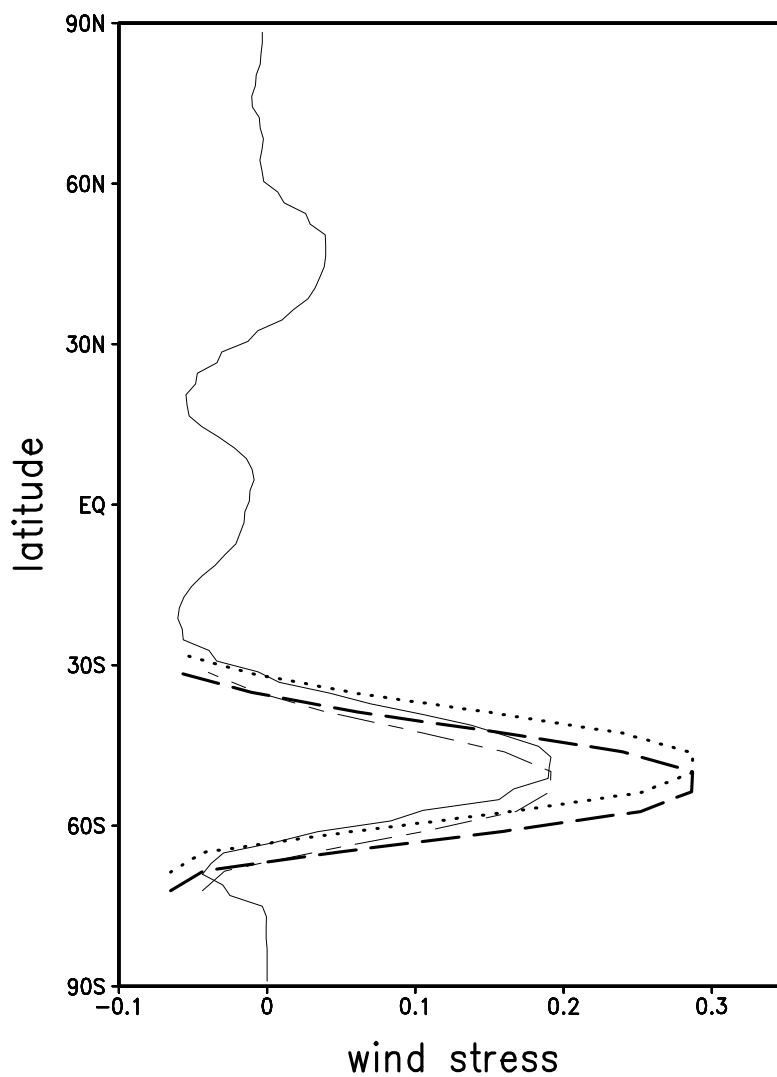


Figure 2.2 Zonal mean wind stress (in Pa) simulated in the CTL experiment (solid) and applied in the wind perturbation the experiment of $W_{x1.5}$ (dotted), W_{PLWD} (long-short dash) and $W_{PLWDx1.5}$ (long dash).

2.2.2 Water isotope simulation setup

To evaluate the hydrological cycle change during the Holocene, we performed simulations for the same scenarios introduced in 2.2.1 with the atmospheric general circulation model ECAHM5-wiso, which implements a water isotope module [Werner *et al.*, 2011]. It is the newest version of the ECHAM family that is equipped with a module for the direct simulation of the stable isotopes ^{18}O and deuterium in all components of the atmospheric water cycle [Hoffmann *et al.*, 1998; Werner *et al.*, 2001]. The spatial resolution of the simulations used in this study is T42 with 19 vertical levels, which is identical with that used in the atmospheric part of the coupled model.

For each timeslice experiment, the boundary conditions are used the same as shown in Table 2.2. Climatologies of monthly SST and sea ice extent as bottom-boundary conditions have been taken from previous coupled simulations with COSMOS, respectively. The surface ocean isotopes boundary condition is prescribed using the global seawater oxygen-18 dataset [LeGrande and Schmidt, 2006]. Each experiment is integrated for 50 years, with the first 10 years neglected and the rest 40 years for statistic analysis, which is sufficient for statistical significance of the modeled anomalies. To distinguish each experiment from each other as well as the coupled timeslice runs, the experiments are named with '-wiso' as a postfix, e.g. CTL-wiso for the control simulation.

Additionally, a sensitivity experiment H9KMS-wiso is conducted with the same boundary condition prescribed in H9KM-wiso, except that, in this experiment, 2 per mill $\delta^{18}\text{O}$ is added to the surface ocean $\delta^{18}\text{O}$ within the area of 5° - 30°N and 30° - 90°W . Results from this experiment are shown in section 5.1.3.2 in order to provide further explanation of the model-data comparison.

2.3 Proxy data

For model-proxy data comparison, two kinds of paleoclimatic archive are used in this study. One is the speleothem archive-stalagmite from north-western Cuba; the other is fossil corals in the Bonaire Island from the southern Caribbean Sea. The sampling locations can be seen in Figure 2.3.

There are two stalagmites Cuba Pequeño (CP) and Cuba Medio (CM) included in this study, which are sampled from the Dos Anas wave system in north-western Cuba (Figure 2.3), and analyzed by colleagues from University of Heidelberg working in the CaribClim project. Both stalagmites are well dated using the Uranium-series dating methods. Stalagmite CP covers the whole Holocene period with a resolution of 4-20a, while stalagmite CM is relatively short and only the data from about 7-10 kyr BP is available. The geological setting and dating have been described in more detail by Fensterer [2010; 2011]. Here, we focus on the $\delta^{18}\text{O}$ values recorded by the Cuban stalagmites, which are mainly a proxy for the precipitation. The observed $\delta^{18}\text{O}$ values can be influenced by many factors, among which the composition of the precipitation and groundwater, and the background conditions that main composition of the stalagmite-calcite is precipitated are of high importance [C Fensterer, 2011]. On shorter timescales, the $\delta^{18}\text{O}$ composition of the precipitation is controlled by the temperature at the mid-high latitudes and amount effect at the low latitudes [Vuille *et al.*, 2003b; Lachniet, 2009]. On longer timescales, it is also influenced by the precipitation seasonality, which is driven by the insolation, and the source of the precipitation, which can be modulated by the $\delta^{18}\text{O}$ values in the ocean. During the glacial-interglacial transition period, the growth and retreat of the ice sheet can result in large difference of the $\delta^{18}\text{O}$ values in the ocean. Consequently, the $\delta^{18}\text{O}$ recorded by the stalagmites can also be affected by large-scale ocean and atmosphere circulation, which redistributes the $\delta^{18}\text{O}$ in different components of the climate system.

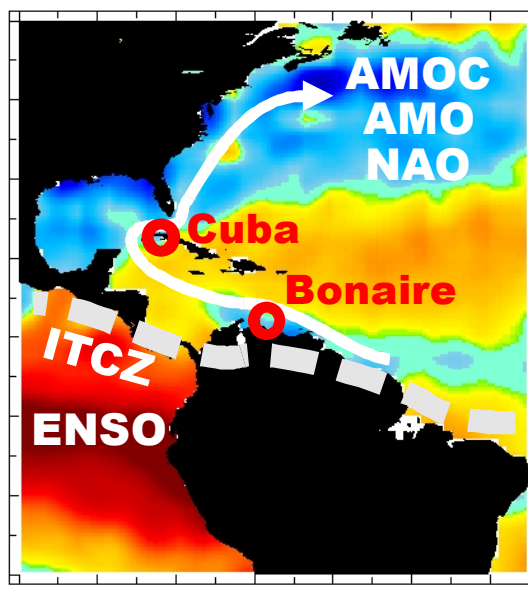


Figure 2.3 Schematic diagram of the study area and the adjacent regions. The sampling locations for the proxies are indicated by the red circles. Possible forcing mechanisms controlling the study area are also shown.

Several fossil corals have been analyzed by the colleagues from University of Bremen working in the CaribClim project. Monthly resolution geochemical signal can be obtained by accurate microsampling along the center of thecal wall from the skeletal of *Diploria strigosa*, which is an important reef-building, shallow water coral of the Caribbean region [Bak, 1977]. Especially, the SST and salinity can be reconstructed by combining $\delta^{18}\text{O}$ and Sr/Ca measurement, which provides ideal information for studying the climate variability in the past [Giry *et al.*, 2010a; Giry *et al.*, 2010b]. In this study, the monthly-resolved coral Sr/Ca records of three modern and one 6.2 kyr BP fossil corals sampled along the coast of Bonaire (Figure 2.3) are included [Giry, 2011; Giry *et al.*, 2011]. Comparison of the seasonality based on the coral records and modeling results will enable us to quantify the seasonality change in the Caribbean during the mid-Holocene.

3. Simulated Atlantic Multidecadal Oscillation during the Holocene

3.1 Introduction

The Atlantic Multidecadal Oscillation (AMO) has been considered an internal mode of the variability in the North Atlantic sea surface temperature (SST) with duration of 50 to 80 years. It was firstly detected in the instrumental data [*Schlesinger and Ramankutty*, 1994; *R.A. Kerr*, 2000] and later on proved to exist in both proxy records [*M E Mann et al.*, 1995; *G Lohmann et al.*, 2004; *Grosfeld et al.*, 2007; *S. Hetzinger et al.*, 2008; *Poore et al.*, 2009; *Knudsen et al.*, 2011] and climate models [*T L Delworth and Mann*, 2000; *Latif et al.*, 2004; *Knight et al.*, 2005].

The typical feature of the AMO is that during its warm (cold) phase, the North Atlantic experiences a general warming (cooling) in the amplitude of about 0.2°C [e.g. *Enfield et al.*, 2001]. Previous studies have demonstrated that this basin-wide pattern has large influence on almost the whole North Hemisphere climate, e.g. Atlantic hurricanes [*Goldenberg et al.*, 2001; *Knight et al.*, 2006; *Zhang and Delworth*, 2006], India/Sahel rainfall [*C Folland et al.*, 1986; *Rowell et al.*, 1995; *Knight et al.*, 2006], North American climate [*Enfield et al.*, 2001; *McCabe et al.*, 2004; *Hu and Feng*, 2008; *Feng et al.*, 2010], Arctic temperature [*Chylek et al.*, 2009], North Pacific climate [*Zhang and Delworth*, 2007], Asian monsoon [*Lu et al.*, 2006] and even part of the South Hemisphere, e.g. north east Brazil rainfall [*C K Folland et al.*, 2001; *Knight et al.*, 2006]. Consequently, prediction of the AMO in the future is highly important for the whole society, especially in the undergoing anthropogenic induced global warming conditions, which may be masked by the AMO signal [*Latif et al.*, 2004].

Some attempts have been made to forecast the AMO in the next decades [*Latif et al.*, 2004; *Knight et al.*, 2005]. However, due to the relatively short length of the

instrumental data, there are still many uncertainties concerning its persistence and forcing mechanism, which makes any prediction more difficult to ascertain. Thus, proxy data and modeling studies provide us a complementary approach. Previous studies based on proxy data can date back to the Holocene, an epoch during which, orbital change, greenhouse gases, solar forcing and volcanic activities control the climate evolution. Knudsen et al. [2011] applied the spectral analyses to several high-resolution records from the region bounding the North Atlantic, and found that a quasi-persistent 55- to 70-year cycle existed through large parts of the last 8,000 years. Based on proxy SST records, Feng et al. [2009] pointed out that the centennial variability of the North Atlantic SST during the Holocene resembled the common AMO feature. More recently, Giry et al. [2011] showed that a substantial AMO-like signature can be found in their mid-Holocene coral records, which have been proved to enable them to reconstruct the temperature variation associated with the AMO [Heslop and Paul, 2010]. More efforts have been made concerning the reconstruction of the AMO for the last several centuries [e.g. *M E Mann et al.*, 1995; *Gray et al.*, 2004; *S. Hetzinger et al.*, 2008].

Large amount of modeling studies have been carried out in the direction of understanding the forcing mechanisms of the AMO and its climate influence [e.g. *T L Delworth and Mann*, 2000; *Latif et al.*, 2004; *Knight et al.*, 2005; *Knight et al.*, 2006]. However, rare modeling studies [e.g. *Oglesby et al.*, 2011] have concentrated on the past AMO reconstruction. In this study, we investigate the AMO pattern and its robust feature during the Holocene by performing several long-term numerical experiments. Moreover, comparisons between experiments allow us to explore the AMO variation during the Holocene, resulting from different external forcing. We also show the climate influence of the AMO under different climate conditions, which might provide useful information for the future AMO prediction.

3.2 Mean climate during the Holocene

The seasonal and annual mean climatology is calculated by averaging the corresponding parameters over the whole valid integration periods.

The simulated air surface temperatures are shown in Figure 3.1. Compared to the pre-industrial condition, the most intriguing large-scale feature during the mid-Holocene is that the North Hemisphere high latitudes experience a warming up to 2 °C in boreal summer, especially over the continents (Figure 3.1a). Such a feature can be attributed mainly to increased insolation in boreal summer, which is induced by a larger tilt of the orbital plane [Berger, 1978]. This is consistent with the previous modeling studies [e.g. Braconnot *et al.*, 2007]. This effect is amplified during the early Holocene, resulting in a stronger summer warming in the North Hemisphere (Figure 3.1b). Meanwhile, the winter cooling during the early Holocene is also much stronger than that during the mid-Holocene (Figure 3.1a,b). Together with the cooling effect generated by less greenhouse gases, more cooling is expected in the annual mean values (Figure 3.1b).

Changes in the topography (Figure 2.1) during the early Holocene have a considerably global influence on the climate. Compared with H9KO, a general warming due to the sea level decrease can be seen clearly in H9KT (Figure 3.1b,c). Notably, there is a strong cooling (more than 10 °C) directly over the LIS due to the combined effect of higher surface elevation and larger surface albedo (Figure 3.1c). This cooling overcompensates the positive insolation anomaly and can extend over the North Atlantic. Freshwater associated with the background melting of the LIS contributes additional cooling over the North Atlantic, which leads to up to 5 °C over the whole North Atlantic as well as the Scandinavia (Figure 3.1d).

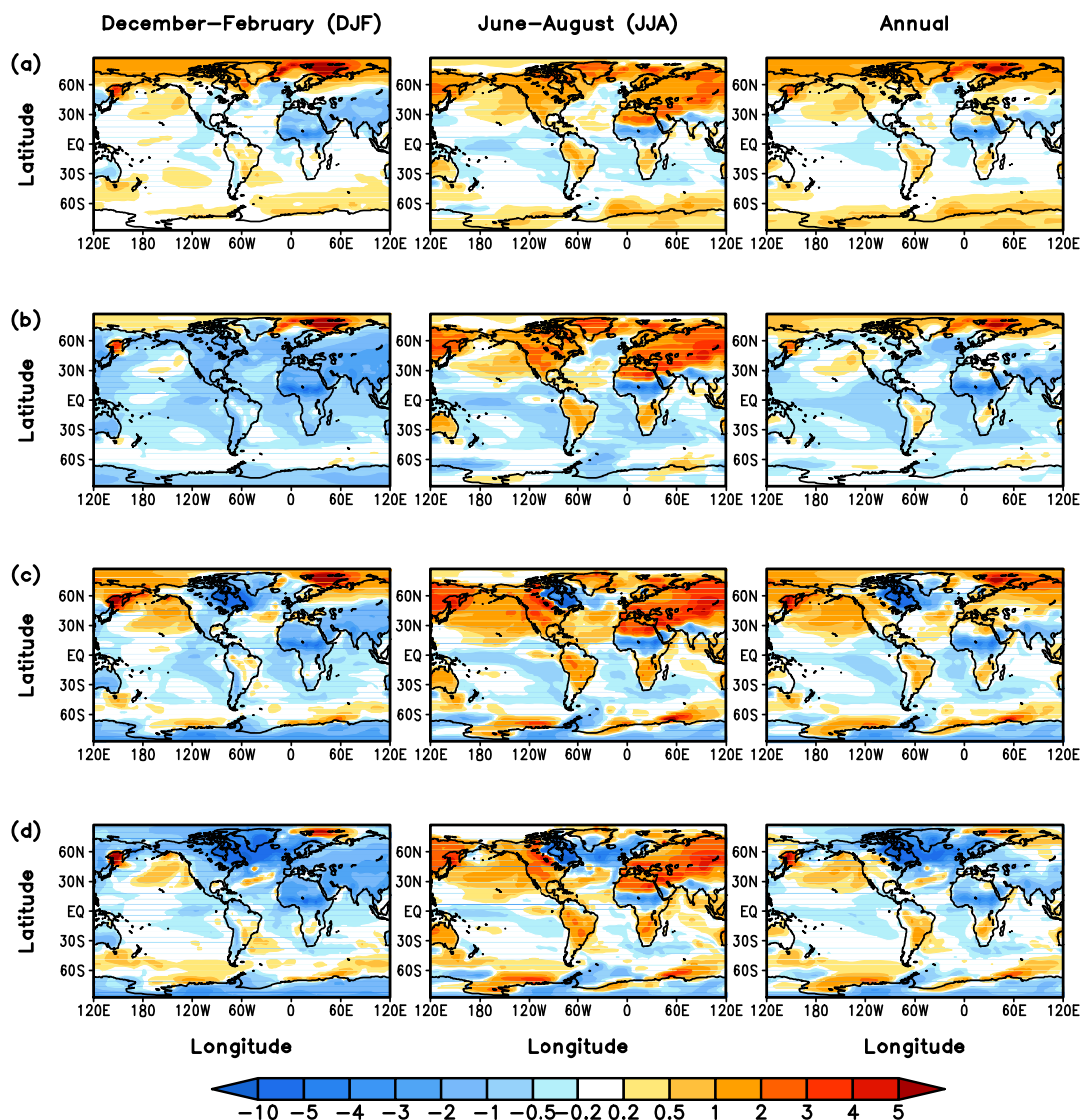


Figure 3.1 Simulated surface temperature anomalies (in °C) relative to CTL¹ in (a) H6K², (b) H9KO³, (c) H9KT⁴ and (d) H9KM⁵, respectively. For each experiment, the left figure is for boreal winter (December–February); the middle is for boreal summer (June–August); the right is for annual mean.

¹ CTL: present-day control experiment (detail in section 2.2.1.1)

² H6K: mid-Holocene (6 kyr BP) experiment

³ H9KO: early Holocene (9 kyr BP) experiment with orbital parameters and greenhouse gas change

⁴ H9KT: identical with H9KO except including the prescribed LIS

⁵ H9KM: identical with H9KT except including the freshwater flux from melting of the LIS

Corresponding to the insolation change during the Holocene, the precipitation pattern is characterized by wetter conditions over the Africa and India in both 6 kyr and 9 kyr BP (Figure 3.2). This increase in precipitation results from the enhanced monsoon system due to the increased summer insolation and has been found to be a key feature during the Holocene climate evolution [Kutzbach and Liu, 1997; Zhao *et al.*, 2005]. Over the tropical Atlantic, the enhanced land-sea contrast favors a northward shift of the intertropical convergence zone (ITCZ). The ITCZ over the Pacific is also strengthened. However, a drying condition is produced along the equator of the Pacific, caused by the cooling of the ocean surface (Figure 3.2).

The simulated Atlantic meridional overturning circulation stream function for the present condition has the maximum of 16.1 Sv at 1000m depth of 30°N (Figure 3.3a), consistent with the estimates of global circulation from the hydrographic data [15 ± 2 Sv; Ganachaud and Wunsch, 2000]. This value decreases by 2.3 Sv in the mid-Holocene and 3.3 Sv in the early Holocene run H9KO, respectively (Figure 3.3b,c). Previous study [Fischer and Jungclauss, 2009] using a similar model setup with an old version of the vegetation model JSBACH showed that, this reduction of the North Atlantic deep water (NADW) formation also happens in their mid-Holocene and Eemian experiments, when the North Hemisphere high latitudes get more insolation compared to the pre-industrial condition. It can be explained by a combined effect of insolation induced warming over the high latitudes and sea ice reduction in the Arctic. In experiment H9KT, the AMOC shows a very different feature with that in H9KO, with about 2 Sv increase at 30°N relative to CTL and more than 5 Sv increase relative to H9KO (Figure 3.3d). The cooling effect of the LIS over the North Atlantic increases the surface water density and thus produces enhanced deep water formation, which can overwhelm the warming effect by the orbital change. This cooling is most significant over 40°-60°N. As a consequence, the deep water formation increases dramatically in the same latitude band, leading to a shift of the AMOC maximum from 30°N to 40°N (Figure 3.3d). Contrary to the cooling effect by the ice sheet, the melting of the LIS injects large amount freshwater into the North Atlantic and triggers a strong reduction of the NADW formation (Figure 3.3e). The

magnitude of this reduction is comparable with a Holocene transient run with identical forcing [Renssen *et al.*, 2010] except that in their study, the prescribed LIS melting flux increased to 0.1 Sv to prevent any deep water formation in the Labrador Sea.

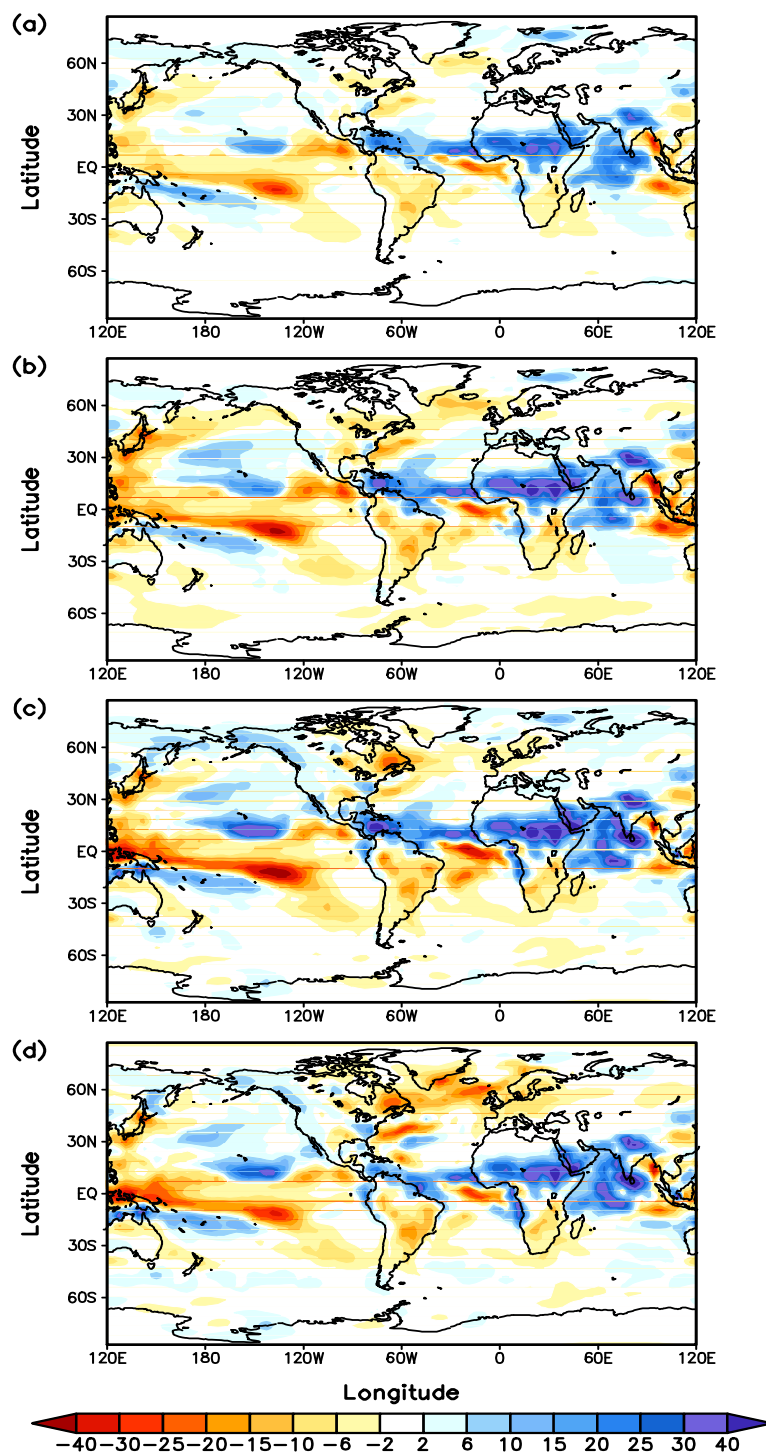


Figure 3.2 Annual precipitation anomalies (in mm/month) relative to CTL in (a) H6K, (b) H9KO, (c) H9KT and (d) H9KM, respectively.

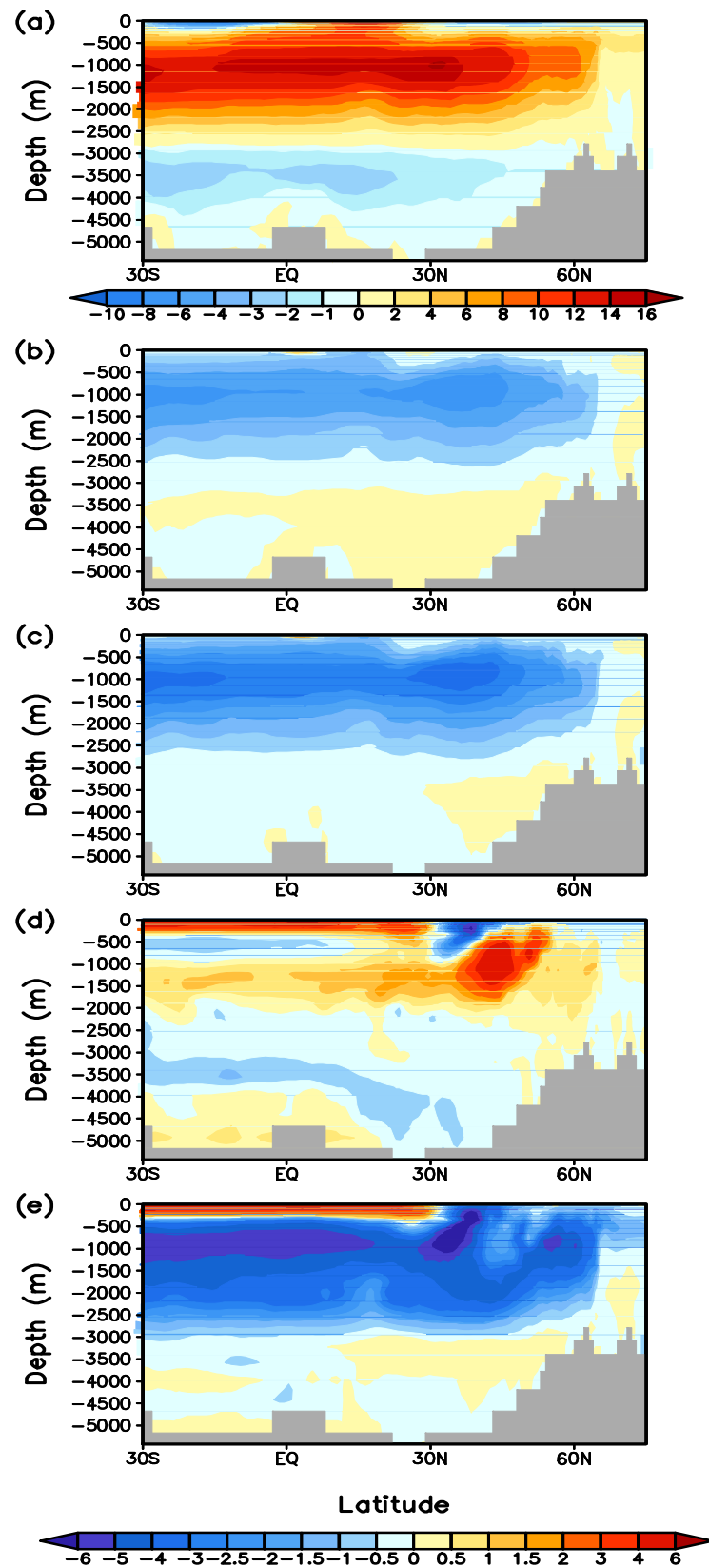


Figure 3.3 Annual AMOC streamfunction anomalies (in mm/month) relative to CTL in (a) H6K, (b) H9KO, (c) H9KT and (d) H9KM, respectively.

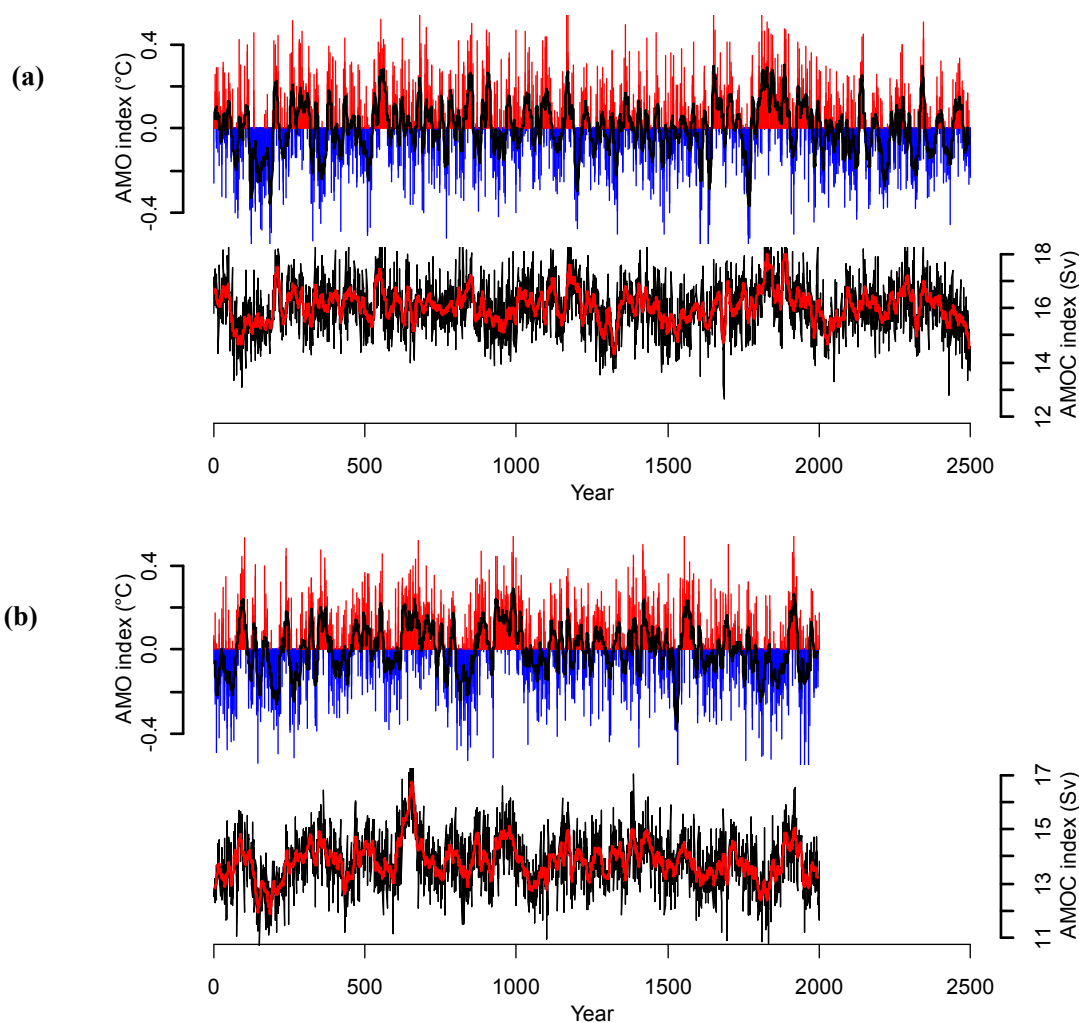
3.3 Periodicity of the AMO indices

The AMO indices (Figure 3.4) are constructed based on the simulated SSTs in a similar way following previous studies [e.g. *Knight et al.*, 2005; *Sutton and Hodson*, 2005; *Dima and Lohmann*, 2007]. Here, SSTs are identical with the air surface temperature over the ocean as shown in Figure 3.2. Each index is calculated by averaging the annual mean SST over the region 0° - 60° N, 75° - 7.5° W. Then a linear trend is removed and the anomalies are derived by subtracting the time series from its mean value. A roughly 0.4° C peak-to-peak oscillation can be obtained from the long-term mean indices, which has good agreement in the observed AMO variation [e.g. *Enfield et al.*, 2001].

To identify the simulated periodicity of the AMO indices that have a typical 50- to 80-year cycle in the observation, we apply the multitaper method (MTM) spectral analysis [*J Park*, 1992a] to the corresponding indices. To be expected, pronounced 50- to 80-year cycle exists in all the AMO indices (Figure 3.5a-e). Meanwhile, variations in decadal and centennial timescale also can be found in each spectrum. The latter has been suggested to associate with the centennial variation of the AMOC induced by Southern Hemisphere westerly winds [*Wei et al.*, 2011]. Our results (Figure 3.5a-e) reveal that the AMO is a quasi-multidecadal oscillation independent with the background climate conditions. For each experiment, the prescribed forcing is kept constant during the integration. Thus, the simulated 50- to 80-year cycle can provide further evidence that, the periodicity of the AMO inferred from the instrumental data also exists in the simulation as indicated by previous studies [*T L Delworth and Mann*, 2000; *Knight et al.*, 2005], and is induced by the internal variability of the climate system. Nevertheless, the background climate conditions can modulate both the periodicity and magnitude of the AMO (Figure 3.4 and Figure 3.5a-e).

To better investigate the influence of background climate conditions on the periodicity of the AMO, we perform the wavelet spectral analyses (Figure 3.5f-j) using the same time series shown in Figure 3.4, which gives the temporal variation of the AMO periodicity. Similar with the MTM spectral analysis, all wavelet spectrums display a

quasi-persistent 50- to 80-year cycle. But interestingly, this cycle is more pronounced in some experiments, e.g. CTL and H9TO (Figure 3.5f,h). Combining with the mean climatology discussed in 3.2, however, there seems no direct explanation for this difference. Results from both instrumental and modeling studies [*Knight et al.*, 2005; *Dima and Lohmann*, 2007] have suggested that the engine for the AMO involves variation in strength of the AMOC, which leads us to investigate the relation between the AMO and the AMOC in our simulation. The correlation coefficients of the 11-year running mean AMO indices with the corresponding AMOC indices (Figure 3.4) are 0.459, 0.542, 0.300, 0.369 and 0.553 for CTL, H6K, H9KO, H9KT and H9KTM, respectively, i.e. the decadal variation of the AMO is highly associated with the AMOC change. However, the values (Figure 3.4) are only 0.179, 0.228, 0.141, 0.083 and 0.207 for the annual indices, respectively, which indicates there is no significant relation between the AMO and AMOC on short timescale.



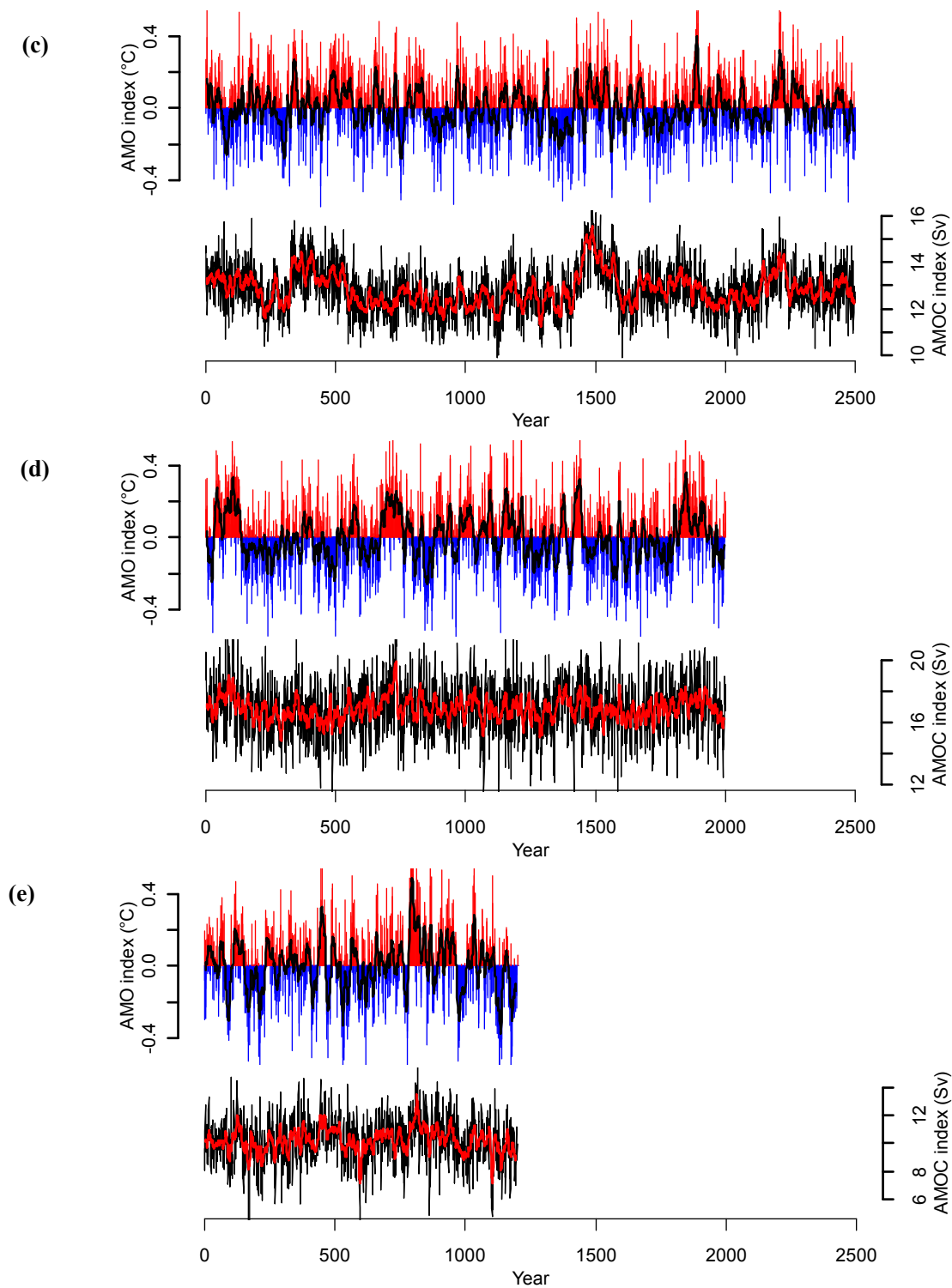


Figure 3.4 The AMO indices (in $^{\circ}\text{C}$; red and blue) and the AMOC indices (in Sv; black) for (a) CTL, (b) H6K, (c) H9KO, (d) H9KT and (e) H9TM, respectively. The AMO indices are constructed based on simulated sea surface temperature averaged over the region 0°N to 60°N , 75°W to 7.5°W . The solid lines represent the 11-year running mean values. The AMOC indices are derived from the maximum meridional stream function at 1000m depth of 30°N in the Atlantic Ocean. The 11-year running mean values are plotted using the red solid lines.

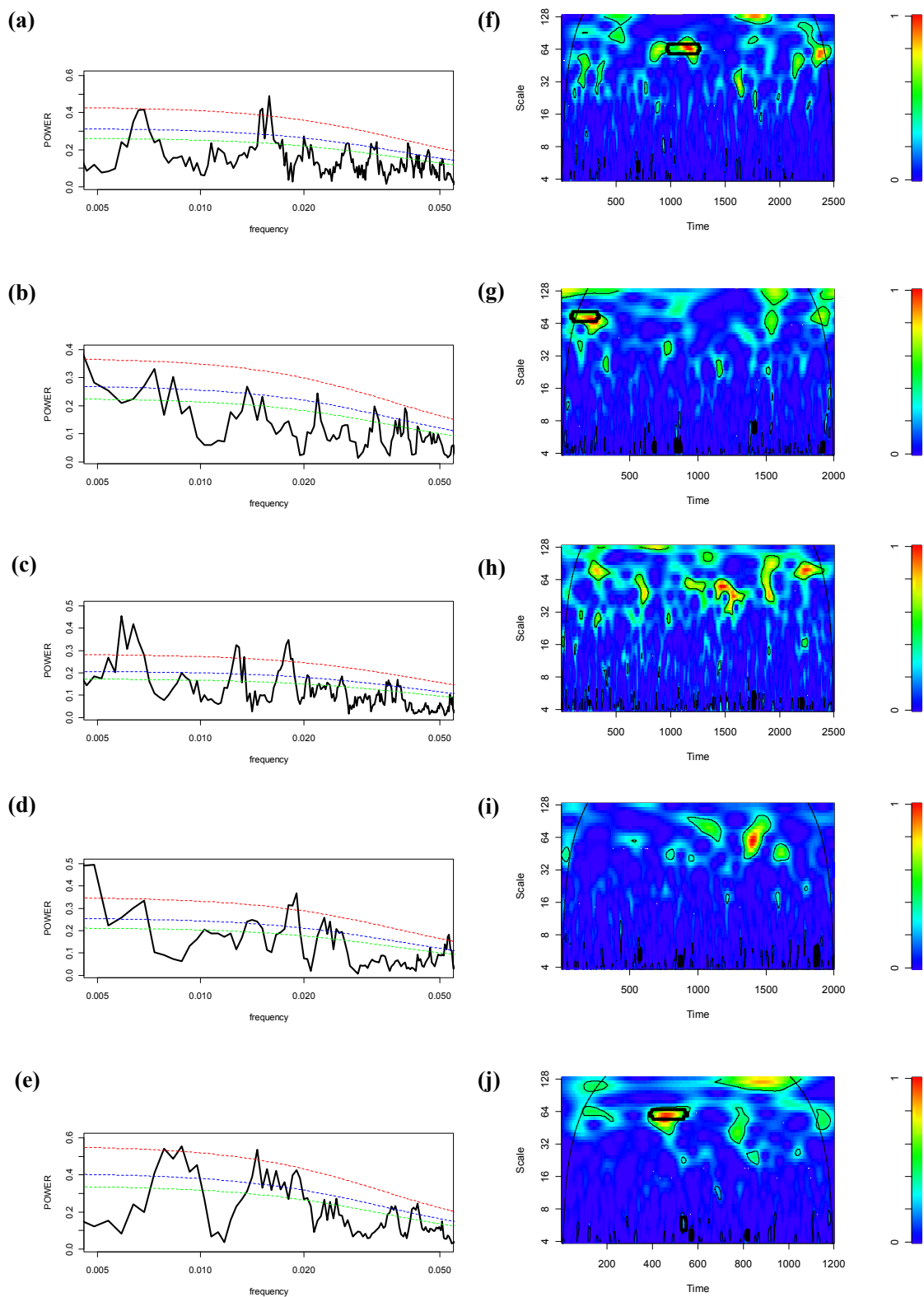


Figure 3.5 Multitaper method (MTM) spectral analyses of the AMO indices for (a) CTL, (b) H6K, (c) H9KO, (d) H9KT and (e) H9KM, respectively. The significance levels of 90%, 95% and 99% are plotted by green, blue and red dotted lines, respectively. (f)-(j) are the corresponding wavelet spectrums. The thin and thick solid circles indicate the 90% and 95% significant levels, respectively.

3.4 Spatial patterns of the temperature and AMOC associated with the AMO

The spatial patterns of the temperature associated with the AMO are illustrated by composite analyses of the air surface temperature with the corresponding AMO indices (Figure 3.6). During the warm phase of the AMO, there is a quasi-monopolar temperature structure [Dima and Lohmann, 2007] over the Atlantic Ocean, with dramatic warming in the north and slight cooling in the south. This quasi-monopolar temperature pattern is a robust feature of the AMO, as indicated by both observation [Enfield *et al.*, 2001; G Lohmann *et al.*, 2004; Dima and Lohmann, 2007] and modeling studies [T L Delworth and Mann, 2000; Latif *et al.*, 2004; Knight *et al.*, 2005]. Meanwhile, the North Pacific is also characterized by a general warming, which is affected through atmospheric teleconnections [Dima and Lohmann, 2007]. It is worth noting that this feature of the AMO shows no remarkable difference during the Holocene.

Associated with the warm phase of the AMO, there is coherent strengthening of the AMOC stream function north of 30°N (Figure 3.7). This in-phase relationship between the AMO and the AMOC reflects the high correlation of the decadal running mean AMO and AMOC indices (Figure 3.4), further confirming that the AMO is potentially driven by the multidecadal variation of the AMOC. The slightly weakening of the overturning around 60°N can be linked to the shrink of the sea ice coverage resulting from the warming in the high latitudes (Figure 3.8). The AMOC patterns demonstrate a common feature in all the experiments except that it has pronounced amplification in H9TM (Figure 3.7e), in which a relatively vigorous fluctuation of the AMOC exists due to the melting water flux of the LIS (Figure 3.4e). This might indicate that the melting induced cooling acquires a much more strengthening of the AMOC to overwhelm its cooling effect, and thus reach a warm phase of the AMO. Meanwhile, this vigorous AMOC fluctuation also leads to a comparably stronger AMO warm phase (Figure 3.6e).

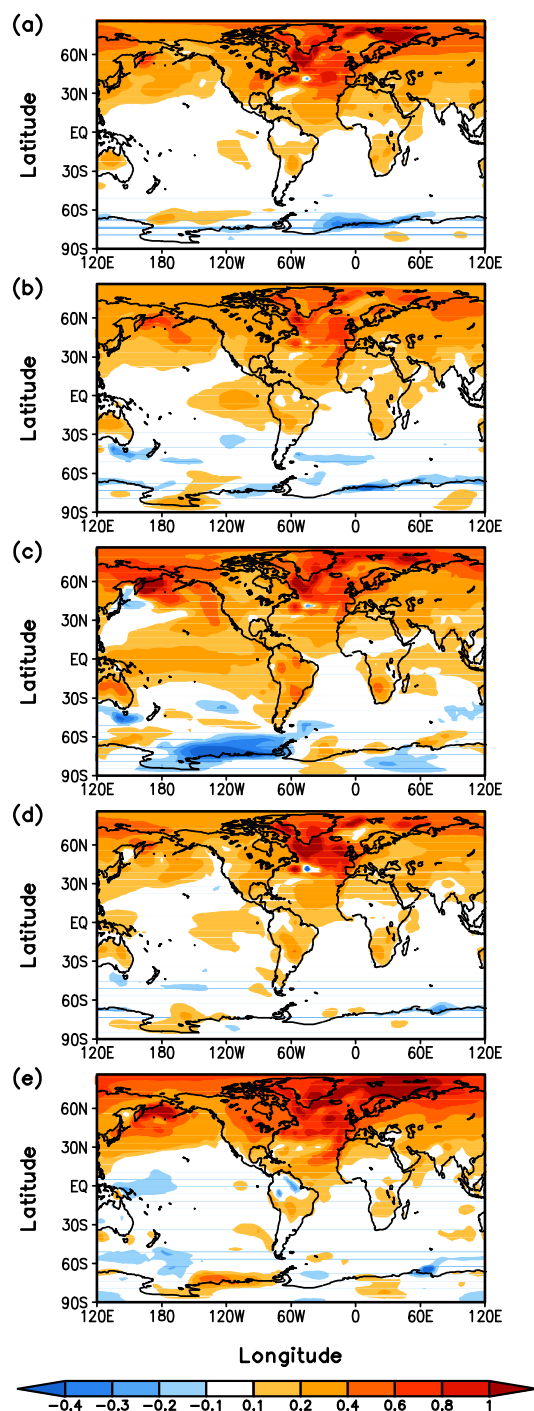


Figure 3.6 Composite maps of surface temperature (in $^{\circ}\text{C}$) with the AMO index for (a) CTL, (b) H6K, (c) H9KO, (d) H9KT and (e) H9KM, respectively. The band-pass filter has been applied to both the indices and fields to assure only variations in multidecadal timescale are represented. A linear trend is also removed before the composite analyses. The composite maps shown here are calculated by subtracting the fields that have higher than one standard deviation of the mean from those with lower than one standard deviation with respect to the indices. Here anomalies with significance higher than 95% are plotted.

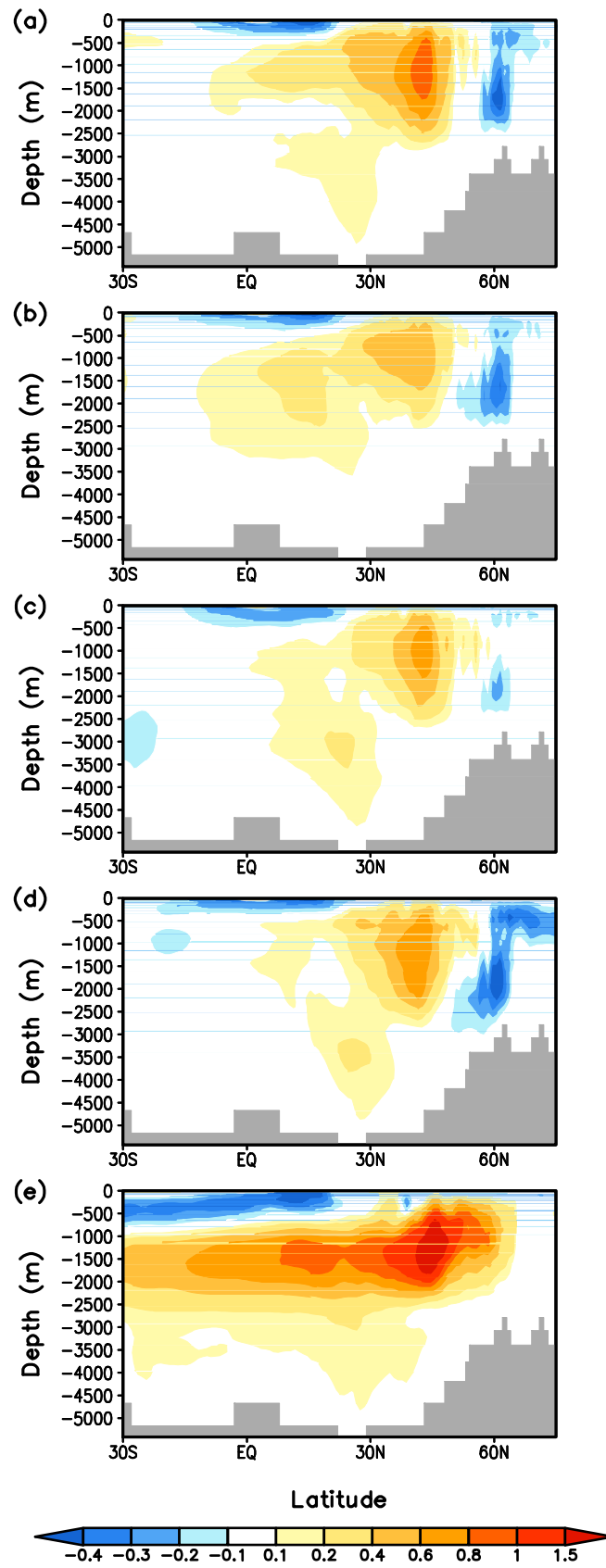


Figure 3.7 As Figure 3.6, but for the AMOC stream function (in Sv).

3.5 Climate influence of the AMO

During a warm phase of the AMO, not only the North Atlantic experiences a large scale warming, also the warming can spread over the whole mid-high latitudes in the North Hemisphere (Figure 3.6), consistent with previous observation and modeling studies [Knight *et al.*, 2005]. This warming shows relatively stronger signal in H9KM (Figure 3.6e). It might suggest that the AMO is more sensitive to the cold period, when the cooling and freshening caused by the ice sheet and its melting can lead to a less stable climate condition. Over the low latitudes and South Hemisphere mid-high latitude, influence of the AMO is not pronounced except that slightly warming over the land areas, i.e. part of the South American, North Australia and part of the Africa (Figure 3.6).

The precipitation field shows the maximum anomalies in phase with the AMO warm period is located over the North Atlantic low latitudes, with pronounced wetter condition (Figure 3.9). Moderate anomalies include more rainfall over the Sahel, drought condition in the North American east coastal areas, wetter condition in Europe and less precipitation in Brazil (Figure 3.9), all of which are consistent with previous findings [Sutton and Hodson, 2005; Knight *et al.*, 2006]. But interestingly, although the general pattern persists in all the simulations regardless of the mean climate background, it demonstrates distinct regional characters and magnitude.

The associated sea ice change (Figure 3.8) coincides with change in the surface temperature (Figure 3.6). During a warm phase of AMO, the warming in the high latitudes of the North Hemisphere leads to melting of the sea ice. The decreasing of the sea ice fraction has the maximum in Barents Sea, where the strongest warming occurs due to the heat transport by the ocean current. The feature in the Southern Ocean is not clear, with both increasing and decreasing of the sea ice coverage.

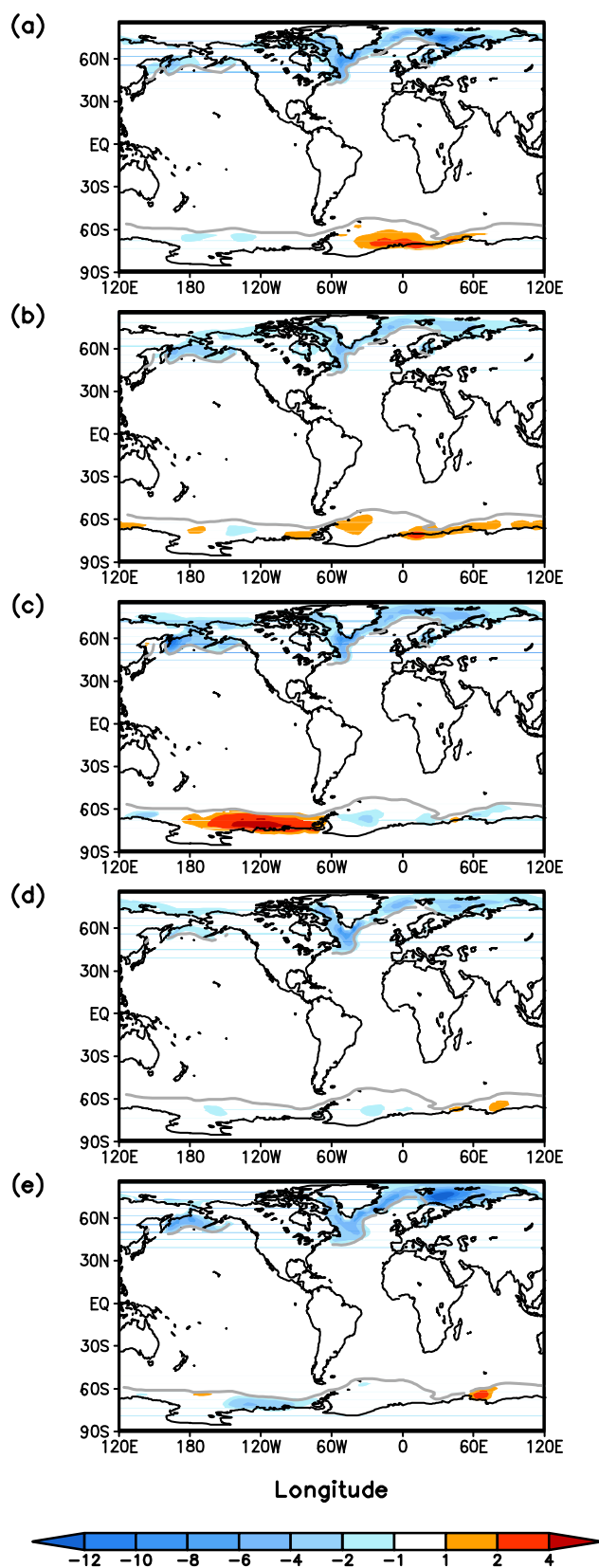


Figure 3.8 As Figure 3.6, but sea ice fraction (in %). The grey solid lines indicate the boundary of the sea ice coverage in each experiment.

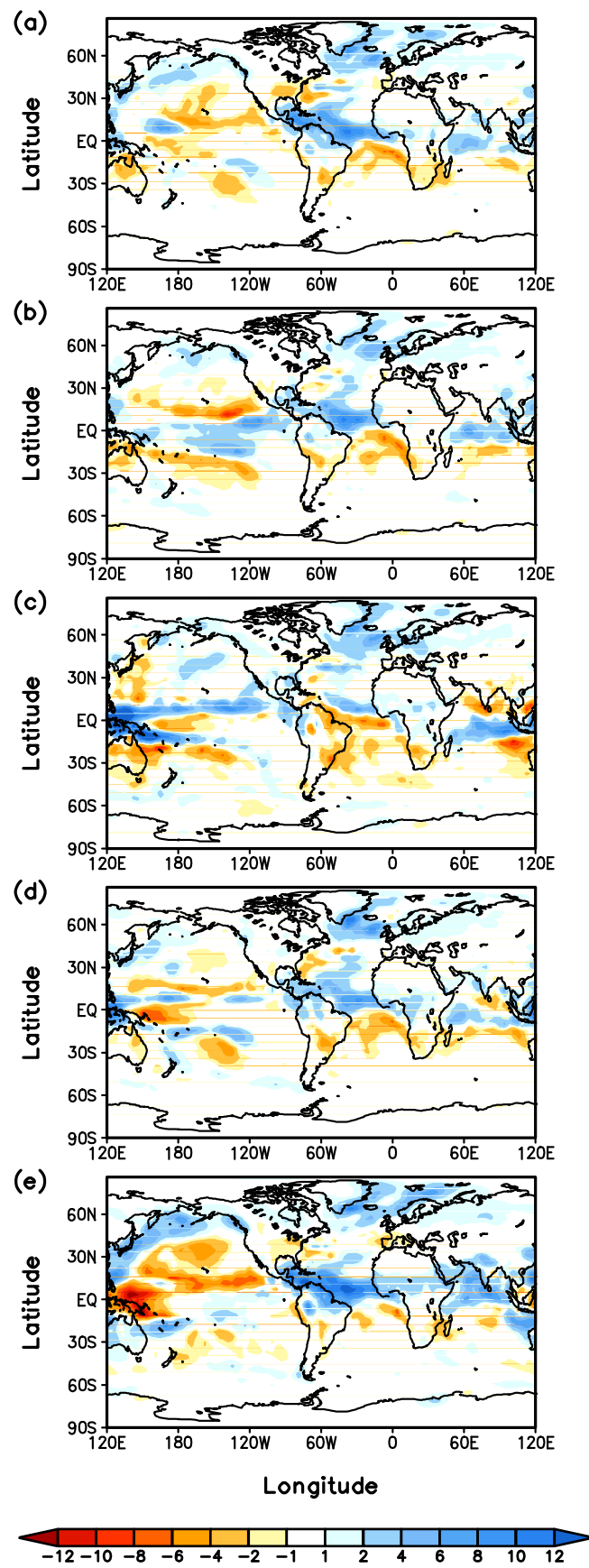


Figure 3.9 As Figure 3.6, but for the precipitation (in mm/mon).

3.6 Discussion and summary

Concerning the forcing mechanism of the AMO, the most common believed physical process involves the variation of the AMOC. Although a fully understanding of such a process is beyond the scope of this study, our results show the strong correlation between the AMO index and AMOC index on multidecadal timescales and, during a warm phase of the AMO, the AMOC is intensified significantly.

The simulated AMO indices exhibit a quasi-multidecadal periodicity, consistent with the typical 50-80 year cycle of the AMO indicated by the observation data [Schlesinger and Ramankutty, 1994; R.A. Kerr, 2000]. A warm phase of the AMO accompanies a hemispheric scale warming in the NH, with the maximum warming over the North Atlantic and part of the Arctic. Such a warming favors more evaporation and thus more precipitation over most part of the North Atlantic, especially enhancing the Atlantic ITCZ.

The climate influence of the AMO during the Holocene demonstrates that there is no remarkable change in its spatial pattern under different climate background conditions, which further reveals that the AMO is an internal variability of the climate system. However, we imply that this influence can be distinguished regarding the regional scale feature and its magnitude. It has been supported by a pervious study, which suggests that the regional response to the AMO can be modulated by orbitally induced shifts in large-scale ocean-atmosphere circulation [Knudsen *et al.*, 2011]. Moreover, we argue that the climate influence of the AMO might be amplified by a vigorous background climate condition, in particular during a cold period.

4. Distinct modes of internal variability in the Global Meridional Overturning Circulation associated with the Southern Hemisphere westerly winds

4.1 Introduction

The winds are one of the major forcing that modulates the global meridional overturning circulation (GMOC) [*J Toggweiler and Russell, 2008*], by transferring the atmospheric kinetic energy directly or indirectly to the ocean via Ekman transport and geostrophic flow [*Wunsch and Ferrari, 2004*]. It is estimated that about 70% of this transfer takes place over the Southern Ocean (SO) [*Wunsch, 1998*]. The most important pattern of climate variability in the Southern Hemisphere (SH) mid- to high latitudes is related to the Southern Annular Mode (SAM). Positive phase of the SAM can enhance the Southern Hemisphere westerly winds (SWW), resulting in increased equatorward Ekman transport [e.g. *Lovenduski and Gruber, 2005; Sen Gupta and England, 2006*].

Toggweiler and Samuels [1993; 1995] examine how the SWW can influence the GMOC. By performing a number of sensitivity experiments, they highlight the “Drake Passage effect”: the magnitude of the inflow and outflow from the Atlantic to the SO is linearly correlated with the strength of the SWW at latitude of the Drake Passage. This effect is then further elaborated, showing that after applying stronger SWW, stronger upwelling at the latitude of Drake Passage increases the density gradient across the Antarctic Circumpolar Current (ACC) and thus produces a stronger ACC [*McDermott, 1996*]. On the contrary, a shutdown of the SWW is reported to induce the disappearance of the SO overturning [*Ma et al., 2010*].

Using idealized single-basin and twin-basin models, as well as ocean general circulation models, several studies [e.g., *Gnanadesikan and Hallberg, 2000; Hirabara*

et al., 2007] indicate that stronger SWW can induce more deep-outflow through the South Atlantic, which needs to be compensated by more deep water formation in the North Atlantic, and thus increases the North Atlantic deep water (NADW) formation. The GMOC, on one hand, varies with the magnitude of SWW; on the other hand, it also depends on the latitude of the wind bands. A poleward shift of zero wind stress curl can result in a stronger Atlantic meridional overturning circulation (AMOC) and vice versa [Sijp and England, 2008; 2009]. Delworth and Zeng [2008] use a coupled general circulation model (GCM) to simulate the impact of altered wind stress over the SH on the AMOC and conclude that enhanced (reduced) and poleward (equatorward) shift of the SWW result in a strengthening (weakening) of the AMOC. However, using the fine-resolution eddy-permitting version of the same model, Farneti and Delworth [2010] demonstrate that poleward eddy fluxes associated with a strengthening of the SWW can largely compensate the enhanced equatorward Ekman transport and thus significantly reduce the AMOC anomalies.

The SWW affects not only the AMOC but also the Indo-Pacific overturning circulation. A SH wind stress perturbation experiment [Klinger and Cruz, 2009] estimates the Indo-Pacific volume transport anomaly in the SH as twice the amount in the South Atlantic. By contrast, the volume transport anomaly has a similar magnitude over both basins in the North Hemisphere (NH). However, changes of the SWW have the opposite effect on different ocean basins in the NH. A stronger AMOC due to enhanced and poleward shift of the SWW normally accompanies a damped sinking in the North Pacific [Sijp and England, 2009]. Thus, a seesaw-like pattern between the Atlantic and the Pacific overturning can be expected, which might be amplified by the Atlantic-Pacific seesaw [Saenko *et al.*, 2004], which involves a positive feedback between ocean circulation and salinity at low and high latitudes.

The GMOC response to the SWW varies temporally as well, in all ocean basins. Klinger and Cruz [2009] pointed out that a SH wind stress anomaly can generate the volume transport anomaly in the whole SH within one decade. While in the NH, this anomaly in the AMOC persists in their 80-year simulation. They also argue that the Ekman transport initiated by the wind stress anomaly should be much larger in the

Indo-Pacific basin than that in the Atlantic basin, due to the fact that the former one is much broader. In another perturbation experiment mentioned above, Delworth and Zeng [2008] found that it takes one-to-two centuries for the AMOC to fully adjust to the wind stress anomaly. Both results are consistent with previous studies, which show that the GMOC anomalies on interannual to decadal time scales is confined to the basin in which they are generated, but might have a global impact through the atmospheric teleconnection [*Johnson and Marshall, 2004*].

Modeling studies reveal that the AMOC have the variability on decadal and multidecadal to centennial timescale [e.g., *T Delworth et al., 1993; W Park and Latif, 2008*], which is not induced by any external forcing, but through internal variability in the climate system. The variability at these time scales generates specific sea surface temperature (SST) patterns. The most discussed one, identified in observational data, is the so called Atlantic Multidecadal Oscillation [AMO; *Richard A. Kerr, 2000*], the basin-wide North Atlantic SST anomaly with a typical period of 65-80 years [*Enfield et al., 2001*]. *Dima and Lohmann [2007]* examined a hemispheric mechanism of this mode based on long-term instrumental data. They found that its periodicity is related to the AMOC adjustment to freshwater fluxes, the Atlantic SST response to it, the ocean-atmosphere feedback in the North Pacific and the sea ice response to wind stress. Evidence of this mode also exists in proxy data [e.g., *M Mann et al., 1995; G Lohmann et al., 2004*]. More recently, two distinct SST patterns have been found in the instrumental data – a global mode on centennial timescale and an Atlantic mode associated to multidecadal variability, which are potentially linked to variability of GMOC and AMOC, respectively [*Dima and Lohmann, 2010*].

A previous study [*McDermott, 1996*] suggests that longer time scales rather than interannual variability in SWW can influence the sinking in the NH and modulate the GMOC. In this study, we highlight the decadal and longer time scale internal variability of the GMOC driven by SWW anomalies based on model simulations. To our knowledge, it is the first attempt to focus on the internal variability of this phenomenon compared to a large number of SWW perturbation experiments performed before. Our aims are (1) to identify the dominant modes of the GMOC

internal variability at decadal and longer time scales, (2) to find and distinguish the forcing mechanisms that control the different modes, and (3) to analyze the influence of the corresponding modes on the climate.

The layout of this chapter is as follows: a brief introduction of the data and methods used in this study is given in section 4.2; in section 4.3 are presented the results of numerical experiments and statistical analyses, and propose the physical mechanisms to support our findings. Finally, discussion and conclusions complete the paper in section 4.4 and 4.5.

4.2 Data and Methods

In this chapter, data from CTL⁶ and H6K⁷ are used in the following analyses. After 1000-year spin-up of each experiment, there is no detectable trend in the surface fields. Slight trend exists in the deep ocean, which can be attributed to the slow adjustments in temperature and salinity. Therefore, a linear trend is removed from the corresponding fields and time series before applying the statistical analyses. To concentrate mainly on the decadal and longer timescale variability, we apply a 15-year running mean to the annual mean GMOC streamfunction anomaly and all the other fields used in this study. Here, the anomaly is calculated by subtracting 2000-year average from the annual mean of this field. Then the empirical orthogonal function analysis [EOF; *E Lorenz*, 1956] is used to identify the dominant modes of the GMOC. To distinguish the modes and try to elucidate the mechanisms that control each mode, we use the composite analysis of the principal components (PCs) with different fields. Here, all the composite maps are illustrated by subtracting the composite fields that have higher than one standard deviation of the mean from those with lower than minus one standard deviation with respect to time series of the corresponding PCs.

⁶ CTL: present-day control experiment (detail in section 2.2.1.1)

⁷ H6K: mid-Holocene (6 kyr BP) experiment

Additionally, we perform three SWW perturbation experiments to support our hypotheses by modifying the magnitude and position of the SWW stress in the ocean model. Details of these experiments are introduced in section 2.2.1.2.

4.3 Results

4.3.1 Mean state of the GMOC and AMOC

Figure 4.1 shows the 2000-year mean state of simulated GMOC and AMOC in both CTL and H6K experiments. In CTL (Figure 4.1a), the model produces the Deacon cell [Deacon, 1937] in a range 30 ~ 40 Sv ($1 \text{ Sv} = 10^6 \text{ m}^3/\text{s}$) near 50°S, due to the Ekman divergence. The simulated Deacon cell is comparably larger than that in previous studies [e.g. Döös and Webb, 1994; Speer *et al.*, 2000], which can be related to stronger SWW in the simulation. In CTL, the annual mean value of zonal-averaged surface wind u component has a maximum of 9.2 m/s near 50°S (not shown), whereas it is about 7.3 m/s in the observation averaged over the period 1948-2010 [Kalnay *et al.*, 1996]. Such stronger SWW might be partly attributed to the different boundary conditions in CTL compared with the present-day condition, e.g. a lower greenhouse gas concentration on pre-industrial level, which can result in a relative cooling climate background and hence strong SWW [J Toggweiler and Russell, 2008]. Production of the Antarctic Bottom Water (AABW) is 8.4 Sv, which is consistent with the observation data [8.1 Sv; Orsi *et al.*, 1999]. The AMOC (Figure 4.1b) has a reasonable structure as well, with the deep water formation between 30°N and 60°N penetrating to a depth of 2500m. The maximum value of the AMOC index (defined as the AMOC streamfunction maximum at 30°N in the North Atlantic), which has a 2000-year mean annual value of 16.0 Sv with standard deviation of 1 Sv, is in good agreement with the estimates of global circulation from the hydrographic data [15 ± 2 Sv; Ganachaud and Wunsch, 2000]. Its spectrum analysis exhibits variability with multidecadal as well as centennial timescales (Figure 4.2). Such multidecadal

variability has been interpreted as an atmosphere-ocean coupled mode in a present-day simulation [Zhu and Jungclauss, 2008], using the same coupled model setup, but without interaction of the land surface model.

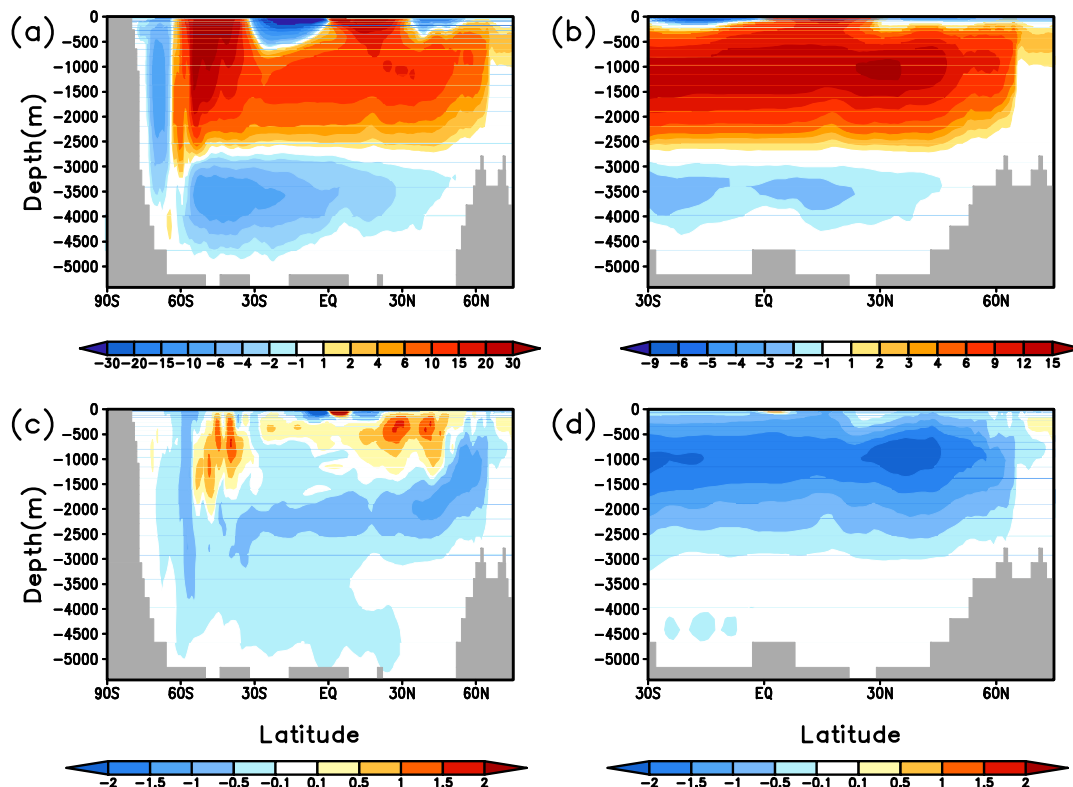


Figure 4.1 Simulated annual mean GMOC (left) and AMOC (right) streamfunction (in $\text{Sv} = 10^6 \text{m}^3/\text{s}$) averaged over 2000 years in (a,b) CTL. (c,d) Their anomalies in H6K relative to CTL.

In the H6K experiment, the structures of the GMOC and AMOC are identical with those in CTL. Notably, compared to CTL, the intriguing feature of the AMOC in the mid-Holocene simulation (Figure 4.1d) is that its maximum value at 30°N of the North Atlantic is reduced by 2.5 Sv. This reduction is induced by changes in the orbital parameters and high-latitude warming [Fischer and Jungclauss, 2009]. Meanwhile, the Pacific overturning is also weakened (Figure 4.1c). The SWW in H6K shows no significant change compared to CTL. The annual mean value of zonal-averaged surface wind u component reaches a maximum of 9.2 m/s near 50°S, in a similar magnitude with that in CTL (not shown). Therefore, the overturning

circulation in the SO has not much difference with that in CTL (Figure 4.1c).

4.3.2 Global modes of the overturning circulation

The two most important modes and the corresponding PCs from the EOF analysis that is based on the GMOC streamfunction are shown in Figure 4.2. They explain 29.38% and 12.22% of total variance, respectively and are well separated. For both modes, oscillations with vigorous multi-decadal to centennial timescale can be seen in multitaper method (MTM) spectral analysis [*J Park, 1992b*] of the corresponding PCs (Figure 4.2c,d).

The first mode (Figure 4.2e) is mainly constrained to the SH. Instead of having the common feature of the Deacon cell (Figure 4.1a), it shows prominent enhanced southward flow between 45°S and 65°S, penetrating to a depth of more than 4000m. As a consequence, the AABW formation in the SO is interrupted to a certain extent, and becomes slightly weakened. Meanwhile, north of 45°S, the upper cell, comprising southward advection of upper circumpolar deep water (UCDW) and northward movement of the Antarctic intermediate water (AAIW), becomes weakened. The second mode has a similar structure in the SO, but resembles the AMOC pattern in the north (Figure 4.2f), with the maximum overturning around 30°N, at a depth of 1000m. In this mode, the southward flows extend from 60°N to 60°S and dominate almost the whole overturning cell above a 4000m depth, except for a northward flow around 40°S, over the top 800m.

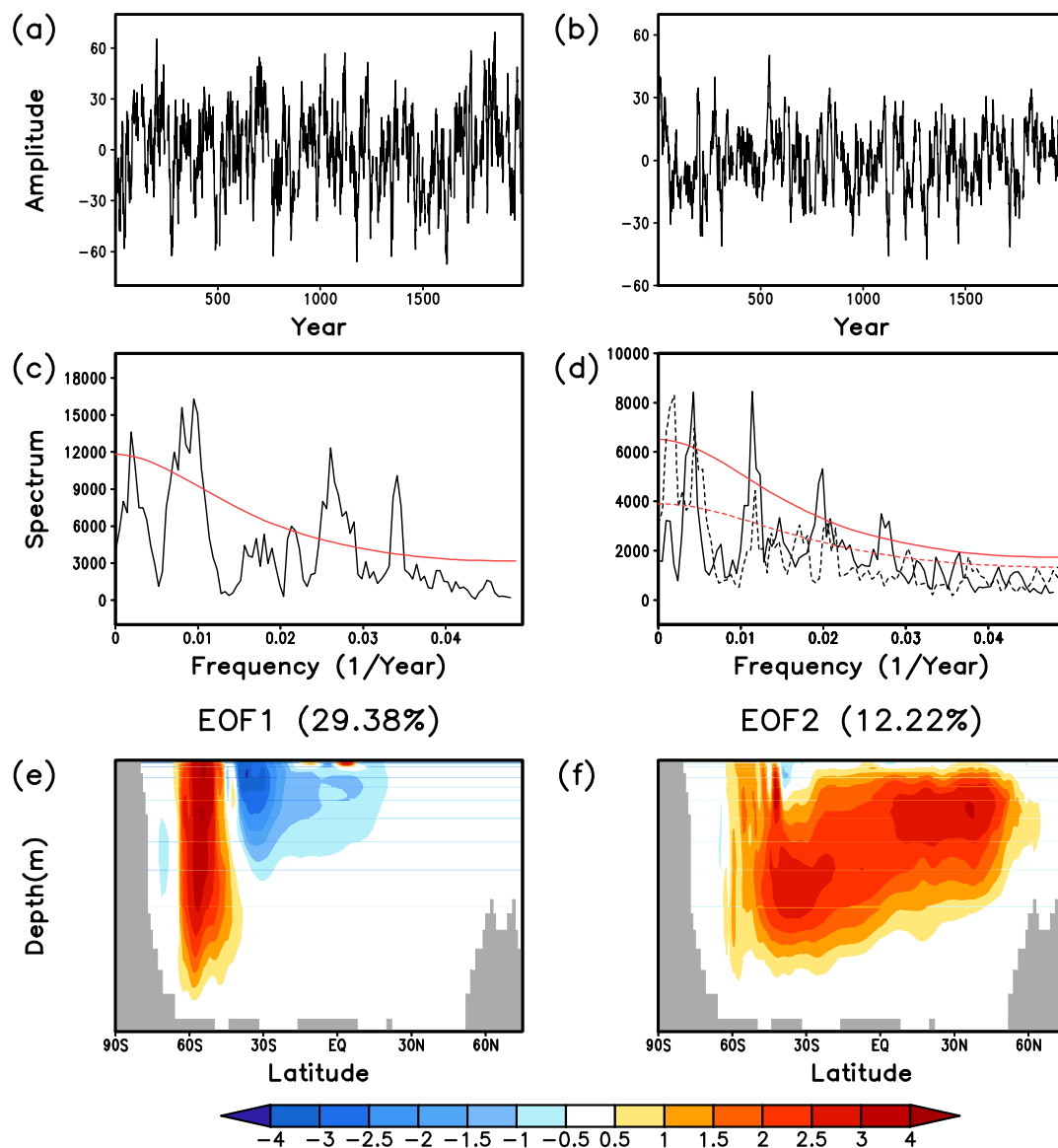


Figure 4.2 EOF analysis of the annual GMOC streamfunction anomaly in the CTL experiment. (a) PC1, (b) PC2, (c) multitaper method (MTM) spectral analysis of PC1 (black) and the 95% significance level relative to the estimated red noise background (red), (d) MTM spectral analysis of PC2 (black solid) and the AMOC streamfunction maximum in 30°N (black dash) with their 95% significance levels (red lines), (e) the first EOF pattern and (f) the second EOF pattern. Here, a linear trend is removed from the data and a 15-year running mean is also applied prior to the EOF analysis.

To investigate the relationship between these modes and the SWW, the composite maps of SWW zonal component u with the corresponding PCs are shown in Figure 4.3. In both modes, the SWW is shifted poleward and enhanced during both the austral winter (June-August) and summer (December-February). The change is much stronger during the austral summer (Figure 4.3b,d). More precisely, in the first mode, the wind anomalies exhibit a zonal symmetric structure and are centered over the adjacent area of the South Pacific and SO, which is bounded by the Drake Passage (Figure 4.3b). Such a pattern resembles the wind anomalies during a positive phase of SAM [e.g. *Lovenduski and Gruber, 2005; Sen Gupta and England, 2006*]. Time series of this mode has the maximum correlation with the SAM indices, which are defined as the difference of zonal mean sea level pressure between 40°S and 65°S [*Gong and Wang, 1999*], when they are in phase. It can be as significant as 0.61 and 0.50 for the austral winter and austral summer SAM indices, respectively. This implies that the GMOC pattern in the first mode is primarily dominated by the SAM associated SWW change. In the second mode, the SWW anomalies are distributed quasi-uniformly over the SO and show the maximum over the Drake Passage (Figure 4.3d), but with much smaller magnitude compared to that in the first mode. It is not surprising that the in-phase wind anomalies in the second mode are relatively smaller, because the response of the AMOC to the SWW change needs at least one centennial [*TL Delworth and Zeng, 2008*]. Detailed explanation of the forcing mechanism for this mode will be given in section 3.4.

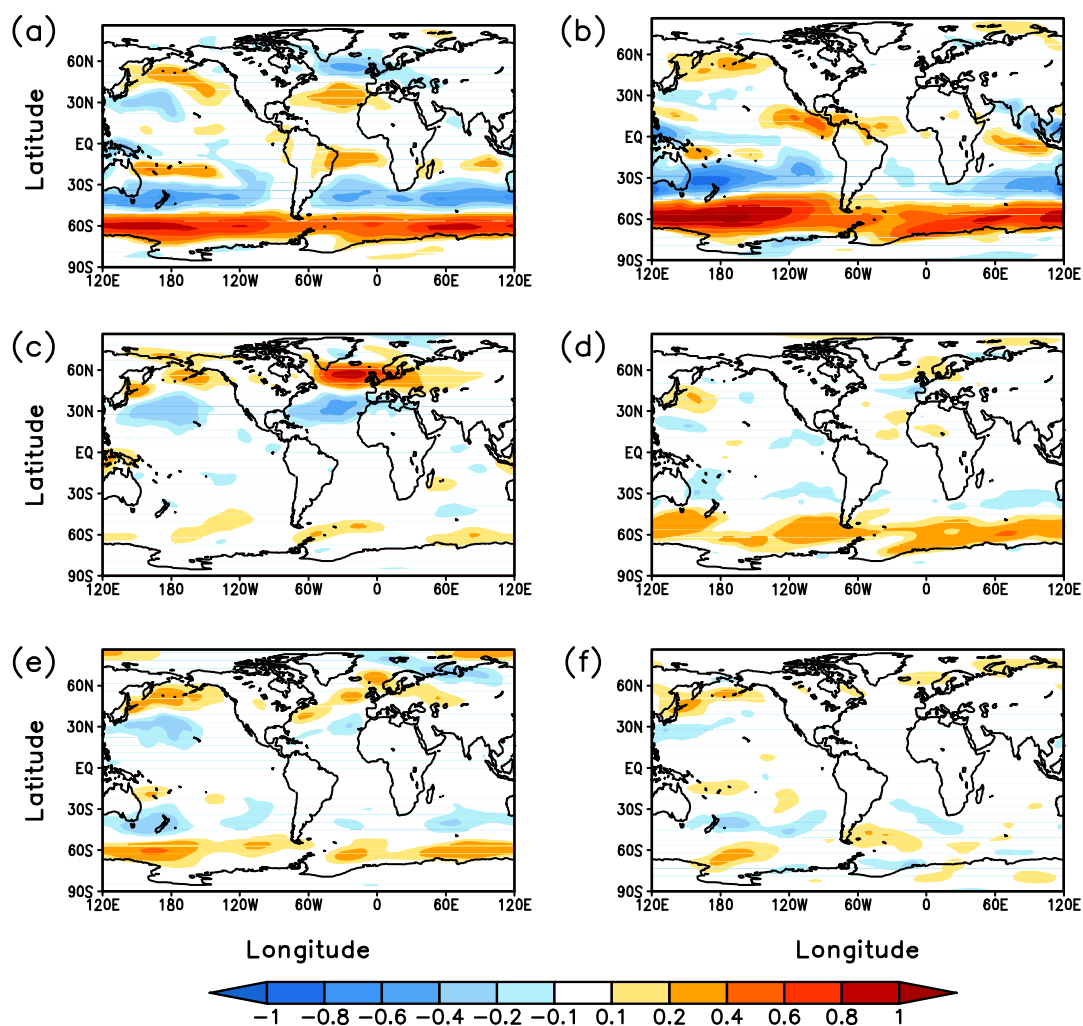


Figure 4.3 Composite maps of the seasonal mean surface zonal wind anomalies (in m/s) with PC1 (a,b) and PC2 (c,d) during austral summer (December-February, left) and winter (June-August, right) in CTL. (e) and (f) are as (c) and (d) but for PC2 lagging the wind field for 305 years. Values with significance higher than 95% using a student t-test are considered.

As mentioned in the introduction, we concentrate mainly on internally induced GMOC variability, possibly linked to SWW anomalies. To exclude any factor that might influence the EOF patterns in the CTL experiment due to different boundary conditions, we apply the same analysis to the H6K experiment. The two dominant EOF patterns (Figure 4.4c,d) in the H6K experiment have a similar structure to those in CTL and explain 28.06% and 17.48% of total variance, respectively. Composite analyses using the PCs (Figure 4.4a,b) with the wind field also demonstrate a

poleward shift and strengthening of the SWW when the GMOC and AMOC anomalies occur (not shown). This indicates that the wind-driven GMOC modes can be found in both present day and mid-Holocene climate conditions and thus is generated through internal interactions in the climate system.

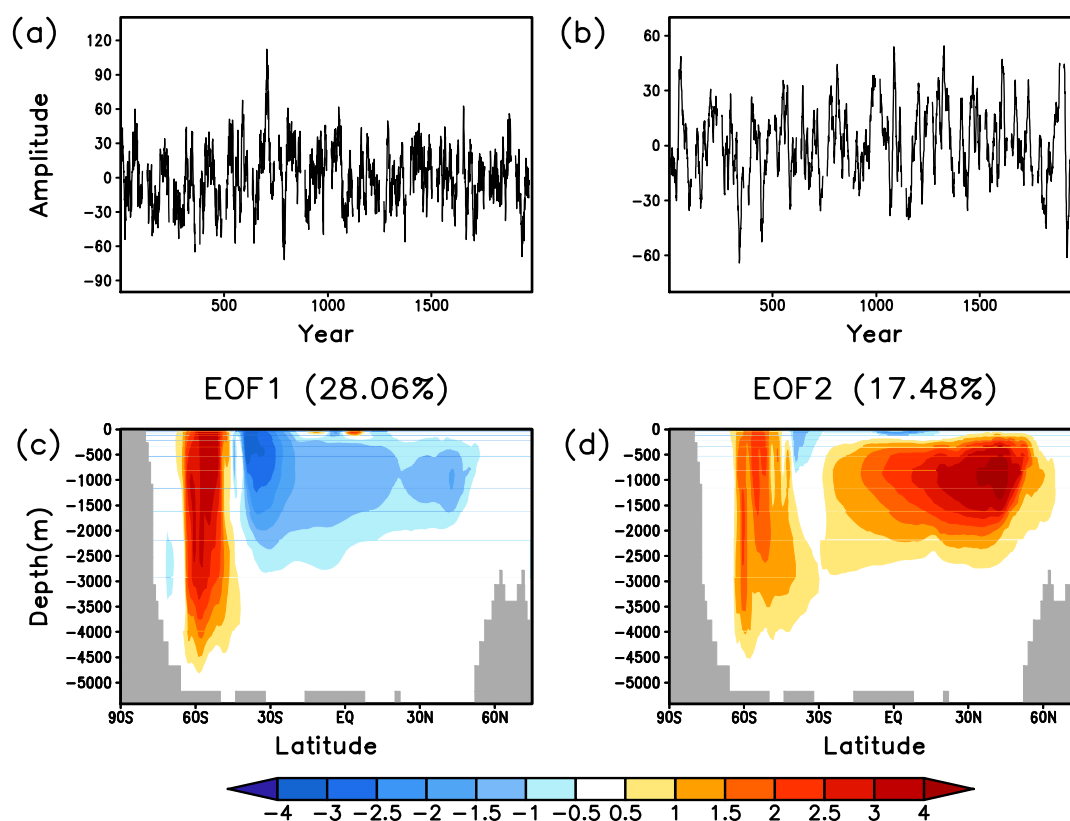


Figure 4.4 EOF analysis of the annual mean GMOC streamfunction anomaly in the H6K experiment. (a) PC1, (b) PC2, (c) the first EOF pattern and (d) the second EOF pattern.

4.3.3 Wind perturbation experiments

The GMOC and AMOC anomalous streamfunctions in the three wind perturbation experiments $W_{x1.5}$, W_{PLWD} and $W_{PLWDx1.5}$ are illustrated in Figure 4.5. Notably, the structure of the GMOC streamfunction anomalies (Figure 4.5a,c,e) seems to be a combination of those in the two EOF patterns from CTL. The wind-induced divergence over the latitude band of the SWW is intensified significantly, which leads

to stronger upwelling over the Drake Passage. North of this band, the southward flow in the intermediate depth has slightly positive anomalies. In the AMOC (Figure 4.5b,d,f), there is an increase in the NADW outflow, along with an increased NADW formation. The magnitude of the GMOC and AMOC streamfunction anomalies shows the maximum in the $W_{\text{PLWDx1.5}}$ experiment, resulting from both poleward shift and intensified SWW. The NADW outflow is approximately 3.6 Sv stronger at a depth of about 2200m than that in CTL. Comparably, the anomalies are 1.9 Sv and 1.3 Sv in the $W_{\text{x1.5}}$ and W_{PLWD} experiments, respectively. This suggests that these two effects related to the SWW are additive, i.e. the patterns derived from $W_{\text{PLWDx1.5}}$ can be obtained as a superposition of the corresponding structures induced by each forcing, for both the global and the Atlantic streamfunctions.

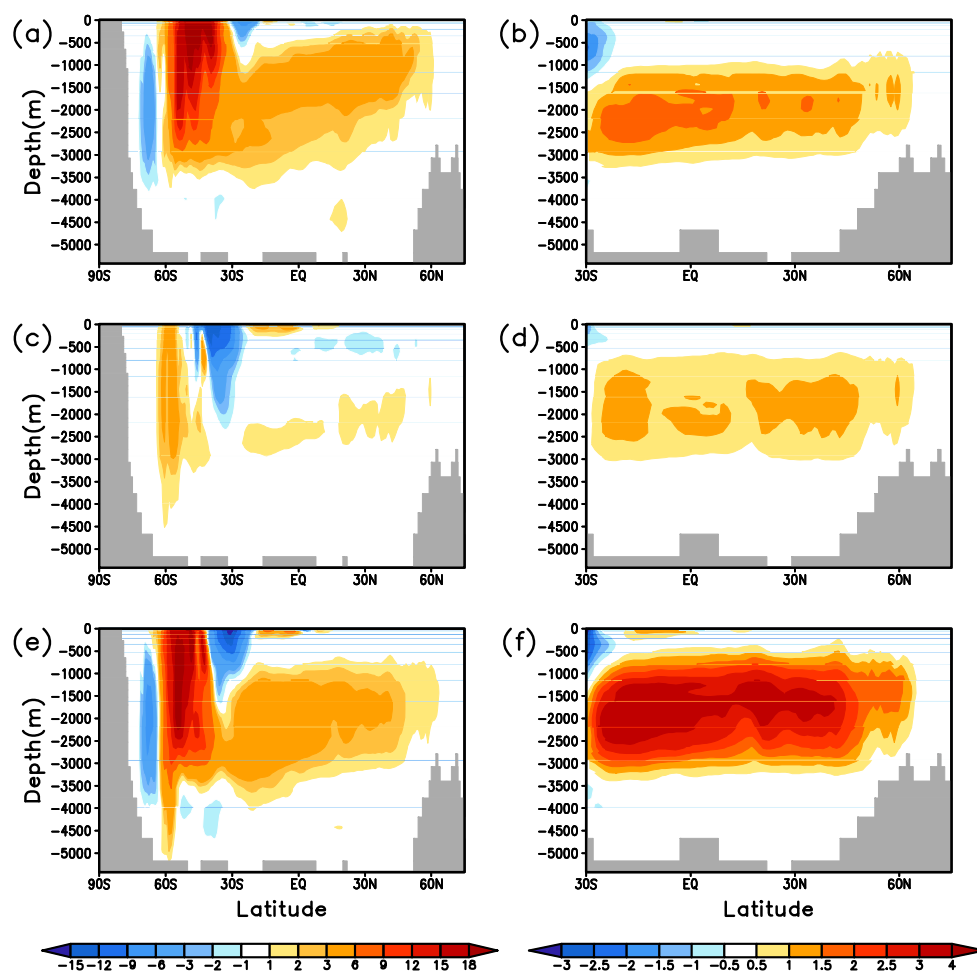


Figure 4.5 Annual mean GMOC (left) and AMOC (right) streamfunction anomalies (in Sv) averaged over the last 200 years of the integration in (a,b) $W_{\text{x1.5}}$, (c,d) W_{PLWD} and (e,f) $W_{\text{PLWDx1.5}}$ relative to CTL.

It is worth mentioning that the strengthening of the NADW outflow and the associated overturning cell in the North Atlantic seems to be compensated by a more pronounced Indo-Pacific upwelling in W_{PLWD} , which leads to no remarkable change in the GMOC streamfunction (Figure 4.5c). This suggests that the Indo-Pacific overturning circulation is likely to be more sensitive to the shift of the SWW than its strengthening. The results reveal that the GMOC and AMOC are sensitive to both types of changes related to the SWW in our simulations.

4.3.4 The SO mode and the NH mode

As seen in Figure 4.2, the first mode shows maximum values south of 30°S , whereby the feature in the NH is more pronounced in the second mode. Furthermore, the SWW anomalies (Figure 4.3) reach the maximum in the adjacent area of the SO and the Indo-Pacific Ocean in the first mode, and distribute quasi-uniformly in the second mode. Thus, we infer that the first mode can be mostly projected onto the SO, especially the longitude band of the Indo-Pacific Ocean, and the second mode onto the Atlantic Ocean. To verify it, we apply the composite analysis to the Indo-Pacific overturning circulation and the AMOC using the two PCs, respectively.

When the first PC is projected onto the Indo-Pacific streamfunction, the overturning pattern (Figure 4.6a) resembles that of the first mode. The stronger SWW cause an enhanced divergence centered on the maximum latitude band of the SWW. This leads to a 3 Sv increase of the upwelling centering around 55°S , close to where the Drake Passage is located. This increased upwelling can extend downward to a depth of more than 4000m. North of 45°S , the enhanced divergence also leads to a decrease of the southward flow above 3000m depth. In contrast, the anomaly in the NH is not pronounced, which implies that response of the Indo-Pacific overturning circulation to SWW change has some years lag with the direct response in the SO. However, when the first PC is projected onto the AMOC, the anomaly is moderate and it shows a slight decrease of the AMOC with a magnitude of less than 0.5 Sv at maximum

(Figure 4.6b). Comparably, the first mode is mainly identified in the SO.

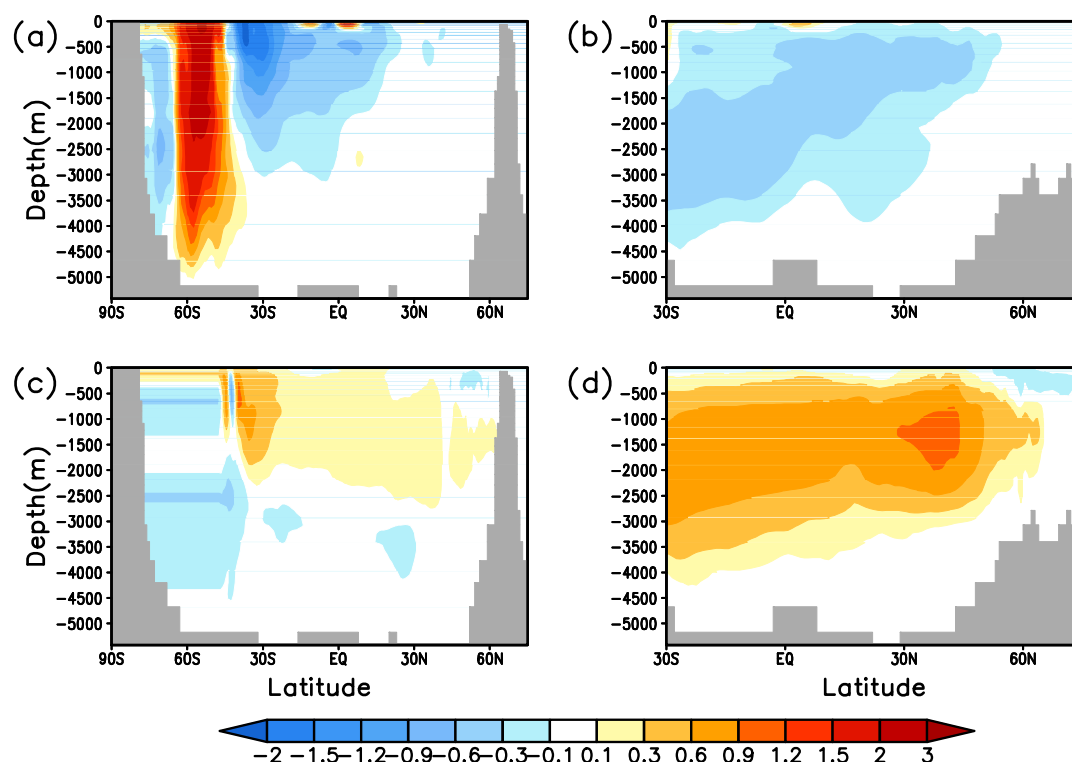


Figure 4.6 Composite maps of the Indo-Pacific streamfunction (left) and AMOC (right) streamfunction anomalies (in Sv) with (a,b) PC1 and (c,d) PC2 in CTL. Values with significance higher than 95% using a t-test are considered.

Contrary to the first mode, the composite maps of the Indo-Pacific streamfunction and AMOC with PC2 (Figure 4.6c,d) demonstrate that the second mode is primarily captured by the Atlantic Ocean. PC2 is highly correlated to the AMOC index (with maximum correlation of 0.47 at 0-lag; not shown). Therefore, spectral analysis of PC2 (Figure 4.2d) shows a similar periodicity with that of the AMOC index. In the second mode, the NADW outflow is strengthened and NADW formation also has an increase of more than 1 Sv (Figure 4.6d). Simultaneously, the upwelling in the North Pacific decreases by approximately 0.2 Sv. A seesaw-like change in the overturning circulation between two ocean basins can be obtained, which has been attributed to the SWW induced decrease in the salinity contrast between the Indo-Pacific and the Atlantic basin in the previous study [*Sijp and England, 2009*]. Here, we refer to this

mode as the NH mode.

The wind anomalies with PC2 (Figure 4.3) are much weaker than those with PC1. Due to the rather long response time for the AMOC to the SWW change [e.g. *TL Delworth and Zeng, 2008*], one can speculate that there might be some lag between PC2 and the wind anomalies. To find the possible lag time, we apply the cross correlation between PC1 and PC2. The correlation coefficient at 0-lag is nearly 0 and there is no strong correlation in other lags. Then a 91-year running mean is applied to both PCs prior to the correlation calculation, which enables us to concentrate mainly on the lag longer than one centennial. Interestingly, the correlation between the filtered PCs (Figure 4.7a) shows a maximum value when PC1 leads PC2 for 305 years, which indicates that the response time of the AMOC to the SWW might be around three centuries. The wind perturbation experiments provide us the possibility to examine this response time. The GMOC and AMOC anomalies in $W_{PLWD \times 1.5}$ within different integration intervals relative to the CTL experiment are illustrated in Figure 4.8. The quick response of the SO to the SWW change can be clearly displayed in the GMOC anomalies (Figure 4.8a-f), with the clear structure formed immediately after the perturbation. Comparably, the AMOC anomalies (Figure 4.8g-l) are characterized by a propagation of SWW-induced NADW outflow strengthening from 30°S to 60°N. After about one decade, the NADW outflow becomes increased. However, in the first 50 years, the SWW anomalies hardly have any influence on the AMOC north of 30°N. It takes at least one century for the anomalies to reach the North Atlantic (Figure 4.8i), which supports the previous view [*TL Delworth and Zeng, 2008*]. However, the AMOC anomalies keep increasing until it reaches the maximum after 300-year perturbation (Figure 4.8j-l), after which the AMOC anomalies are in a similar magnitude (Figure 4.5f). Such an interval strongly matches the 305-year lag time in the cross correlation of PC1 and PC2. Therefore, we conclude that it takes three centuries for a full adjustment of the AMOC to SWW change in our model. The cross correlation of PC1 with AMOC (Figure 4.7b) shows the peak at a same lag with that of PC1 and PC2 and further supports our finding.

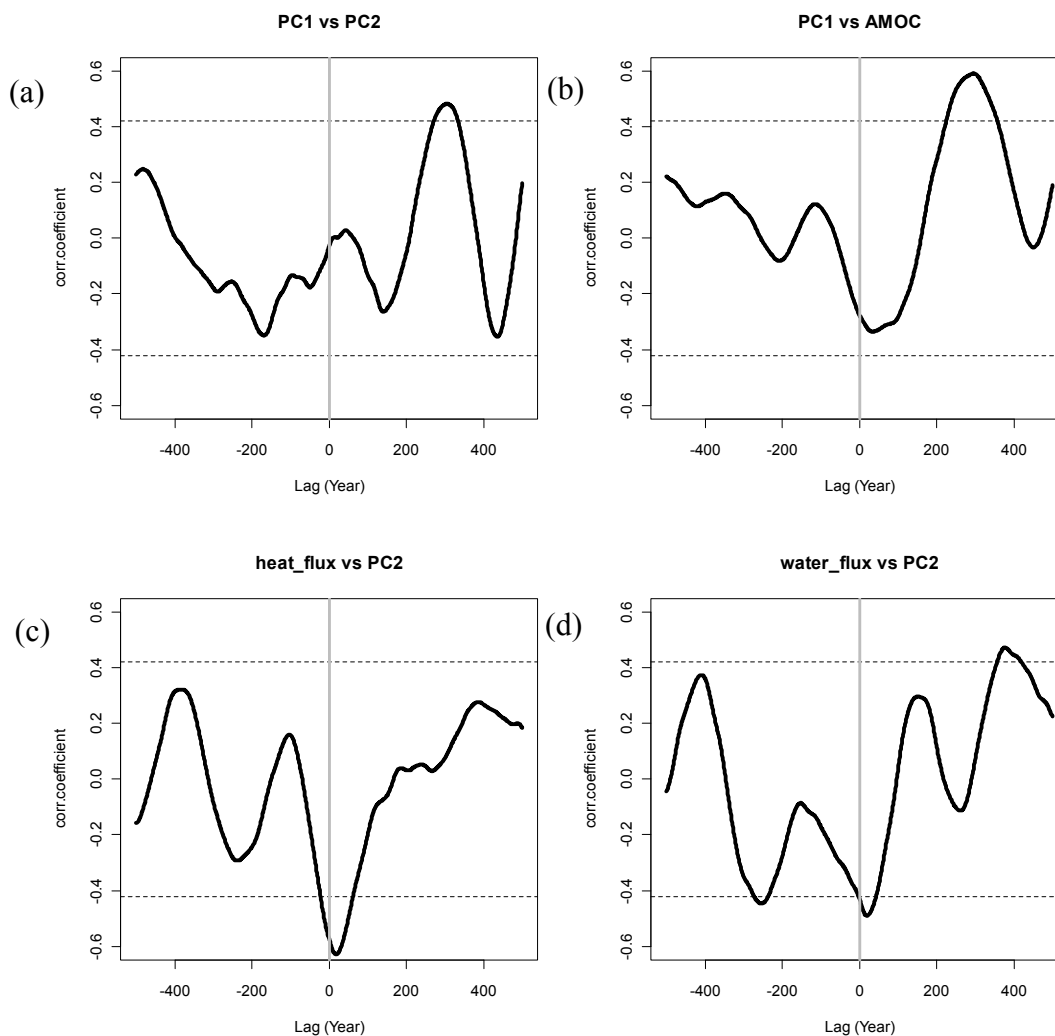


Figure 4.7 Cross correlation of (a) PC1 and PC2, (b) PC1 and AMOC streamfunction maximum in 30°N , (c) surface downward heat flux and PC2 and (d) net freshwater flux into the ocean including the river runoff with PC2. Here time series of PC1 and PC2 have been filtered by a 91-year running mean prior to the correlation calculation. The heat flux and freshwater flux time series are averaged over the region $55^{\circ}\text{-}15^{\circ}\text{W}$ and $50^{\circ}\text{-}70^{\circ}\text{N}$, and then filtered by the same strength with PCs. The dashed lines indicate the 95% significance level when 20 degrees of freedom are selected concerning the autocorrelation in the time series. Positive lags (in year) indicate that the first time series leads the second one and vice versa.

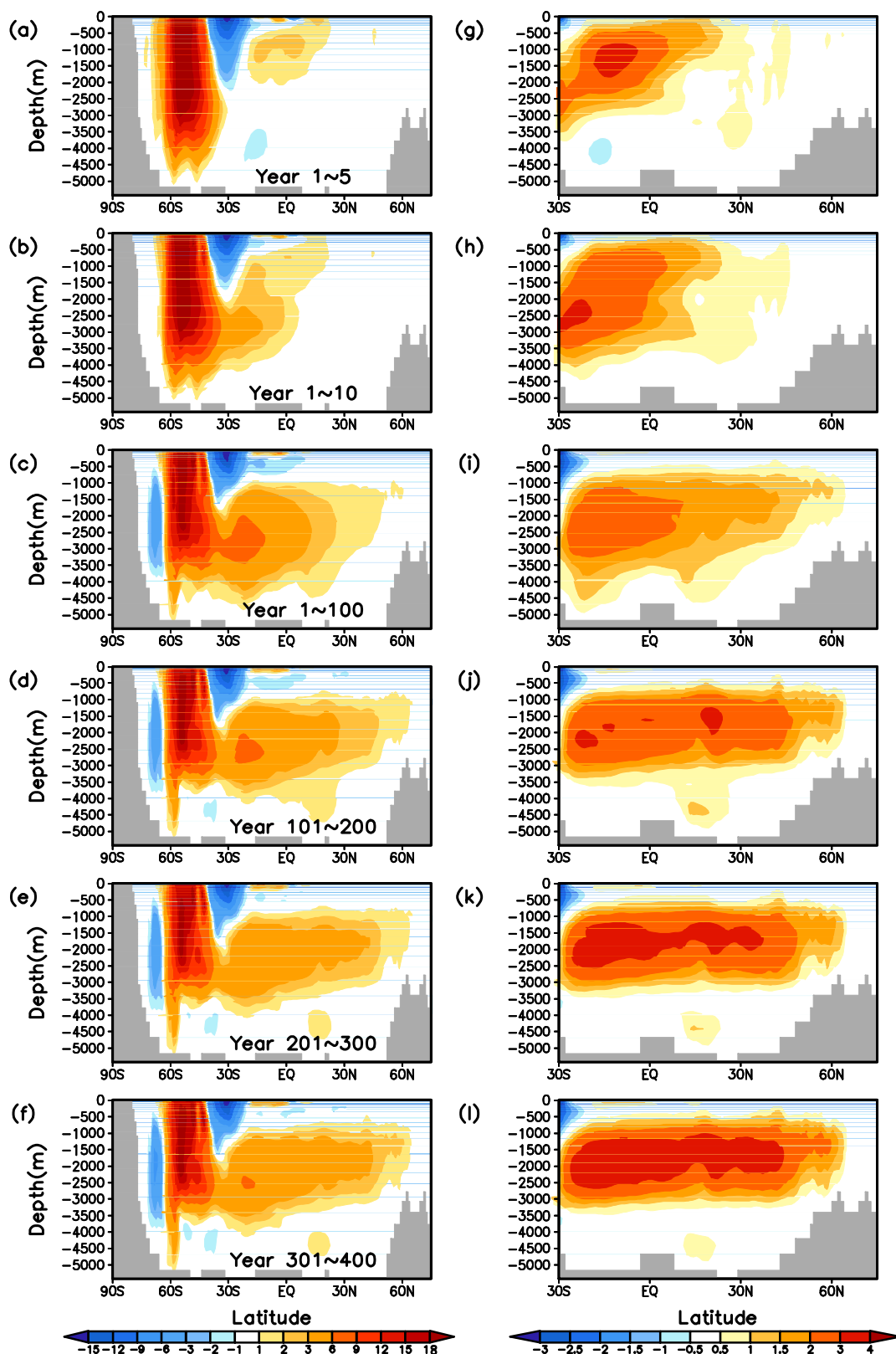


Figure 4.8 Annual mean (a-f) GMOC and (g-l) AMOC streamfunction anomalies (in Sv) in $W_{\text{PLWDx1.5}}$, relative to CTL. The numbers of year indicate the integration time after the perturbation.

Based on this interval, we calculate the composite maps of PC2 with the wind field at 305-year lag. The wind anomalies (Figure 4.3e,f) resemble those with PC1 (Figure 4.3a,b), but are still much smaller in the magnitude. This result suggests that the NH mode can also be controlled by other forcing factors. Thus, the cross correlations of surface downward heat flux and freshwater flux including the river runoff with PC2 are also shown (Figure 4.7c,d). Here, the time series of these two indices are constructed according to Delworth and Greatbatch [2000] by averaging over the region 55° - 15° W and 50° - 70° N, where the NADW formation takes place. PC2 is highly correlated to both indices, showing the highest coefficients of -0.63 when the heat flux leads PC2 by 18 years, and -0.49 when the freshwater flux leads PC2 by 19 years (Figure 4.7c,d). It indicates that the second mode, which resembles the AMOC, is driven by a combined effect of different forcing. However, an entire understanding of the controlling mechanism for the AMOC is beyond the scope of this study.

4.3.5 Response of the SST and the sea ice to different modes

As the SWW strengthens, the SSTs associated with the two modes are affected differently (Figure 4.9). Notably, SST change over the latitude band of the SWW has much similarity in both modes: the Atlantic sector experiences a temperature increase by as much as 0.5°C , while the Pacific sector is slightly colder (Figure 4.9a,b). South of this band, the stronger upwelling results in a slight warming in the SO, which in turn decreases the sea ice thickness in the associated regions (Figure 4.9c,d). However, north of this band, the SST response to the SWW change in the two modes seems to be the opposite. In the SO mode, the SST anomaly is mainly negative, except in the Labrador Sea and the Norwegian Sea (Figure 4.9a). One notes the prominent zonal SST dipole in the SH resembles the SAM associated SST anomaly pattern from the previous studies [Sen Gupta and England, 2006; 2007]. Meanwhile, intensified upwelling in the tropical and sub-tropical Pacific Ocean generates a strong cooling there, due to increased Ekman transport associated with stronger SWW. In the NH

mode, warmer SST covers almost the whole North Atlantic and North Pacific (Figure 4.9b), which is caused by increased northward heat transport associated with the strengthened AMOC in the North Atlantic and less cold deep water upwelling due to the weakened overturning circulation in the North Pacific. This leads to a decrease in the sea ice thickness over the North Pacific (Figure 4.9d).

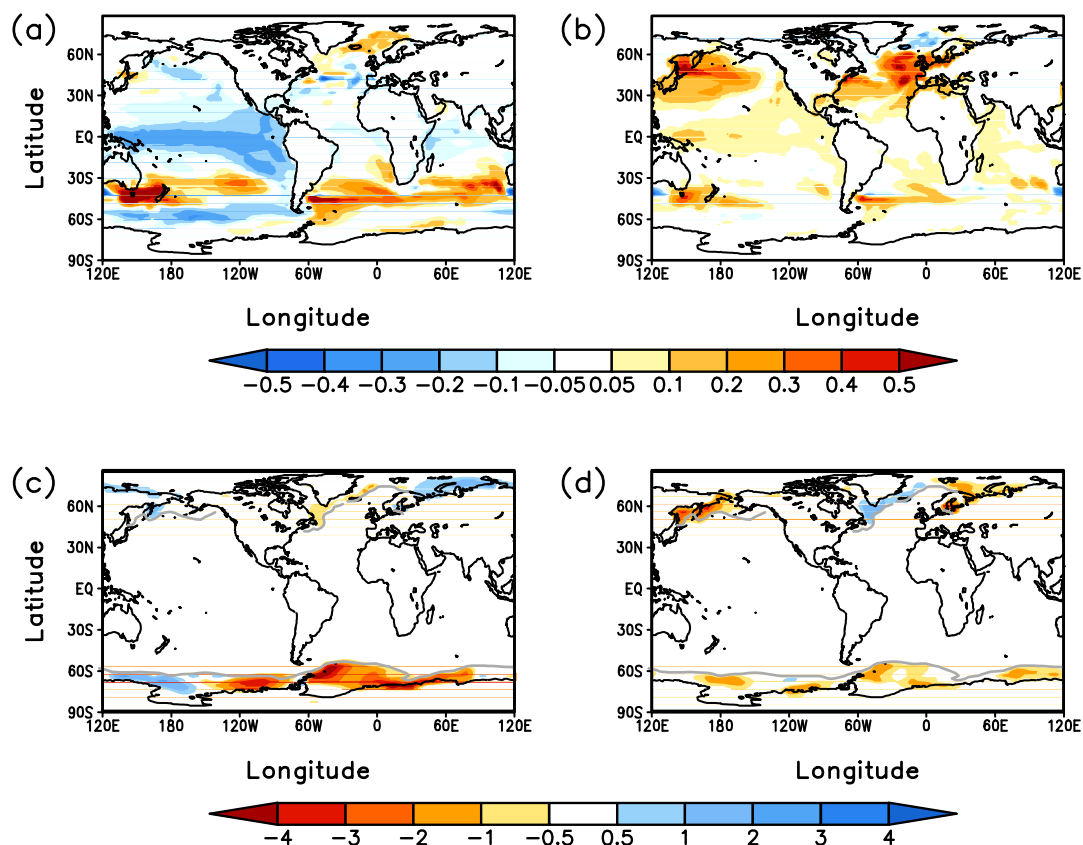


Figure 4.9 Composite maps of the annual mean SST anomalies (in °C) with (a) PC1 and (b) PC2 in CTL. (c) and (d) are as (a) and (b) but for the sea ice fractionation anomalies (in %). The sea ice coverage boundary in CTL is also shown (grey solid line). Values with significance higher than 95% using a student t-test are considered.

4.4 Discussion

In this study, we have presented two distinct multidecadal-to-centennial modes of the GMOC, which result from internal variability of the climate system in the Earth system model COSMOS. The physical mechanism providing the necessary energy to

sustain an overturning circulation [Kuhlbrodt *et al.*, 2007] is a crucial aspect in the GMOC and AMOC. Besides diapycnal mixing [Jeffreys, 1925; Munk and Wunsch, 1998; Prange *et al.*, 2003; Rahmstorf *et al.*, 2005], the SWW induced divergence [J Toggweiler and Samuels, 1998; Gnanadesikan *et al.*, 2005; Schewe and Levermann, 2010] is one of the driving mechanisms. We examined through the analyses of long-term integrations as well as sensitivity experiments that both the SO mode and the NH mode of the GMOC in our simulations are linked to natural variations of the SWW. This internal variability can generate a strengthening and deepening of the Deacon Cell in the SO. Furthermore, strengthening or poleward shift in the SWW can cause considerable increase in the AMOC. Different internal AMOC patterns has been found in a previous study [W Park and Latif, 2008], where the authors propose a North Atlantic source of multidecadal variability and a SO controlled multicentennial variability of the AMOC in their multimillennial control integration. They argue that both of them are associated with sea ice changes.

Results from the mid-Holocene experiment show that the two modes of the GMOC have the analog structure with that in the CTL experiment, although GMOC and AMOC streamfunctions have different magnitudes compared to their present values. The mechanisms found are valid for pre-industrial as well as mid-Holocene conditions, indicating its independence on the climate background conditions during the Holocene. A natural next step would be the analysis of different climate states with strongly deviating background conditions [e.g., C Rühlemann *et al.*, 2004].

The modes identified here may mask any changes and ongoing trends in the GMOC, and therefore, it is important to understand the underlying mechanisms. Changes in the SWW can directly cause a rapid and pronounced local response in SO. In the SO mode, we can see that the intensified and poleward shifted SWW lead to a stronger local divergence through increased downward Ekman transport, which permits an increased northward flow at the surface north of the latitude band of the SWW and a deepening and strengthening of the Deacon cell over the latitude band of the Drake Passage. The wind anomaly structure associated with this mode resembles that in a positive phase of the SAM. Furthermore, the strong in-phase correlation between the

SAM and time series of SO mode enables us to conclude that the SO mode is directly driven by a SAM-like SWW change. Many previous studies [e.g., *J R Toggweiler and Samuels, 1993; Gnanadesikan and Hallberg, 2000; Hirabara et al., 2007; Sijp and England, 2009*] have examined the relationship between the SWW induced SO overturning circulation change and AMOC variation. The basic mechanism can be explained as follow: the wind-induced increased Ekman transport, on one hand, leads to enhanced ventilation in the SO [*Russell et al., 2006; TL Delworth and Zeng, 2008*]. Stronger upwelling removes the deep water and increases the outflow from north to the SO, which needs to be compensated by more deepwater formation in the north. The North Atlantic is considered the only deep water formation place north of the latitude band of SWW [*J Toggweiler and Samuels, 1995*]. Thus, the NADW formation is expected to strengthen, which has been captured by the NH mode in our simulation. On the other hand, the increased Ekman transport pushes more water to move northward and be injected into the AAIW, and results in a deepening of the thermocline [*Gnanadesikan and Hallberg, 2000*]. As a consequence, the NADW formation increases, which in turn increases the NADW outflow and ventilation in the SO. Santoso et al. [2006] analyze the natural variability of the Circumpolar Deep Water using their long integration of a couple GCM, and find that the NADW formation is mainly buoyancy driven, but with a weak connection with the SWW on multicentennial time scales. We show that the NH mode, mainly projected onto the AMOC, is driven by a combination of wind forcing and buoyancy forcing, with the buoyancy dominating. Furthermore, we highlight that the impact of the SWW on the AMOC needs three centuries to reach the full adjustment. Results from our wind perturbation experiments are also consistent with their argument that the SWW has a more direct influence on the NADW outflow [*Santoso et al., 2006*].

A number of factors for the wind-induced GMOC need to be taken into account. One is linked to the uncertainty in the parameterization of mesoscale eddies in the SO. Coarse resolution models without resolving these eddies can exaggerate the effect on the wind-induced Ekman transport [e.g. *Straub, 1993; Hallberg and Gnanadesikan, 2006; Böning et al., 2008; R Farneti et al., 2010; Riccardo Farneti and Delworth,*

2010]. The eddy-induced contribution is important for the water mass transport in the vicinity of the ACC, since it balances the horizontal northward Ekman transport as well as the vertical Ekman pumping [*J. B. Sallée et al.*, 2008]. The heat flux induced temperature change can also be reversed in an eddy-saturated ocean state compared to the direct influence from the SWW change [*Hogg et al.*, 2008; *Screen et al.*, 2009; *Spence et al.*, 2010], because the total heat flux response is more in an eddy-permitted model setup than that in a coarse resolution one by a factor of 2 [*Hogg et al.*, 2008]. *Treguier et al.* [2010], however, report that an increase of overturning circulation as a response to SH wind is due to the time-mean component and is compensated by an increased buoyancy gain at the surface. We suggest that the internal variability of the GMOC associated with the SWW change on longer timescales needs to be considered including the role of mesoscale eddies, in order to understand GMOC changes under past, present and future climate conditions.

The cold temperature response in the tropical and sub-tropical Pacific Ocean related to the SO mode (Figure 4.9a) is due to intensified upwelling in the Pacific and Indian Oceans (Figures 4.2e, 4.6a). SST shows a large-scale zonally asymmetric response between the Atlantic and Pacific-Indian Oceans (Figure 4.9a) caused by wind-induced changes (Figure 4.3a,b) at the mixed-layer depth. Enhanced upwelling over the latitude band of the SWW pumps more cold recirculated deep water to the surface and causes negative SST anomalies west of the Drake Passage (Figure 4.9a). Similar asymmetric heat budgets were observed recently by *Sallée et al.* [2010] in relation to the Southern Annular Mode (projecting strongly onto Figure 4.3a,b). The stratification exhibits opposite anomalies over the South Atlantic Ocean. Positive SST anomalies in the South Atlantic Ocean in the NH mode can be furthermore potentially linked to increased AMOC transports of warm and salty Indian Ocean waters into the cold and fresh South Atlantic. There is evidence from modeling studies [*De Ruijter*, 1982; *Biastoch et al.*, 2009] manifesting that this interbasin transport can be modulated by change in the SWW, e.g. a poleward shift can result in a warming in the South Atlantic, which affects the AMOC on decadal timescales [*Biastoch et al.*, 2008]. Such effect may be also relevant for an onset of a strong present AMOC from the weaker

glacial mode during deglaciation [Knorr and Lohmann, 2003; 2007].

The wind perturbation experiments demonstrate that the GMOC and AMOC are sensitive to the SWW change in our model and capture features of the observed system. A 1.5 times amplified SWW in $W_{x1.5}$ and 3.5° southward shift of the SWW in W_{PLWD} result in an intensifying of the divergence over the latitude band of the SWW (Figure 4.5a,c), as can be seen in the SO mode. The corresponding AMOC in both experiments acts to reinforce (Figure 4.5b,d). In the recent IPCC report, the AR4 models (as a group) predict a 25% intensification and 3.5° poleward shift of the SWW [Fyfe *et al.*, 2007], which is comparable to the SWW change in $W_{PLWDx1.5}$. $W_{PLWDx1.5}$ shows an intensified northward Ekman transport across the ACC and increased upwelling over the SO, consistent with the SO overturning circulation response to the SWW change in IPCC AR4 runs [Fyfe and Saenko, 2006]. However, the AMOC in the $W_{PLWDx1.5}$ experiment strengthens by more than 3 Sv, which is contrary to the predicted weakening of the AMOC in most IPCC runs that results from the increase of anthropogenic CO₂ release [e.g., Schmittner *et al.*, 2005].

Paleo-study based on model-data comparison [Varma *et al.*, 2011] indicates that the centennial-scale variability in the SWW during the Holocene can be caused by the change in solar forcing, which implies possible application of the modes found in this study to understand the past GMOC change. From the future perspectives, CO₂ induced warming in the North Atlantic might overlay the AMOC response to the poleward-intensifying SWW. However, it is unclear whether the response of the overturning circulation in the NH takes longer or is more pronounced than changes induced in the south [Klinger and Cruz, 2009]. The observed SAM undergoes a pronounced upward trend in the last 50 years [Marshall, 2003], which has been attributed to stratosphere ozone depletion [e.g. Thompson and Solomon, 2002] and greenhouse gas increases [Hartmann *et al.*, 2000; Marshall *et al.*, 2004]. This trend is also related to the observed increase in the SWW. In the same period, the Antarctic in general experiences a small warming trend, but with distinct regional difference [Turner *et al.*, 2005]. Driven by surface warming and freshening, a decrease in the projected subduction of SO upper-water masses implies a slowdown in the SO

circulation in the future [Downes *et al.*, 2010]. A reduction in the subduction of intermediate waters affects the ocean's capacity to sequester heat and carbon and would work against changes in the wind-induced variations in Southern Ocean.

4.5 Conclusions

Identification of the link between the SWW and the two leading modes in the internal variability of the GMOC on multidecadal and centennial timescales enables us to confirm that, the winds play an essential role in modulating the GMOC. Strengthening and poleward shift of the SWW generate a direct response in the SO, with Ekman transport enhanced and the Deacon Cell strengthened. Such a change in the SO circulation produces an increase of the NADW outflow in one decade, eventually propagating this anomaly to the North Atlantic Ocean after centuries.

5. Caribbean climate variation during the Holocene

In this chapter, we focus on the Holocene climate variation in the Caribbean. The main feature of the Caribbean climatology during the Holocene will be discussed in section 5.1, based on model-data comparison. Section 5.2 deals with the Caribbean climate variability on seasonal and interannual to centennial timescales. Proper statistical analyses enable us to identify the forcing mechanisms controlling the climate variability on different timescales in the Caribbean region.

5.1 The Caribbean climatology during the Holocene

As introduced in chapter 1, the orbital parameters and the LIS related change can have considerable influence on the NH mid-to-high latitude climate. Comparably, their influence on the tropical and subtropical regions is moderate, except in the monsoon areas [e.g. *Braconnot et al.*, 2007; *Carlson et al.*, 2008; *Renssen et al.*, 2010]. Concerning the Caribbean region, this influence is even minor, with the annual mean temperature anomalies smaller than 1°C [*Braconnot et al.*, 2007; *Carlson et al.*, 2008]. Results based on the proxy studies [*C. Rühlemann et al.*, 1999; *Lea et al.*, 2003; *Giry*, 2011; *Giry et al.*, 2011] reveal that there is a cooling trend (Figure 5.1) during the Holocene in the Caribbean, but its magnitude is still controversial. Compared with the temperature change, the hydrological cycle in the tropical Atlantic region during the Holocene shows a more striking feature, with a gradual southward migration of the Intertropical Convergence Zone (ITCZ) in this period [*Haug et al.*, 2001].

Considering the relative small quantity of high resolution proxy data in the Caribbean during the Holocene, the paleo-modeling effort for this specific region is even less. In this section, we will present the simulated climatology change in the Caribbean during the Holocene.

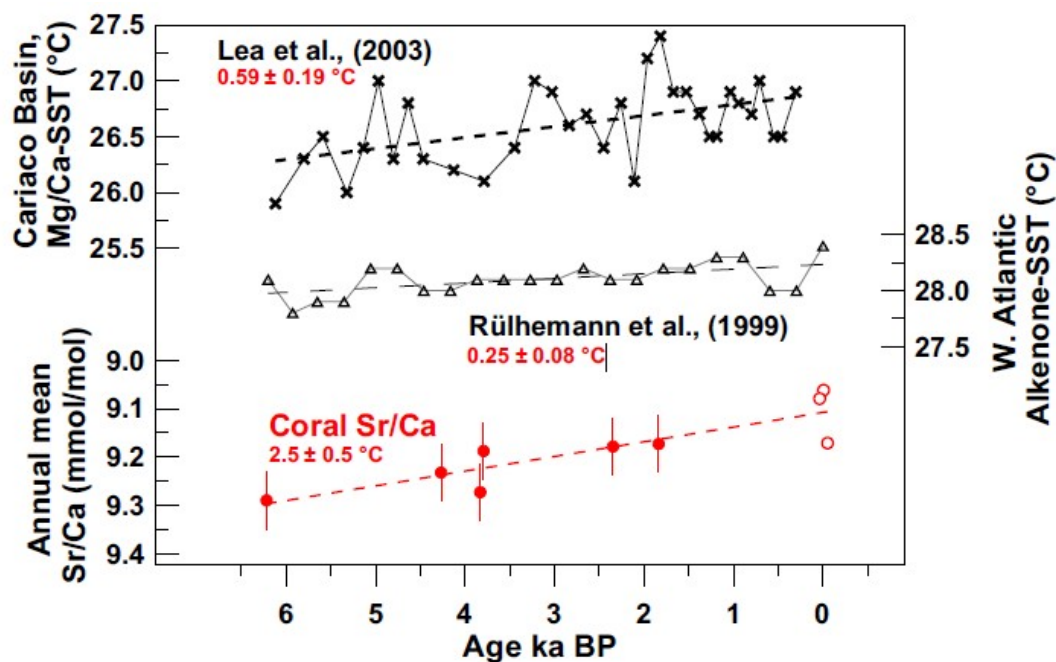


Figure 5.1 The SST trend during the mid- to late Holocene based on different proxy in the Caribbean. Figure from Giry [2011].

5.1.1 Caribbean climatology in the present

5.1.1.1 Observed climatology

The Caribbean region ($8.75^\circ\text{-}25.25^\circ\text{N}$ and $88.75^\circ\text{-}58.75^\circ\text{W}$) consists of the Caribbean Sea, its islands and the surrounding coasts. The region is located southeast of the Gulf of Mexico and North America, east of Central America, and to the north of South America. Its climate is tropical, moderated to a certain extent by the prevailing northeast trade winds, which flow almost constantly over the year (Figure 5.2). These trade winds bring huge amount moisture from the tropical and sub-tropical Atlantic to the Caribbean by advection.

The annual surface air temperature varies slightly over the year in the Caribbean region. The seasonal difference is not as obvious as mid-high latitudes, ranging from 24°C to 30°C (Figure 5.2). The SST variation ranges from 25°C to 30°C (Figure 5.3). The seasonal expansion of the Atlantic Warm Pool (AWP), a warm water body with

temperatures higher than 28.5°C covering the Gulf of Mexico, the Caribbean Sea, and the western tropical North Atlantic (Figure 5.3), has been considered to be the main source of the moisture for the Caribbean [Wang and Lee, 2007]. The AWP is also highly associated with the Atlantic Hurricanes [Wang et al., 2006; Wang and Lee, 2007], which makes the Caribbean an especially vulnerable place.

The Caribbean region locates in the area where the seasonal variation of the ITCZ over Mesoamerica and northern South America controls the pattern and timing of the rainfall [Figure 5.4; Haug et al., 2003]. In previous studies [e.g., Taylor et al., 2002; Angeles et al., 2007], the division of the rainfall seasons, rather than the conventional four seasons, is made according to the amount of the rainfall: a long rainy season from May through October and the dry season, corresponding to boreal winter in most parts of the Caribbean. In the southernmost part, the precipitation occurs primarily from November to next January [Jury et al., 2007]. Even during the rainy season, however, the precipitation range fluctuates greatly within different sub-regions. Thus, in this study, we still use the conventional division of the rainfall seasons to avoid the complexity and confusion, which might occur when we analyze the spatial pattern of the rainfall with the other climatic parameters.

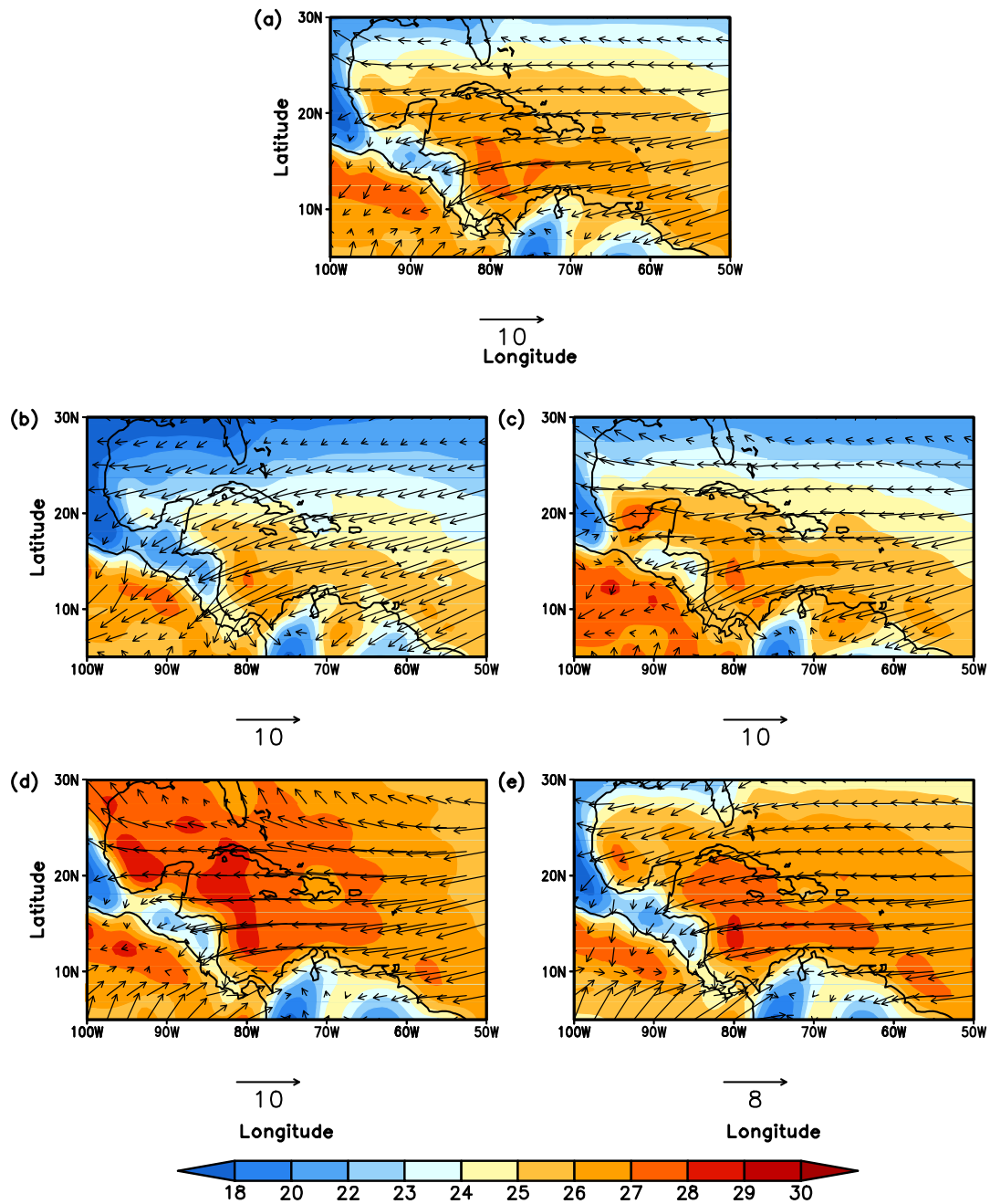


Figure 5.2 Spatial patterns of the surface air temperature (in °C) and winds (in m/s) in the Caribbean based on the NCEP/NCAR reanalysis dataset [Kalnay *et al.*, 1996], averaged over the period 1948-2010 for (a) annual, (b) December-February (DJF), (c) March-May (MAM), (d) June-August (JJA) and (e) September-November (SON).

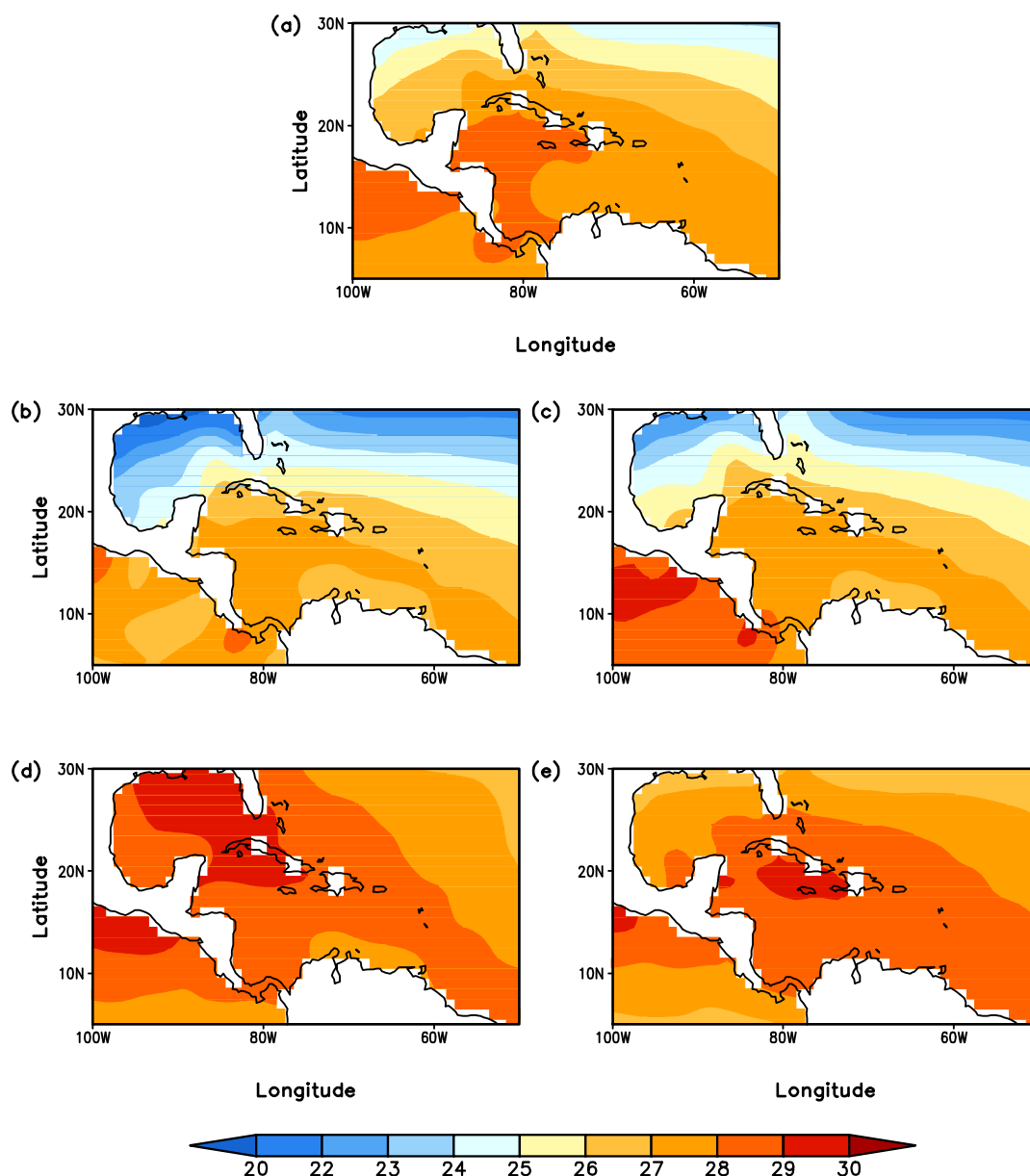


Figure 5.3 Spatial patterns of the sea surface temperature (in °C) in the Caribbean based on the HadISST dataset [Rayner *et al.*, 2006], averaged over the period 1948-2010 for (a) annual, (b) DJF, (c) MAM, (d) JJA and (e) SON.

Rainfall in the Caribbean region undergoes a very distinct annual cycle. Giannini *et al.* [2000; 2001] classified the Caribbean rainfall into three regimes based on EOF analysis of 188 stations centered around the Central America. Jury *et al.* [2007] found four geographically distinct precipitation regions by applying the factor analysis to 35 meteorological stations encompassing the Caribbean region. Here, the distinct annual rainfall cycle can be also seen from the climatology in Bonaire and Cuba (Figure 5.5),

where the proxy archives used in this study are located. In Cuba, the rainfall is best characterized by its bimodal nature, with an initial peak in May–June and the second in September–October. This is the main feature possessed by the whole Caribbean [Chen and Taylor, 2002; Jury et al., 2007]. While in Bonaire, it is more unimodal. It is consistent with the southern Caribbean rainfall annual cycle based on different classification in the previous studies [Giannini et al., 2000; Giannini et al., 2001; Jury et al., 2007].

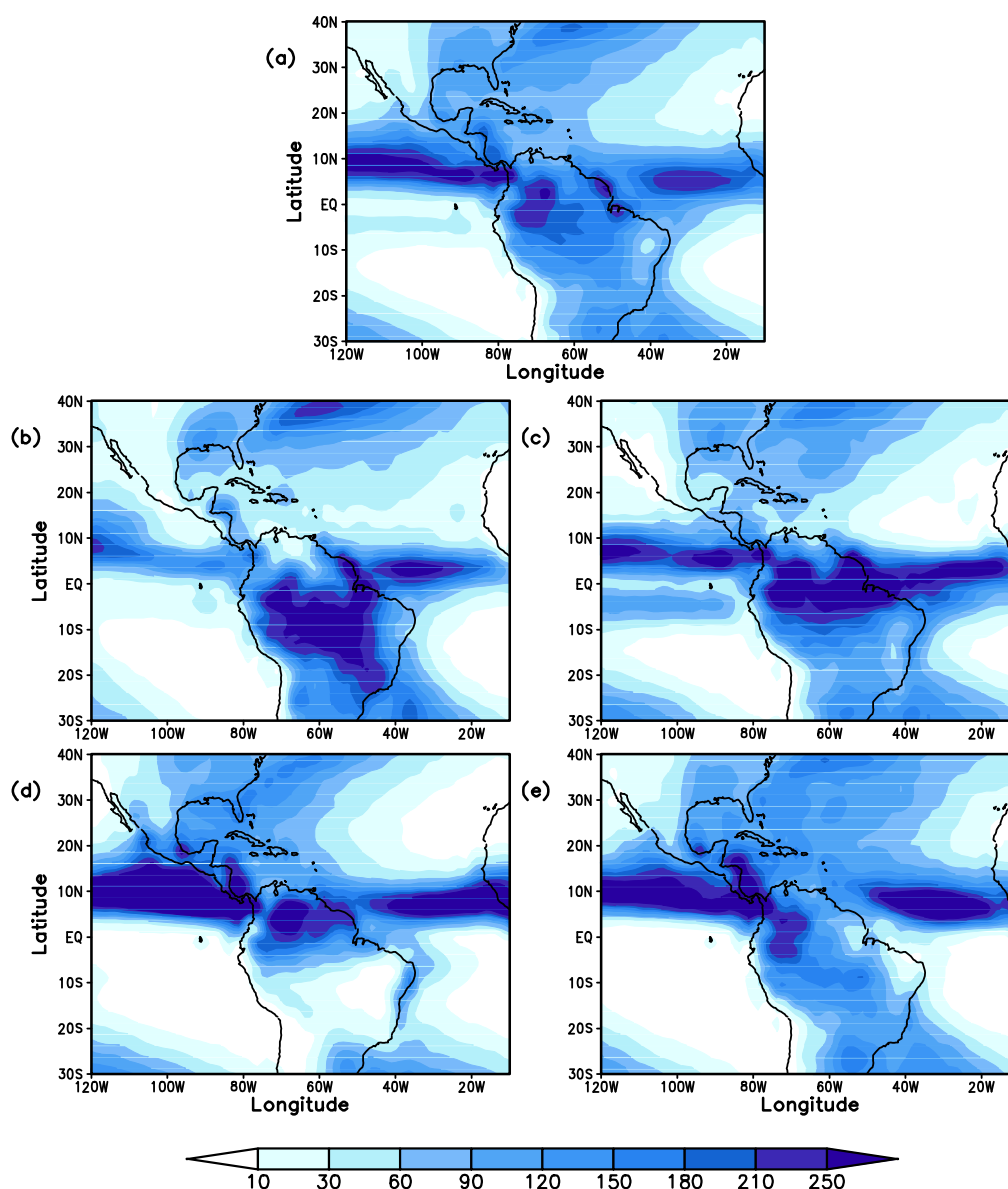


Figure 5.4 Spatial patterns of the precipitation (in mm/day) in the Caribbean based on the CMAP dataset [Xie and Arkin, 1997], averaged over the period 1948-2010 for (a) annual, (b) DJF, (c) MAM, (d) JJA and (e) SON.

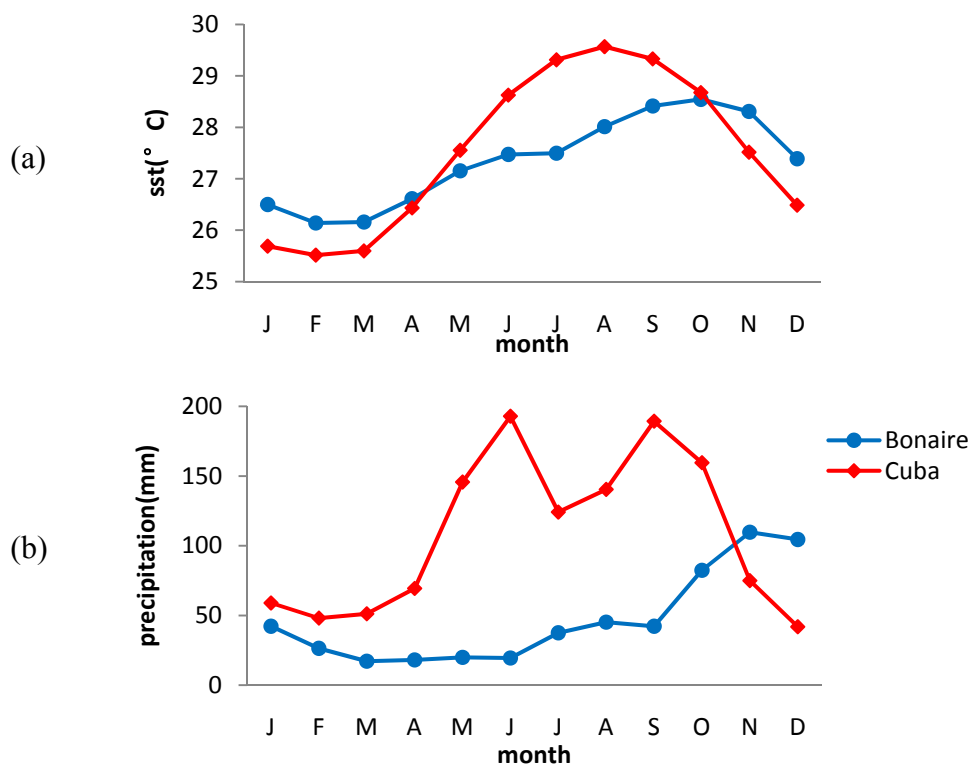


Figure 5.5 Observed HadISST SST [Rayner *et al.*, 2006] (in °C) and Hulme-CRU precipitation [Hulme *et al.*, 1998] (in mm/month) annual cycle in Cuba (red) and Bonaire (blue) averaged over the period 1900-1998.

The relationship between precipitation and local SST can be explained by the SST threshold for convection theory. Previous studies observed [Waliser and Graham, 1993; Folkins and Braun, 2003], based on statistic analyses, that 26.5°C is a threshold for convection. When the SST is below this threshold, the convection intensity has little sensitivity to changes in SST change. But it increases dramatically as the SST increases from 26.5 to 29 °C and decreases again with higher values [Angeles *et al.*, 2007].

During winter (DJF) and spring (MAM), the climatological condition in most of the Caribbean is characterized by SST below or close to the convection threshold (Figure 5.3b,c), which cannot support enough convective activities. Subsidence, which is associated with the spreading of the subtropical high from the Atlantic Ocean to the cool North American landmass, dominates the Caribbean basin in these seasons. Subsidence results in the divergence in the surface (Figure 5.6), with winds, and

moisture transport, directly away from the Caribbean basin, to the south-west, onto the eastern Pacific ITCZ, and to the north-east, toward the Atlantic. Correspondingly, the precipitation in these seasons is relatively less (Figure 5.4b,c). During summer, with the warm pool in the northern Tropical Atlantic spreading gradually eastward, the SST can reach the upper limit of the threshold (Figure 5.3d), which results in the early rainfall season (May-July) in Cuba (Figure 5.5b). The high SST around Cuba lasts until the late winter and so is the high precipitation (Figure 5.5). The mid-summer break of precipitation (Figure 5.5b) can be explained by the temporary intensification of the North Atlantic High [Portig, 1965; Hastenrath, 1976], which strengthens divergence over the basin [Knaff, 1997]. The annual cycles of precipitation and SST in both locations fit quite well, especially in Bonaire (Figure 5.5). The precipitation shows a one-to-two-month lag with the SST (Figure 5.5). The one-month-lag correlation coefficients of the precipitation and the SST for the 100-year monthly data can be as high as 0.5 and 0.53 for Cuba and Bonaire, respectively.

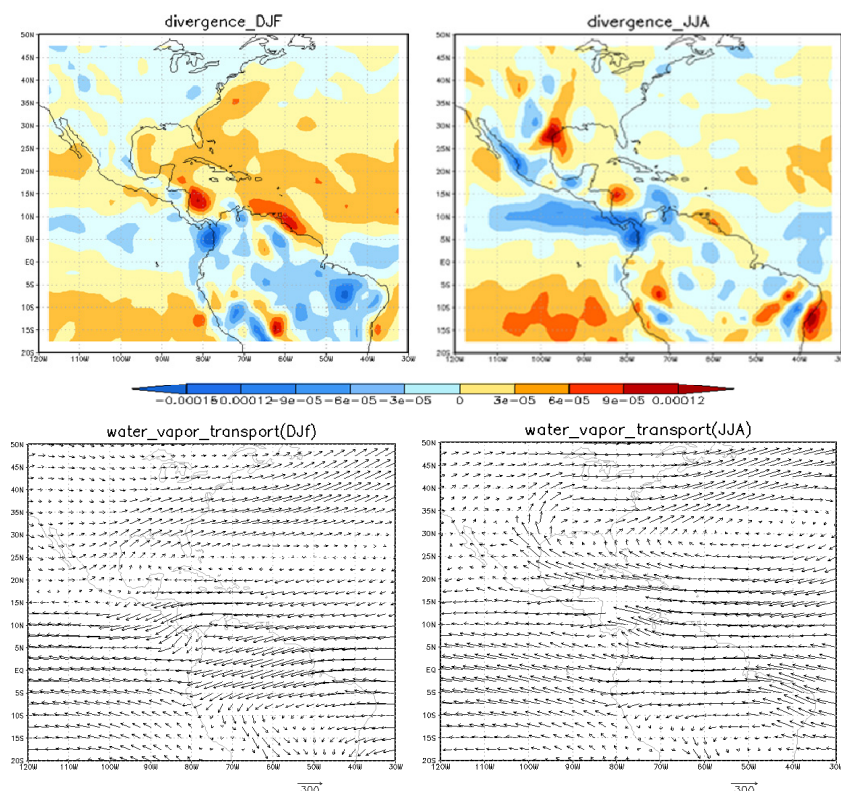


Figure 5.6 Spatial pattern of water vapor divergence and water vapor transport [Ionita *et al.*, 2008] during boreal winter (DJF) and summer (JJA) averaged over the period 1962-2000 .

5.1.1.2 Simulated climatology

To verify the model output and have a better constrain for the simulation of the Holocene climate, we first compare the results from the CTL⁸ experiment with the observation. However, it is necessary to keep in mind that the boundary conditions used in CTL have slight difference with the real present condition, e.g. the greenhouse gas concentration, which in turn can directly or indirectly result in considerable bias from the observed climate.

The simulated surface air temperature and wind are shown in Figure 5.7. Here the surface air temperature over the ocean is identical with the simulated SST (not shown). The simulated easterly winds are consistent with the observed climatology in both magnitude and direction, showing a quasi-constant easterly winds at a maximum 10m/s. The annual surface air temperature in the simulation (Figure 5.7a) is slightly lower than that in the observation (Figure 5.3a), which might reflect the cooling effect due to a lower greenhouse gas concentration in CTL. In most of the Caribbean, the surface air temperature during the winter and spring (Figure 5.7b,c) is below 27°C, generating a relative weak convection. This leads to less rainfall in these seasons (Figure 5.8b,c). As the AWP forms gradually in the summer, the whole Caribbean experiences a temperature above the threshold for convection (Figure 5.7d). Correspondingly, the precipitation also increases dramatically (Figure 5.8d). The high temperature can last through the autumn over the whole region (Figure 5.7e), bringing the late rainfall season for the Caribbean (Figure 5.8e).

In general, the results from the CTL experiment show very good agreement with the observed climatology in the large scale pattern over the Caribbean for the present-day condition.

⁸ CTL: Present-day control experiment (detail in in section 2.2.1.1)

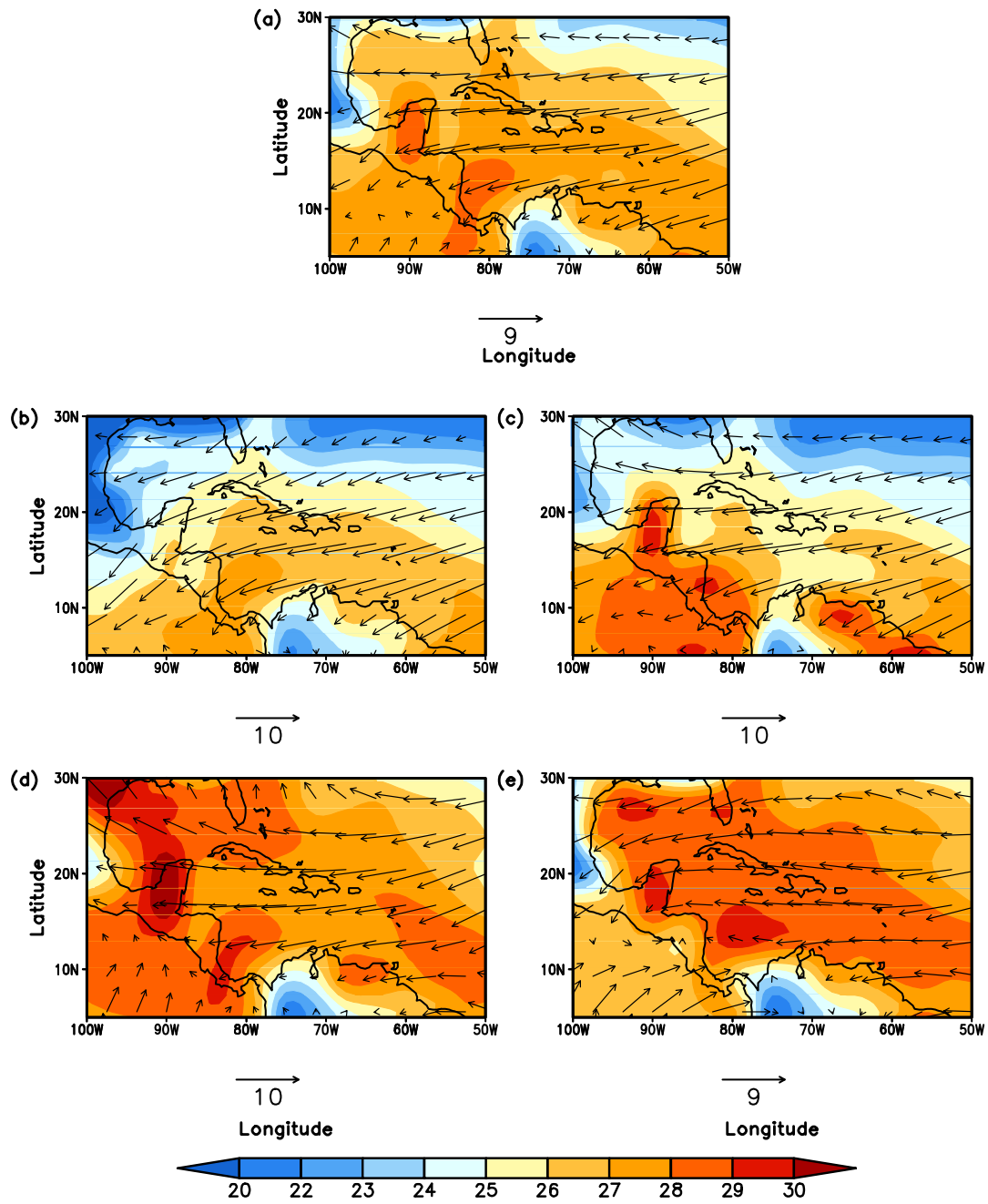


Figure 5.7 Simulated surface air temperature (in °C) and winds (in m/s) in the Caribbean, averaged over 2000 years in CTL for (a) annual, (b) DJF, (c) MAM, (d) JJA and (e) SON.

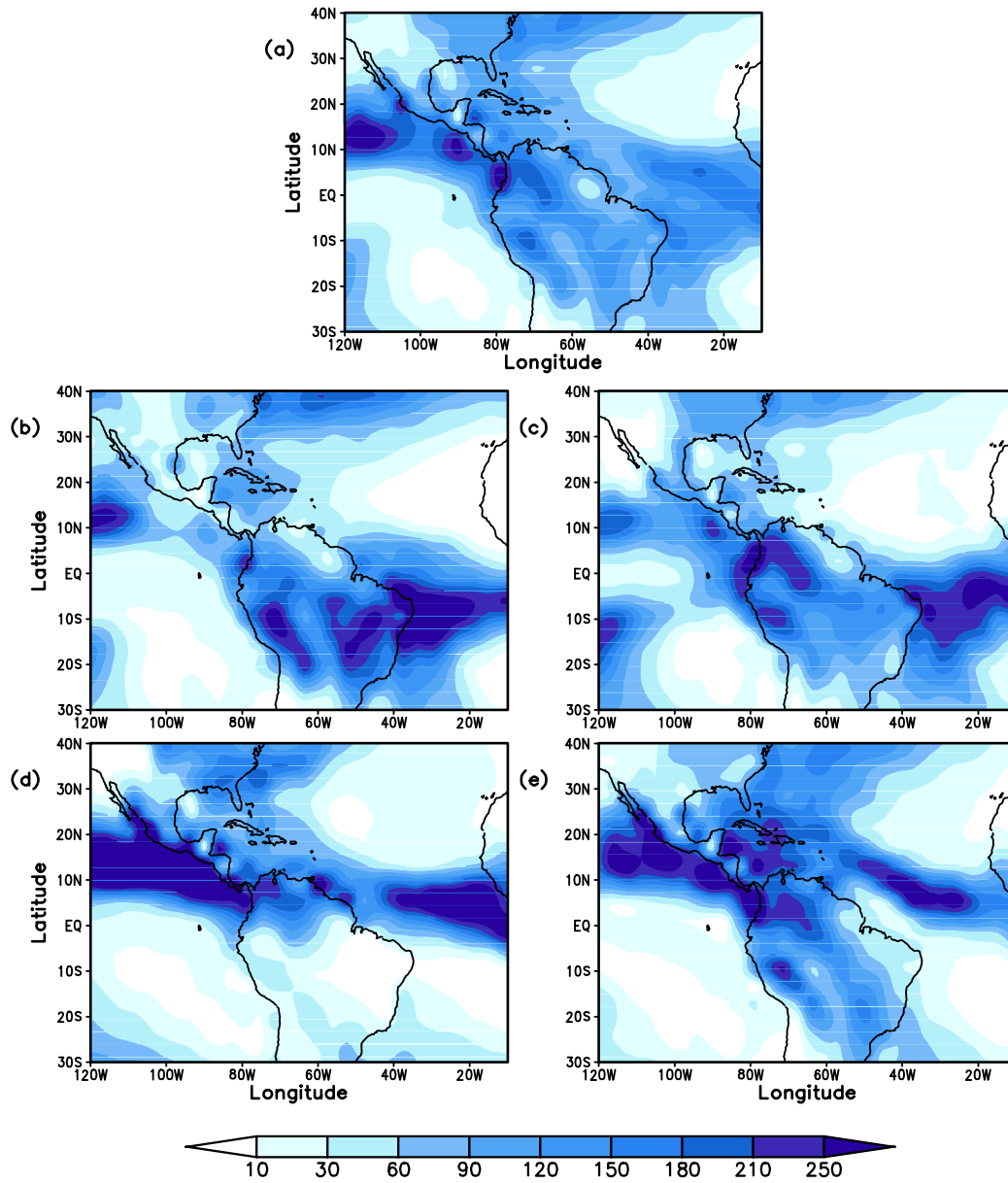


Figure 5.8 Simulated precipitation (mm/month) in the Caribbean, averaged over 2000 years in CTL for (a) annual, (b) DJF, (c) MAM, (d) JJA and (e) SON.

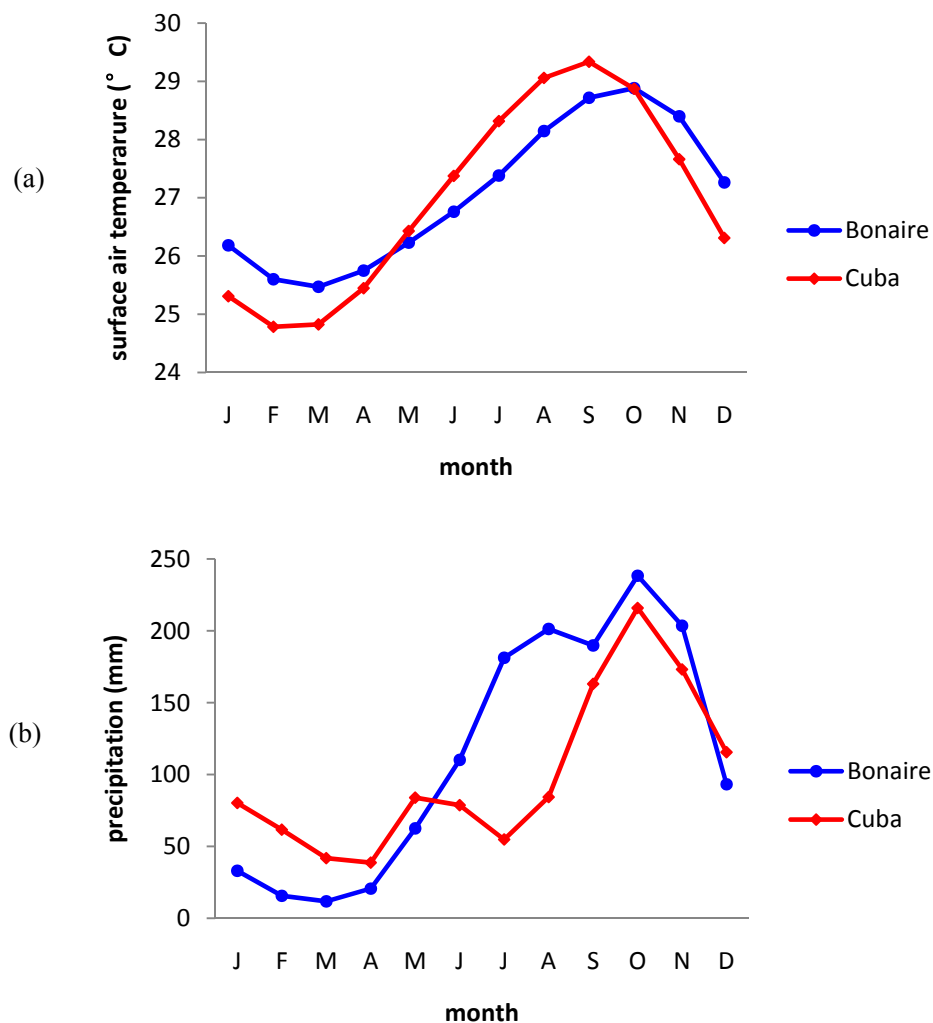


Figure 5.9 Simulated SST (in °C) and precipitation (in mm/month) annual cycle in Cuba (red) and Bonaire (blue) averaged over 2000 years in CTL.

The simulated annual cycles of the surface air temperature for Cuba and Bonaire (Figure 5.9) show a similar trend with that in the observation (Figure 5.5). Notably, the model can simulate the bimodal character of the Caribbean rainfall (Figure 5.9b), but seems to overestimate the Bonaire precipitation (Figure 5.5b). Possible explanations can be either attributed to the different grid setup and the grid used to represent the Bonaire precipitation in the simulation and observation, or due to the coarse resolution of the model, as the Caribbean rainfall exhibits very distinct sub-regional feature. This also has been found in different observation datasets, e.g. CMAP and Hulme-CRU datasets (Figure 5.10).

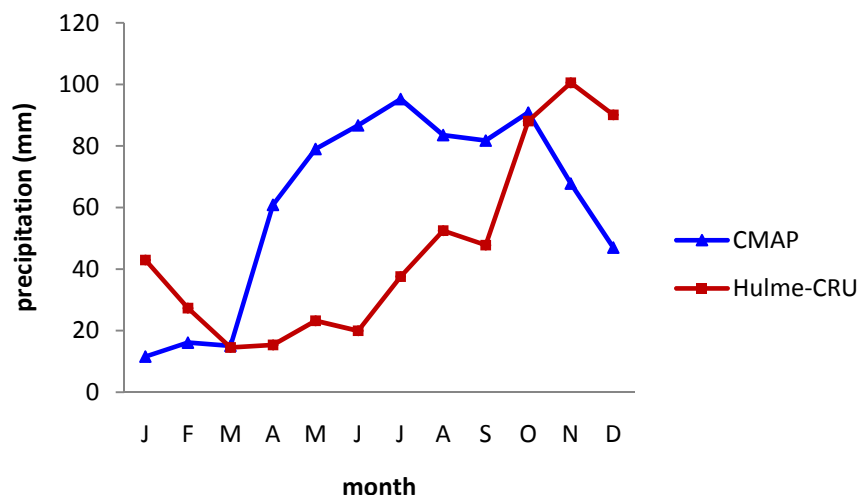


Figure 5.10 Observed precipitation (in mm/month) annual cycle in Bonaire averaged from 1979 to 1998 based on CMAP [Xie and Arkin, 1997] and Hulme-CRU [Hulme *et al.*, 1998] datasets. Here the grids used to represent Bonaire precipitation are centered at 291.25°E, 11.25°N in CMAP dataset and 292.5°E and 12.5°E in Hulme-CRU datasets.

5.1.2 The Caribbean climatology during the mid-Holocene

5.1.2.1 Simulated climatology

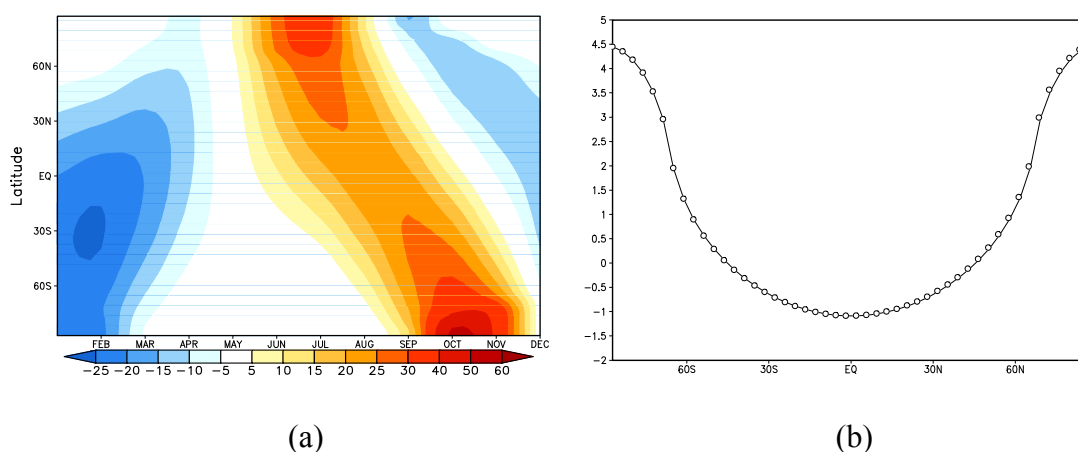


Figure 5.11 (a) monthly zonal averaged top incoming shortwave radiation anomalies (in W/m^2) in H6K⁹ relative to CTL. (b) as (a) but for the annual mean value.

⁹ H6K: mid-Holocene (6 kyr BP) experiment (detail in section 2.2.1.1)

The mid-Holocene climatology anomalies from the present-day condition are mainly due to the orbital change [e.g. *Wanner et al.*, 2008]. The orbital induced insolation change in the tropical and NH sub-tropical shows the maximum positive anomalies from July to September and the maximum negative anomalies from January to March (Figure 5.11a), which is approximately 1-month lag or leading with those in the mid-to-high latitudes. Overall, its annual mean value is negative relative to the present (Figure 5.11b), which can result in a general cooling over the low latitudes during the mid-Holocene, as indicated by most proxy data [e.g. *C. Rühlemann et al.*, 1999; *Lea et al.*, 2003; *Rimbu et al.*, 2004; *Giry*, 2011].

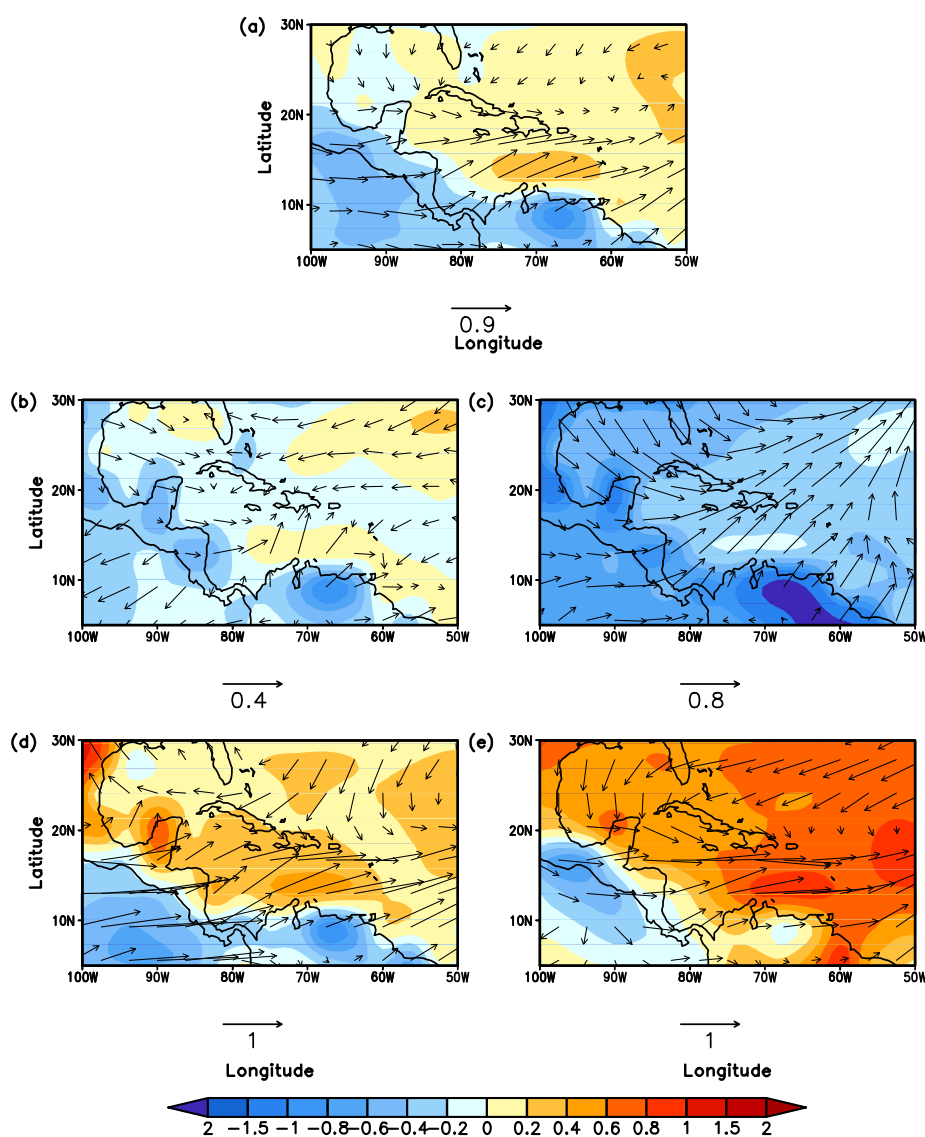


Figure 5.12 Simulated surface air temperature (in $^{\circ}\text{C}$) and 10m wind anomalies (m/s) in H6K relative to CTL in the Caribbean for (a) annual, (b) DJF, (c) MAM, (d) JJA and (e) SON.

The simulated seasonal surface air temperature in H6K (detail in Chapter 2), which is identical with the SST over the ocean, fits the insolation change, with a warming in summer and autumn and a cooling in the other seasons (Figure 5.12b-e). The spatial pattern of seasonal surface air temperature anomalies and their magnitudes are in general consistent with a previous Holocene transient simulation using a similar model setup [*S J Lorenz and Lohmann, 2004*]. Such change in the temperature leads to mid-Holocene seasonality increased by approximately 1°C in the Caribbean, which is more than 20% of the total seasonality. Notably, the annual mean temperature anomalies are positive in the simulation (Figure 5.12a). Although the magnitude is rather small, it shows a different sign as compared to the insolation change (Figure 5.11b) and proxy based temperature reconstruction [Figure 5.1; *C. Rühlemann et al., 1999; Lea et al., 2003; Giry, 2011*]. One possible explanation can be that, in H6K the AMOC is decreased by more than 2 Sv (Figure 4.1), which prevents the relatively warm water to be transported to the cold North Atlantic and thus traps more heat in the low latitudes. This effect can overcompensate the insolation induced cooling. Furthermore, Figure 5.12a shows clear land-sea contrast in the temperature anomalies, with the cooling over the land and the warming over the ocean. While the locations of the proxy mentioned above are very close to the coastline, which indicates they can have more influence from the land than from the ocean. Sensitivity study has also suggested that the temperature change over the Southern Caribbean and Western Tropical Atlantic regions can vary dramatically in small scales with the different physical processes that dominate [*Wan et al., 2009*]. From this point of view, both the modeling and proxy results need to be interpreted more carefully.

The easterly winds show a significant decrease over the Caribbean during the mid-Holocene in all seasons, especially during the summer (Figure 5.12d). Meanwhile, the easterly winds over the subtropical Atlantic regions get intensified except during spring (Figure 5.12). These anomalies tend to result in more convergence in the Caribbean and less water vapor transported to the Western Pacific. This partly explains the remarkable increase of the Caribbean precipitation in H6K (Figure 5.13). Moreover, this increase of the precipitation in this period is also related

to the orbital induced ITCZ shift. Evidences for a more northward position of the ITCZ over the Atlantic during the Holocene have been found in some proxies [Hodell *et al.*, 1995; Haug *et al.*, 2001]. The ITCZ shift can be easily seen from the simulation results, which illustrate a precipitation anomaly contrast between the northern South America and the Caribbean. Such a shift in the ITCZ brings more precipitation to the Caribbean in all seasons (Figure 5.13). The warmer summer SST (Figure 5.12d,e) could provide more energy for this wetter condition by more convection. Moreover, the AMOC in H6K is reduced by more than 2Sv (Figure 3.3). Such a reduction in the AMOC can be partly induced by the freshening from more precipitation [e.g. G. Lohmann, 2003].

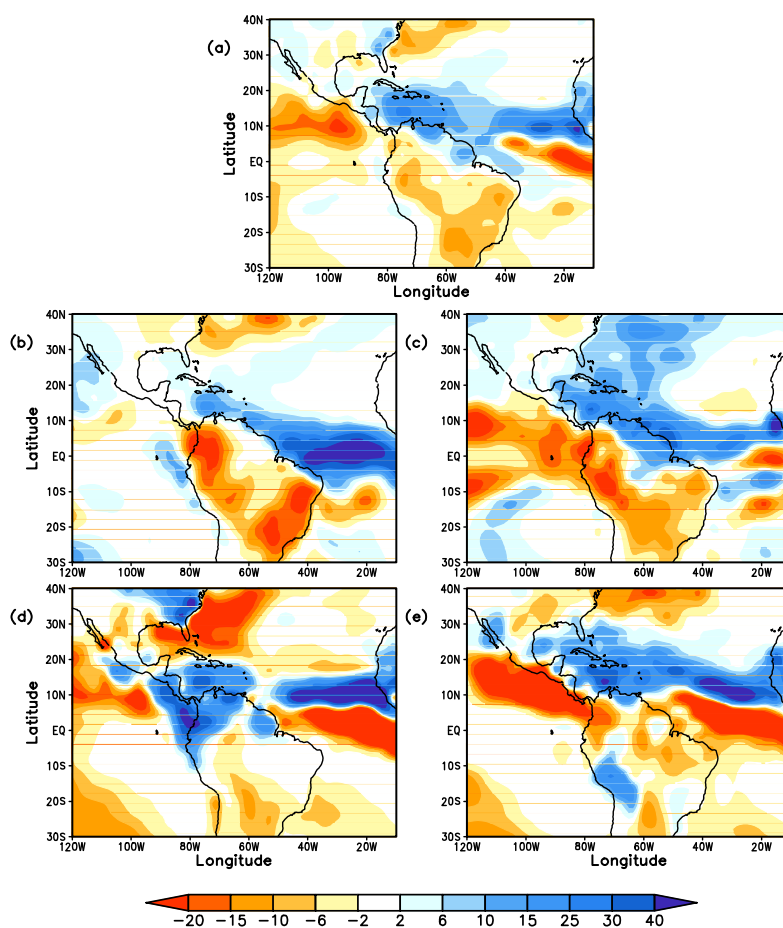


Figure 5.13 Simulated precipitation anomalies (in mm/day) in H6K relative to CTL in the Caribbean for (a) annual, (b) DJF, (c) MAM, (d) JJA and (e) SON.

The simulated $\delta^{18}\text{O}$ of the precipitation shows opposite anomalies with the precipitation (Figure 5.14) in H6K, which results from the amount effect that is the

common relation between precipitation and the associated $\delta^{18}\text{O}$ over the tropical regions and monsoon areas in the observation [Dansgaard, 1964]. Increased precipitation and stronger advection of moisture from the Atlantic due to warmer SST result in more isotopically-depleted rainfall, which is also found in the Eemain simulation using the older version model setup [Herold and Lohmann, 2009]. The annual mean $\delta^{18}\text{O}$ of the precipitation has the depletion in a magnitude of 0.4. However, it also shows distinct seasonal variation. In DJF and MAM, the whole Caribbean region is characterized by strong $\delta^{18}\text{O}$ depletion (Figure 5.14b,c), following the wetter condition in these seasons (Figure 5.13b,c). While in JJA and SON, the anomalies of the $\delta^{18}\text{O}$ reverse (Figure 5.14d,e), although the wetter condition still exists (Figure 5.13d,e).

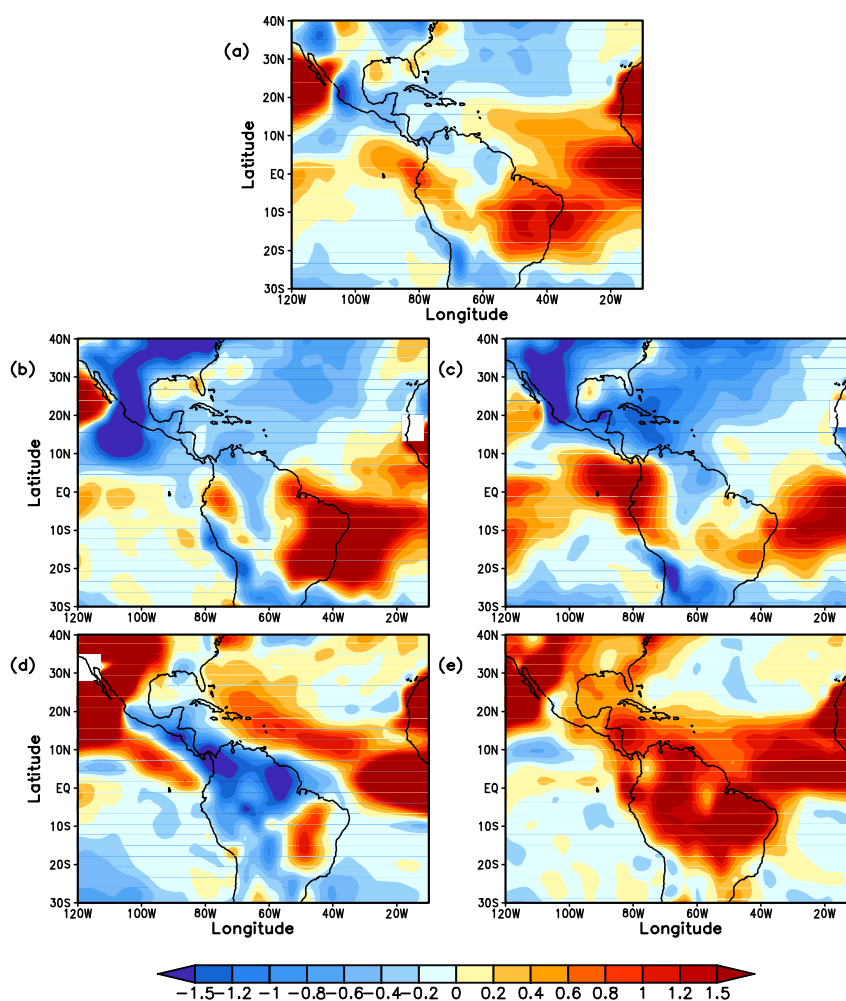


Figure 5.14 Simulated $\delta^{18}\text{O}$ of the total precipitation anomalies (in ‰) in H6K-wiso relative to CTL-wiso in the Caribbean for (a) annual, (b) DJF, (c) MAM, (d) JJA and (e) SON.

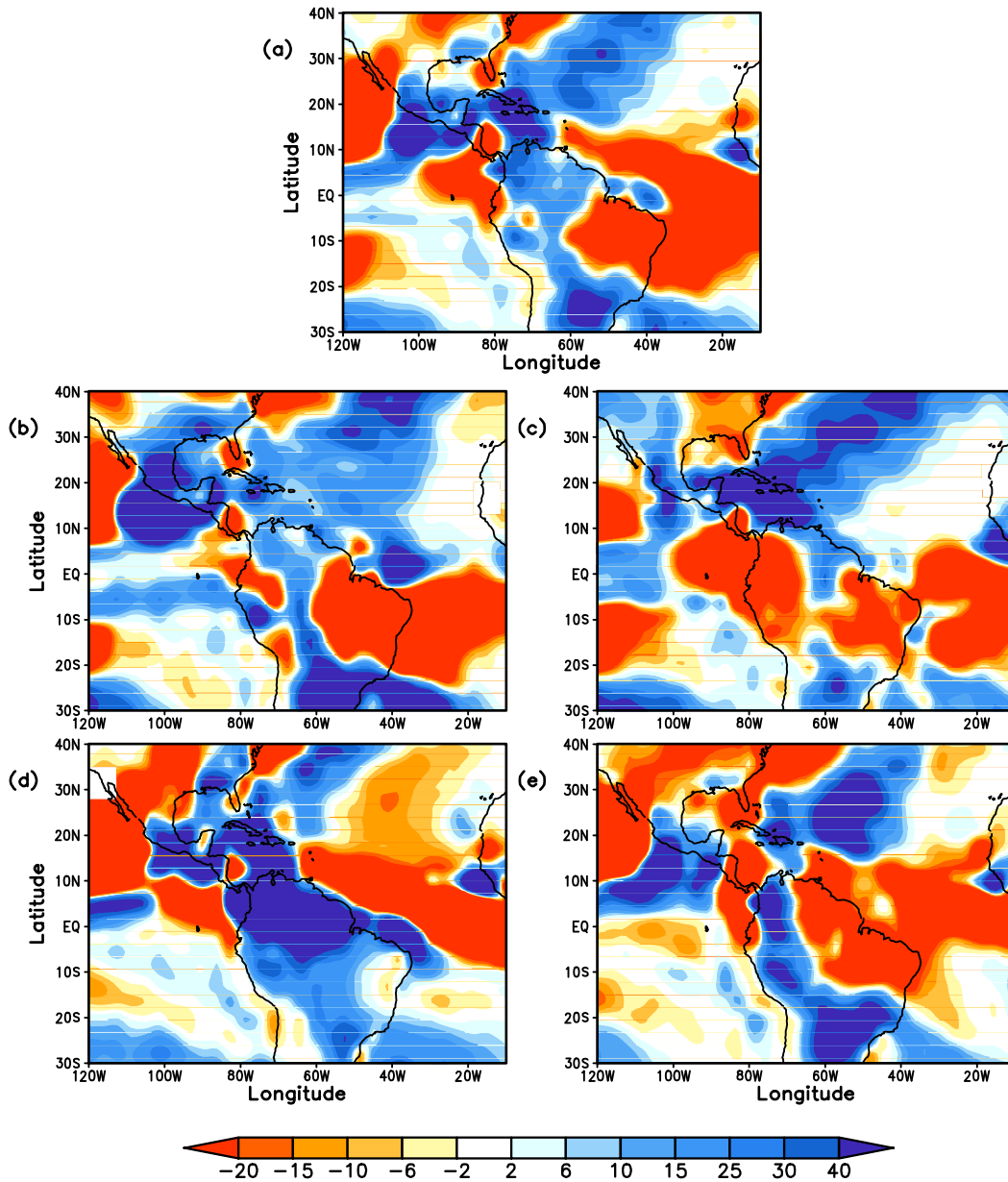


Figure 5.15 Simulated precipitation anomalies (in mm/day) in H6K-wiso relative to CTL-wiso in the Caribbean for (a) annual, (b) DJF, (c) MAM, (d) JJA and (e) SON.

To find the possible explanation, the associated precipitation anomalies in H6K simulated by ECHAM5-wiso are given in Figure 5.15. The spatial pattern of simulated precipitation anomalies in the coupled model and the atmospheric model show some different features, with more similarities in DJF and MAM and quite distinguished regional characters in JJA and SON. Especially, the anomalies in the northern South America are contradicted in two setups. Over the Caribbean, the precipitation from ECHAM5-wiso also shows fewer areas with positive anomalies

than those from the coupled model. This disagreement in the regional scale between a coupled model and its atmospheric part might be a common feature in the coupled general circulation models. Results from the PMIP also demonstrate the simulated precipitation climatology between the coupled model and its atmospheric part using fixed SST has pronounced difference in our study area [Braconnot *et al.*, 2007]. Notably, ECHAM5-wiso simulates more significant precipitation anomalies between the mid-Holocene and present, compared with it does in the coupled model. It might be either induced by the relatively short integration time of the experiment that we perform using ECHAM5-wiso or by a large difference between the mid-Holocene and present-day SST prescribed as the ocean boundary condition.

5.1.2.2 Model-data comparison

Although it is difficult to compare the annual temperature in the simulation and coral based SST reconstruction as discussed in 5.1.2.1. The monthly-resolved records of Sr/Ca from the fossil corals (a proxy for SST) in Bonaire provide us possibility to access the seasonality change during the mid-Holocene.

The three modern coral Sr/Ca records (Figure 5.16a) suggest a mean SST seasonality of $2.8 \pm 0.3^\circ\text{C}$ [Giry *et al.*, 2011], based on the monthly Sr/Ca-SST relationship of -0.041 mmol/mol per $^\circ\text{C}$ [Steffen Hertzinger *et al.*, 2006]. In a 6.2 kyr BP coral, the reconstructed SST seasonality increases to $3.5 \pm 1.0^\circ\text{C}$ (Figure 5.16a). Although the error for the 6.2 kyr BP coral is relatively large, making it difficult to reach a conclusion whether the seasonality is increased during the mid-Holocene or not from the coral-based results, the model based Bonaire SST annual cycle shows more than 1°C seasonality increase in H6K (Figure 5.16b). This pronounced increase in the SST seasonality is a large scale feature over the tropical and subtropical North Atlantic in the simulation (Figure 5.16c), which can be attributed to the direct insolation change as explained in 5.1.2.1. Similar results have been found from a last interglacial coral record from the Caribbean [Winter *et al.*, 2003].

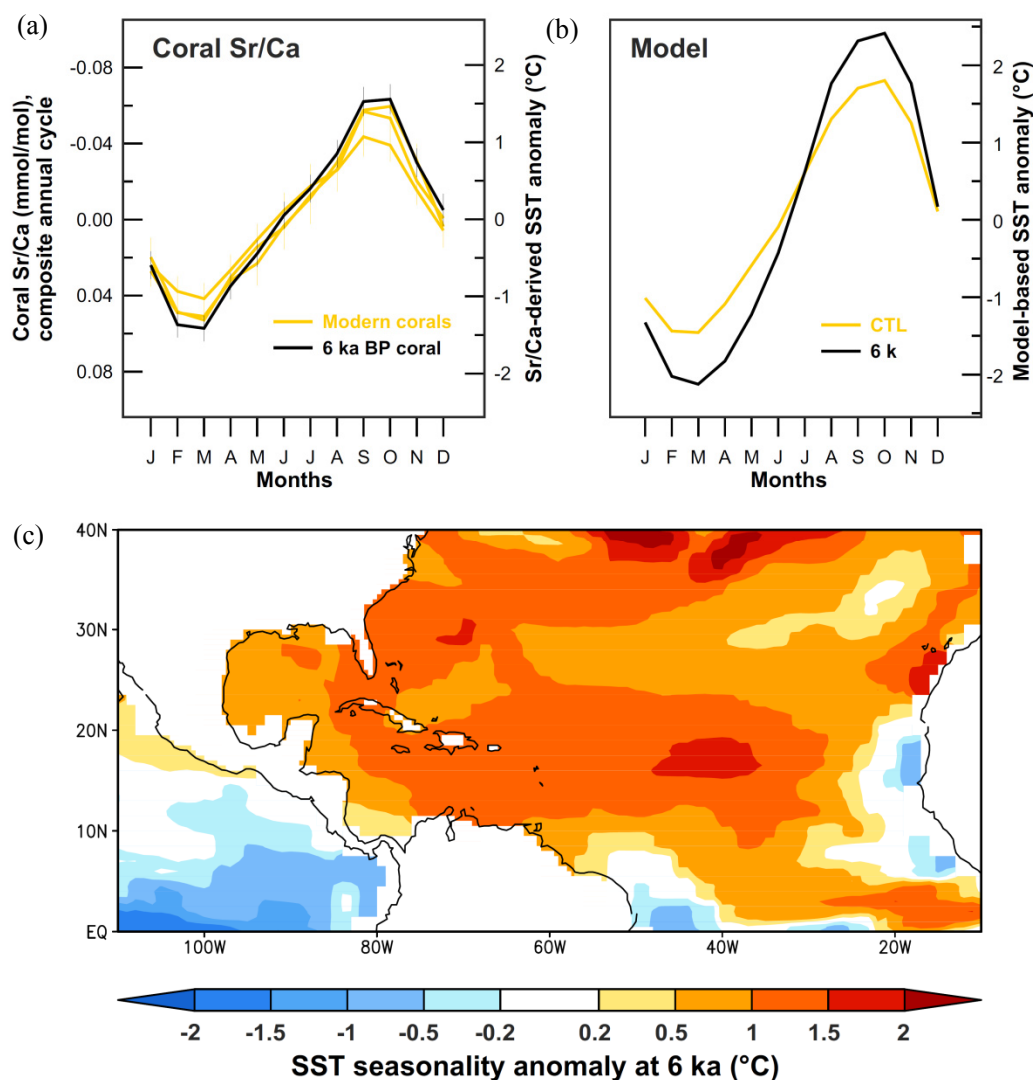


Figure 5.16 Comparison of Bonaire sea surface temperature (SST) annual cycles inferred from (a) coral Sr/Ca records and (b) the simulation. (c) SST seasonality anomaly in H6K relative to CTL. Figure from Giry [2011].

5.1.3 The Caribbean climatology during the early Holocene

5.1.3.1 Simulated climatology

As has been introduced in Chapter 1, the early Holocene (refer to 9 kyr BP in this study) are mainly controlled by orbital induced insolation change and the influence from the LIS.

The insolation change in 9 kyr BP is similar with that in 6 kyr BP, except that the magnitude is even larger (Figure 5.17). Therefore, its influence on the climate should resemble that in 6 kyr BP regarding the spatial pattern. In the Caribbean, the seasonal temperature variation (Figure 5.18) shows a similar feature with that in H6K. Due to even less insolation during DJF and MAM in H9KO¹⁰, a strong cooling dominates the whole Caribbean compared with that in CTL and H6K (Figure 5.18b,c). It can overcompensate the warming during JJA and SON in this period (Figure 5.18d,e), leading to a general cooling in the annual mean field, except over small areas in the southern Caribbean (Figure 5.18a). The AMOC is further reduced in H9KO compared with it in H6K (Figure 3.3). However, the heat trapped by the weakened overturning still cannot overcome the strong cooling. Additionally, the reduced greenhouse gas concentration in 9 kyr relative to the present-day and 6 kyr BP can also contribute to the cooling effect (Table 2.2). The easterly winds are even weaker than that in H6K (Figure 5.18), which can further prevent the water vapor transported from the Caribbean to the western Pacific, thus resulting in even larger rainfall contrast on tropical western Pacific and the Caribbean bounded by the central America (Figure 5.19).

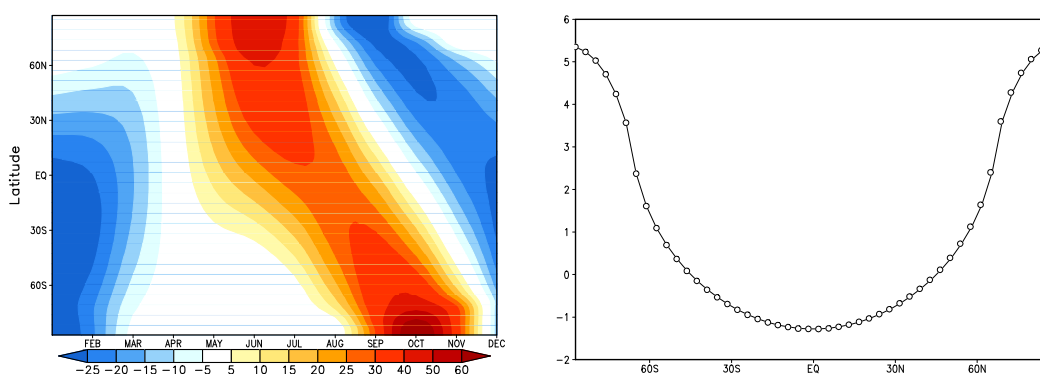


Figure 5.17 (a) monthly zonal averaged top incoming shortwave radiation anomalies (in W/m^2) in 9 kyr BP experiments relative to CTL. (b) as (a) but for the annual mean value.

¹⁰ H9KO: early Holocene (9 kyr BP) experiment with prescribed orbital forcing and greenhouse gases (detail in section 2.2.1.1)

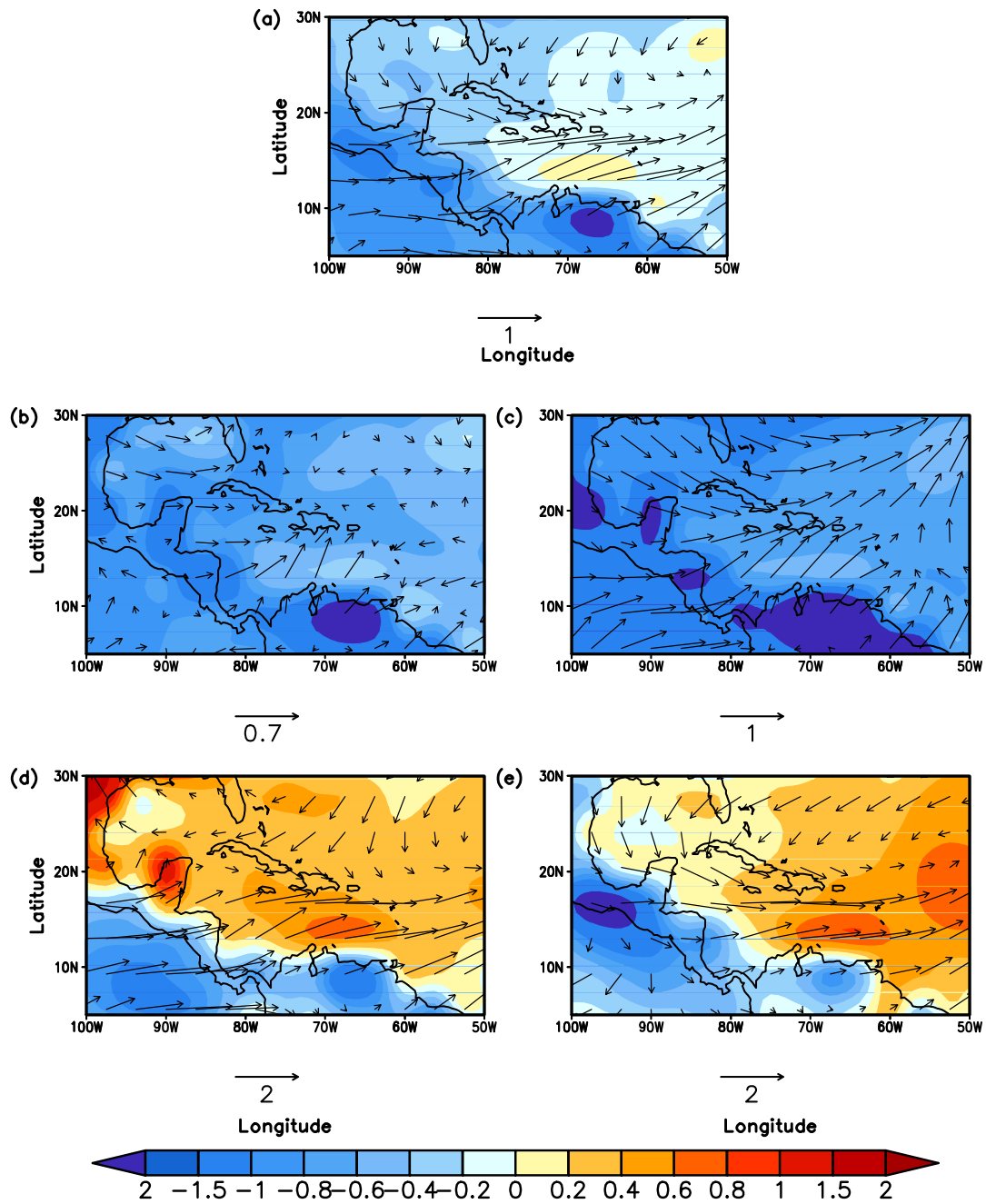


Figure 5.18 Surface air temperature (in °C) and 10m wind anomalies (m/s) in H9KO relative to CTL in the Caribbean for (a) annual, (b) DJF, (c) MAM, (d) JJA and (e) SON.

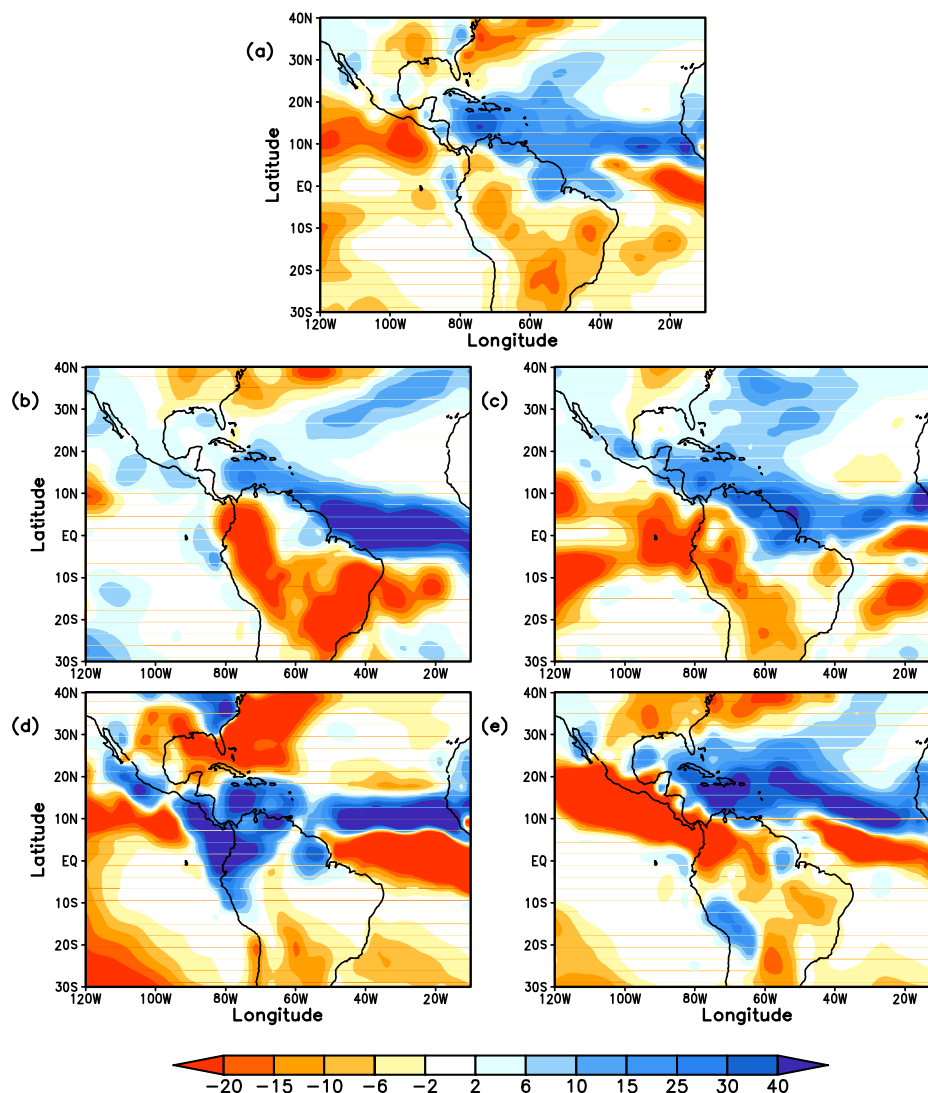


Figure 5.19 Precipitation anomalies (in mm/day) in H9KO relative to CTL in the Caribbean for (a) annual, (b) DJF, (c) MAM, (d) JJA and (e) SON.

Existing of the LIS leads to dramatic cooling effect on the local climate (Figure 3.1), which might have some influence on the climate in our study area as well by teleconnection via atmospheric and ocean circulation. Interestingly, in H9KT¹¹, the simulated surface air temperature over the Caribbean shows opposite anomalies with the cooling over the northern North America and the adjacent areas of the North Atlantic, directly induced by the high albedo over the ice sheet and the cold leeward air. Up to 0.5°C warming can be observed in the annual mean anomalies field over the

¹¹ H9KT: early Holocene (9 kyr BP) experiment with boundary forcing identical to H9KO but prescribed LIS (detail in section 2.2.1.1)

Caribbean (Figure 5.20). Compared to the general cooling induced by the orbital change, the magnitude of the warming is very significant. Concerning the control mechanism, the AMOC change can play the major role. The Caribbean region acts as the important route for the warm water from the tropical Atlantic Ocean transported northward to the high latitudes by the currents. Figure 3.3 shows that the AMOC is strengthened significantly in H9KT relative to CTL and H9KO, due to the cooling and associated more deepwater formation in the North Atlantic. Thus, the vigorous AMOC can bring more warm water via the Caribbean regions into the North Atlantic. In this process, the Caribbean can also experience a warming, especially in the South Caribbean (Figure 5.20), where the Caribbean Current flows by.

Change in the wind field in H9KT resembles that in H9KO, indicating a weakening of the easterly winds (Figure 5.20). The precipitation anomalies also have the similar spatial pattern with that in H9KO, which suggests the influence of the LIS itself on hydrology cycle in the study area is minor (Figure 5.21).

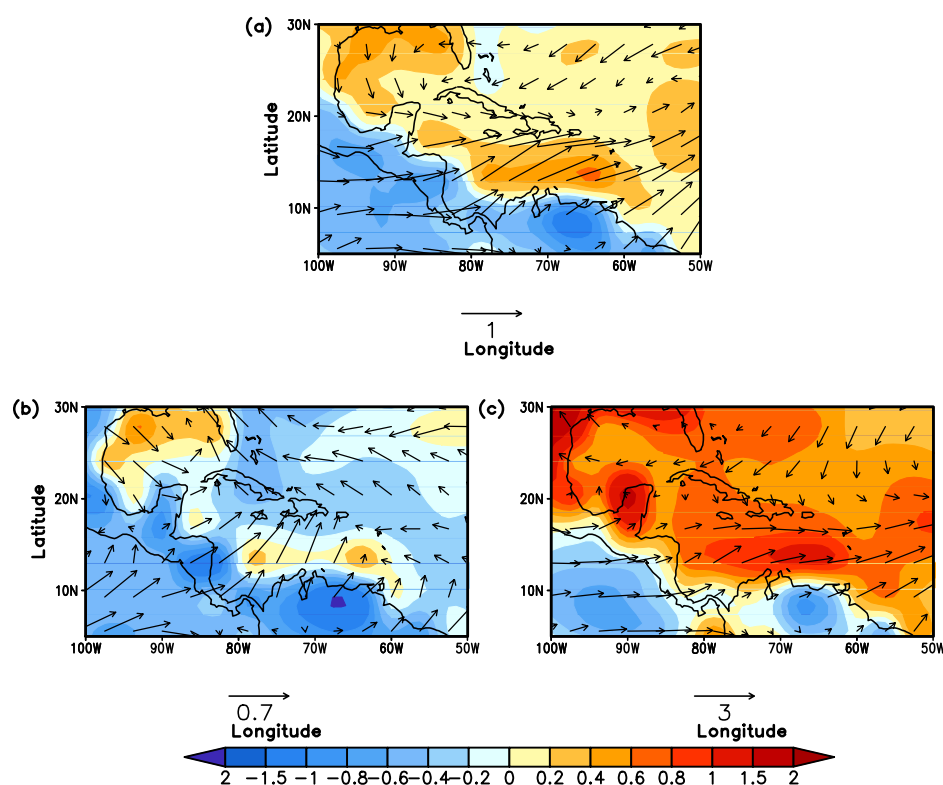


Figure 5.20 Surface air temperature (in $^{\circ}\text{C}$) and 10m wind anomalies (m/s) in H9KT relative to CTL in the Caribbean for (a) annual, (b) DJF and (c) JJA.

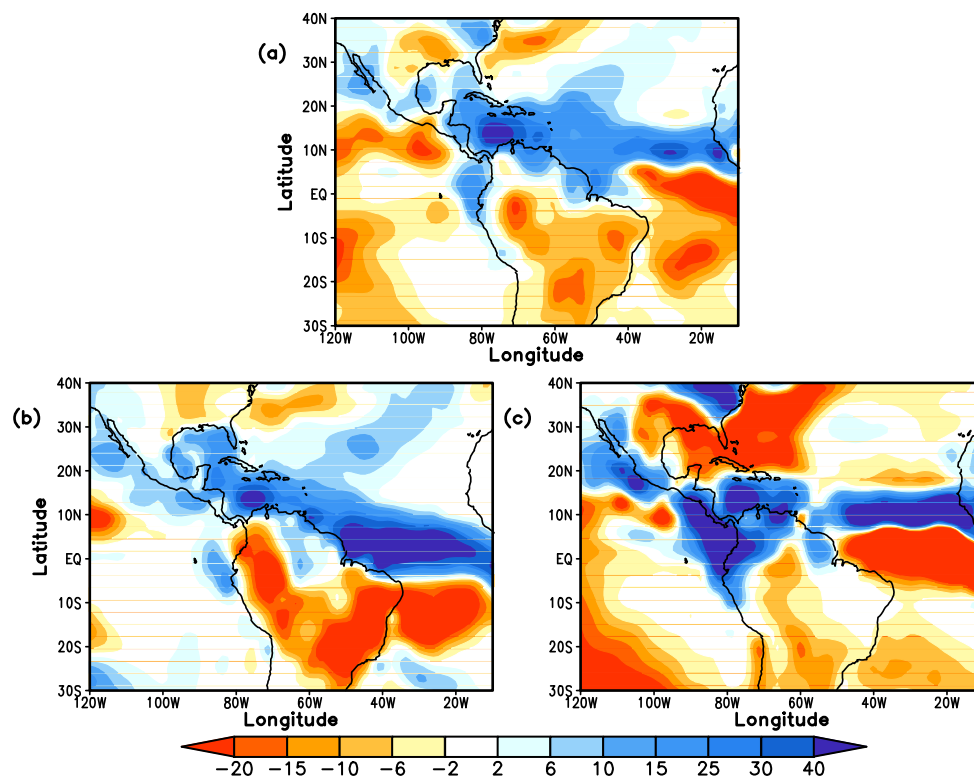


Figure 5.21 Precipitation anomalies (in mm/day) in H9KT relative to CTL in the Caribbean for (a) annual, (b) DJF and (c) JJA.

In H9KM¹², the freshwater flux from the LIS melting enables us to further investigate the LIS influence on the Caribbean climate. The simulated surface air temperature anomalies (Figure 5.22) are in the range between those from H9KO and H9KT, suggesting that melting of the LIS can partly compensate the warming effect of the vigorous AMOC.

Strength of the AMOC in H9KM (Figure 3.3) is reduced by up to 6 Sv relative to CTL. As mentioned in 5.1.2.1, decrease in the AMOC can reduce the heat transfer from the low latitudes to the high latitudes, thus resulting in the low latitudes warming. Over the Caribbean, due to its special location, it seems that both a vigorous and a weakening of the AMOC can generate a warming in this region. However, the mechanisms are different and can lead to compensation with each other, as shown from H9KM.

¹² H9KM: early Holocene (9 kyr BP) experiment with boundary forcing identical to H9KT except prescribed LIS melting (detail in section 2.2.1.1)

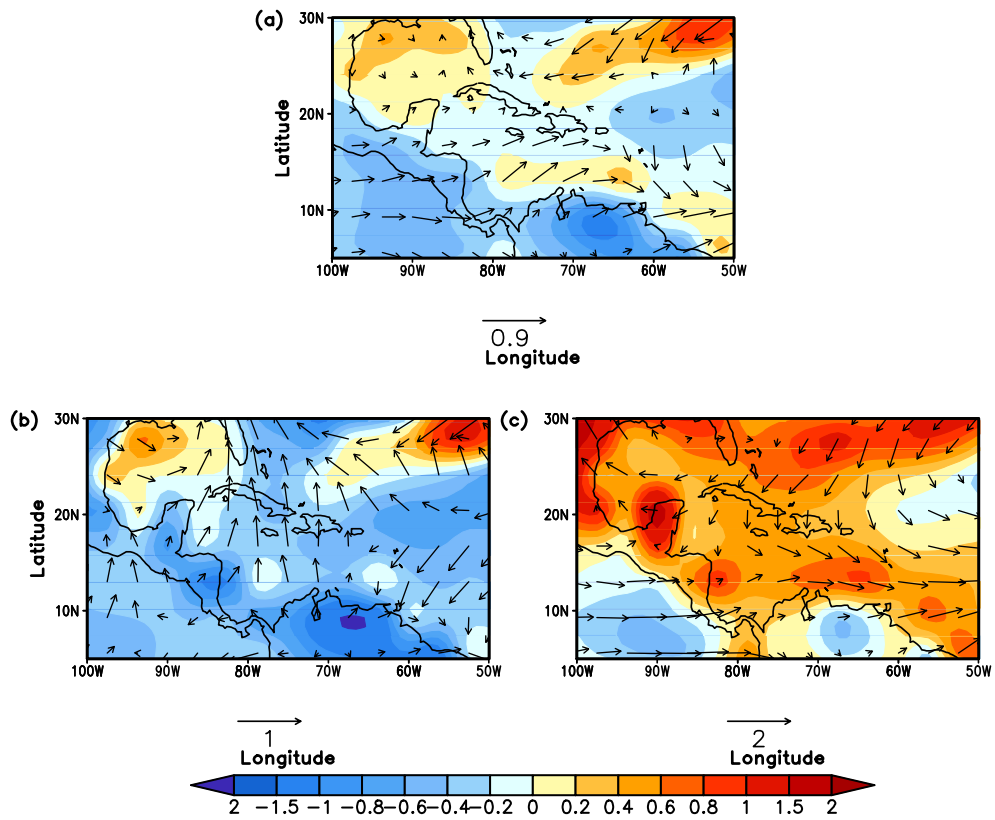


Figure 5.22 As Figure 5.20 but for H9KM.

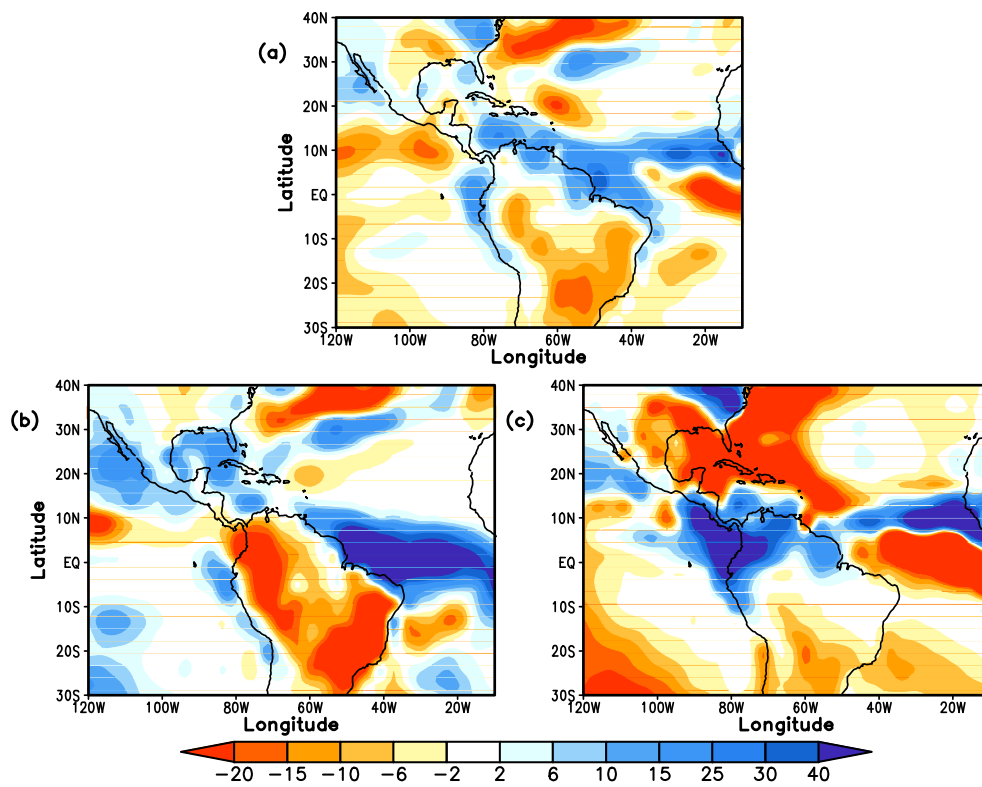


Figure 5.23 As Figure 5.21 but for H9KM.

Along with the ocean circulation change in H9KM, the atmosphere also demonstrates notable difference with CTL and the other 9 kyr BP experiments. The wind anomalies in DJF are in a northward direction instead of eastward. While in JJA, the wind anomalies exhibit a cyclone-like pattern, which can bring more water vapor out of the Caribbean and consequently reduce the rainfall (Figure 5.23c). The precipitation anomalies in H9KM (Figure 5.23) are smaller in the magnitude than that in H9KO and H9KT, making the wetter condition in H9KM less pronounced than it in the other 9 kyr BP experiments.

5.1.3.2 Model-data comparison

The fossil corals analyzed in this study can only date back to the mid-Holocene. Therefore, model-coral data comparison cannot be applied to the early Holocene. In our CaribClim project, the stable isotopes in the Cuban stalagmites, which can date back to around 12 kyr BP and thus cover the whole Holocene transition, are measured by colleagues from University of Heidelberg. The $\delta^{18}\text{O}$ values recorded by the stalagmite in the low latitudes are mainly a proxy for the hydrologic cycle, supplying us the opportunity to compare with the simulated hydrologic change during the Holocene.

The most visible feature in the $\delta^{18}\text{O}$ signal from stalagmite CP and CM is that it shows a very clear transition from higher $\delta^{18}\text{O}$ values in the early Holocene to lower ones in the mid-Holocene, leading to almost 2‰ difference between two phases (Figure 5.24). The large $\delta^{18}\text{O}$ shift can be caused either by remarkable change in the precipitation amount or possible change in $\delta^{18}\text{O}$ from the source of the precipitation. In all the 6 kyr and 9 kyr BP experiments, the simulated precipitation has a large increase in the Caribbean. However, the precipitation anomalies between the different 9 kyr BP experiments and H6K are much smaller than those relative to CTL. These anomalies can only explain 0.2 per mill difference between H9KM and H6K (Figure 5.25) by the precipitation amount change due to the orbital forcing.

Fensterer [2011] compares these stalagmite $\delta^{18}\text{O}$ records with other proxy records (Figure 5.24) from the circum Caribbean region and finds that similar trend is also

recorded in lake and marine sediment proxies. Notably, the planktic foraminifera $\delta^{18}\text{O}$ curve from a sediment core close to Haiti [Horn, 2010] indicates a same magnitude anomaly of the $\delta^{18}\text{O}$ values between early and mid-Holocene (Figure 5.24 red). It implies that the precipitation $\delta^{18}\text{O}$ shift in the stalagmite CP and CM is potential link to the surface ocean $\delta^{18}\text{O}$ change in the same period, considering that the precipitation in Cuba mainly comes from the convection of the sea water nearby.

To examine its possibility in the simulation, results from the sensitivity experiment described in detail in section 2.2.2 are given in Figure 5.26. 2 per mill prescribed sea surface $\delta^{18}\text{O}$ positive anomalies in H9KMS-wiso¹³ can generate more than 1.5 per mill $\delta^{18}\text{O}$ increase in the precipitation. In the early Holocene, the existing of the LIS preserves a large amount of freshwater as ice sheet. Thus, the $\delta^{18}\text{O}$ value in the sea water in this period is comparably higher than that afterward when the LIS melts, which has been indicated in the proxies mentioned above as well as former research [Fairbanks, 1989]. Therefore, it can be concluded that the early to mid-Holocene transition of the $\delta^{18}\text{O}$ observed in the stalagmite CP and CM is induced by a combination of the amount effect due to the insolation change and the source effect due to the sea water $\delta^{18}\text{O}$ change by existing of the LIS.

¹³ H9KMS-wiso: sensitivity experiment performed by ECHAM5-wiso, using H9KM experiment output as boundary conditions except that 2 per mill $\delta^{18}\text{O}$ is added to the surface ocean $\delta^{18}\text{O}$ within the area of 5°-30°N and 30°-90°W (detail in section 2.2.2).

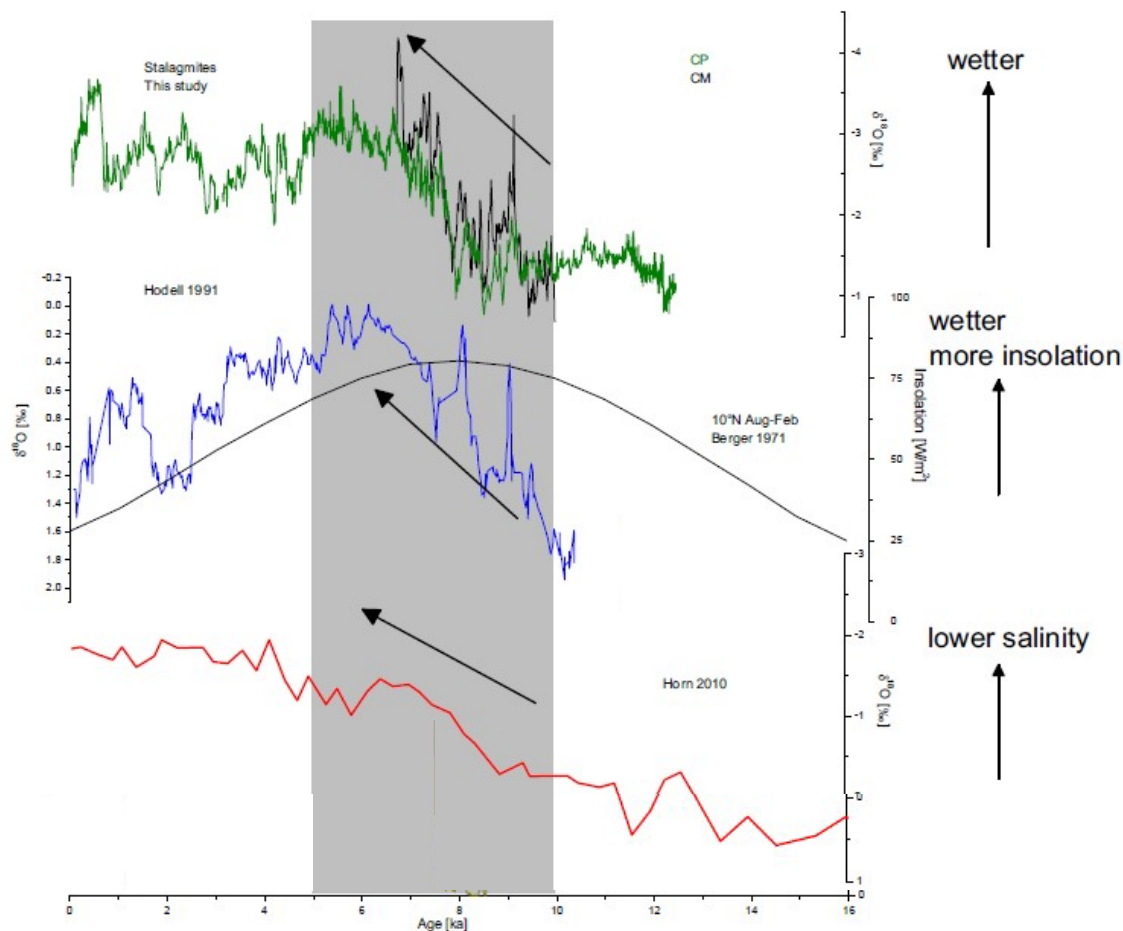


Figure 5.24 The early to mid-Holocene $\delta^{18}\text{O}$ shift indicated by the stalagmite record (top panel). For comparison, $\delta^{18}\text{O}$ from a lake sediment in Haiti [blue curve; *Hodell et al.*, 1991], foraminifera $\delta^{18}\text{O}$ from marine sediment close to Haiti [red curve; *Horn*, 2010] and August-February insolation at 10°N [*Berger*, 1978] are also shown.

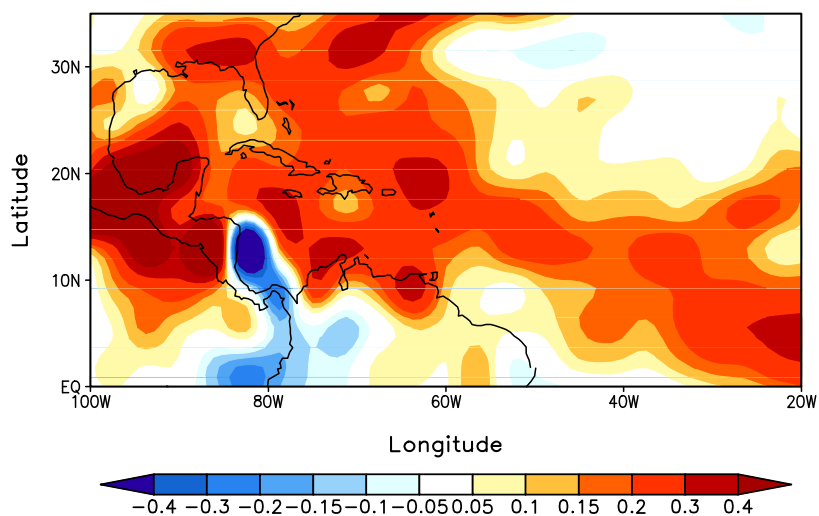


Figure 5.25 Simulated precipitation $\delta^{18}\text{O}$ anomalies (in ‰) in H9KM-wiso relative to H6K-wiso.

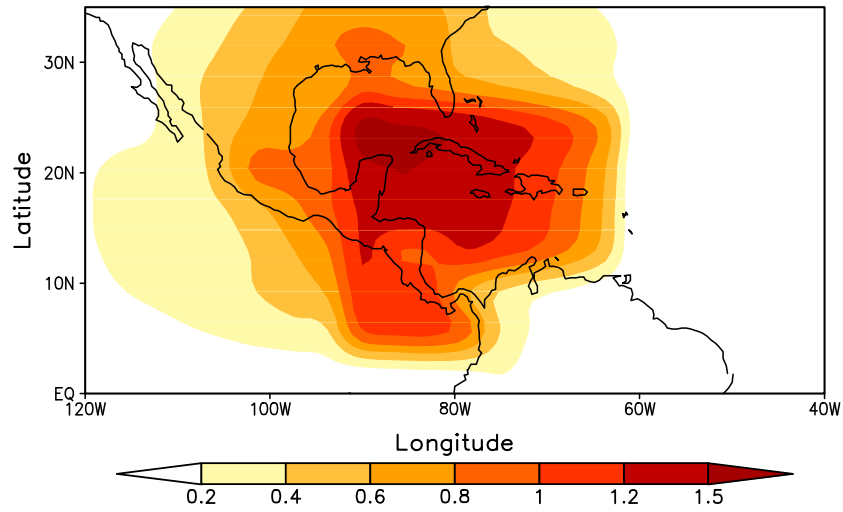


Figure 5.26 Simulated precipitation $\delta^{18}\text{O}$ anomalies (in ‰) in H9KMS-wiso relative to H9KM-wiso.

5.2 The Caribbean climate variability during the Holocene

The long-term Caribbean climate evolution during the Holocene has been attributed more to the external induced variability, e.g. insolation change due to orbital forcing and influence from the existing of the LIS and its melting in the early Holocene. On a short timescale, from seasonal and interannual to decadal and centennial, this variability under the present condition is thought to be controlled more by the internal variability, such as ENSO [e.g. *Giannini et al.*, 2000; *Giannini et al.*, 2001; *Martis et al.*, 2002; *Jury et al.*, 2007], NAO [e.g. *Jury et al.*, 2007], tropical Atlantic variation (TAV) [e.g. *Taylor et al.*, 2002], AMO [e.g. *Sutton and Hodson*, 2005; *Knight et al.*, 2006] and the variation associated with the ocean circulation (Figure 2.3).

Compared with the substantial studies on the present Caribbean climate variability, research on its change during the Holocene is much less. Lachniet et al. [2004] report that ENSO variation has forced Central America monsoon by studying a 1.5-kyr stalagmite in the late Holocene, indicating a drier condition there during the warm phase of ENSO. Similar result has been found by Donnelly and Woodruff [2007] that less hurricane activities in the western Northern Atlantic basin occur during the warm phase of ENSO in the past 5 kyr. An enhanced seasonality has been connected to enhanced positive phase of NAO indicated by a stalagmite record from Barbados during the mid- to late Holocene [*Mangini et al.*, 2007]. Moreover, Rimbu et al. [2003] suggest that persistent warming over the western subtropical Atlantic from the early to late Holocene obtained from alkenone-derived SST is caused by a continuous weakening of a North Hemisphere atmospheric circulation pattern similar to NAO. Such a weakening of the NAO during the Holocene is further elaborated by a modeling study [*G. Lohmann et al.*, 2005] and proved to result from the insolation change. Decadal and multidecadal variability is also observed in a 8-century Mg/Ca SST record measured on foraminifer from a Cariaco Basin sediment [*Black et al.*, 2007]. However, considering the coarse spatial coverage of the proxies, the overall feature of the Caribbean climate variability cannot be well captured.

In this section, we try to explain the Holocene climate variability controlling the Caribbean on different timescales using modeling approach. Comparison between the simulation and observation results will provide us more information about the physical mechanisms involved in each phenomenon, which will be helpful for a better understanding of the proxies.

5.2.1 Seasonal and interannual variability

5.2.1.1 El Niño-Southern Oscillation (ENSO) controlled variability

ENSO is the largest single source of global interannual climate variability [Chiang, 2009]. It is also the dominant factor controlling the variability over the tropical America on seasonal and interannual timescales [Vuille *et al.*, 2003a]. Figure 5.27 depicts the correlations between the Nino3 index and SST for all the seasons based on the observation data.

During the pre-mature phase of a warm ENSO (June-August (0)), the SST manifests positive anomalies over the tropical Pacific Ocean (Figure 5.27a). In this season, a zonal seesaw pattern in the SLP (Figure 5.28a) exists between the Pacific and Atlantic, with high pressure anomalies dominating the Caribbean region, which favors less precipitation (Figure 5.29a) due to a direct atmospheric influence. With the easterly winds weakened [Giannini *et al.*, 2010], this warm anomalies gradually propagate eastward (Figure 5.27b) and can reach the Caribbean during the mature phase (December (0)-February (+1); Figure 5.27c). Meanwhile, the low SLP anomalies also spread into the Caribbean region, especially over the north (Figure 5.28b,c), bringing more precipitation to the northern Caribbean (Figure 5.29c). However, the southern Caribbean is not affected, negative correlation between the warm ENSO and precipitation persists (Figure 5.29c). Therefore, the Caribbean region is characterized by a dipole pattern in the precipitation anomalies. After the warm ENSO, its influence can stay over the Caribbean for another season (March-May (+1)), during which the

warmer SST spreads over the whole Caribbean region and also extends southward to the tropical Atlantic Ocean (Figure 5.27d). Precipitation in most parts of the Caribbean increase slightly (Figure 5.29d).

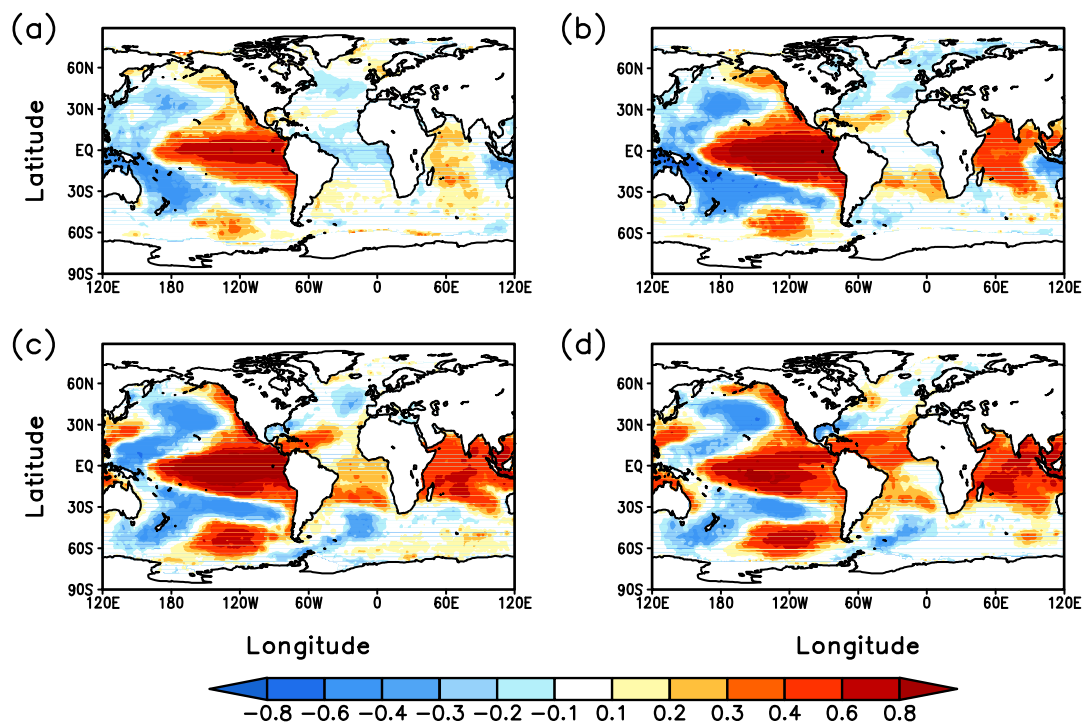


Figure 5.27 Correlation maps of Nino3 index with HadISST [Rayner *et al.*, 2006] during 1900-1998 for (a) June-August (0), (b) September-November (0), (c) December (0)-February (+1) and (d) March-May (+1). Here, Nino3 index is defined as the December (0)-February (+1) mean HadISST SST anomalies over the area 150° - 90° W, -5° - 5° N. Significance greater than 90% is plotted.

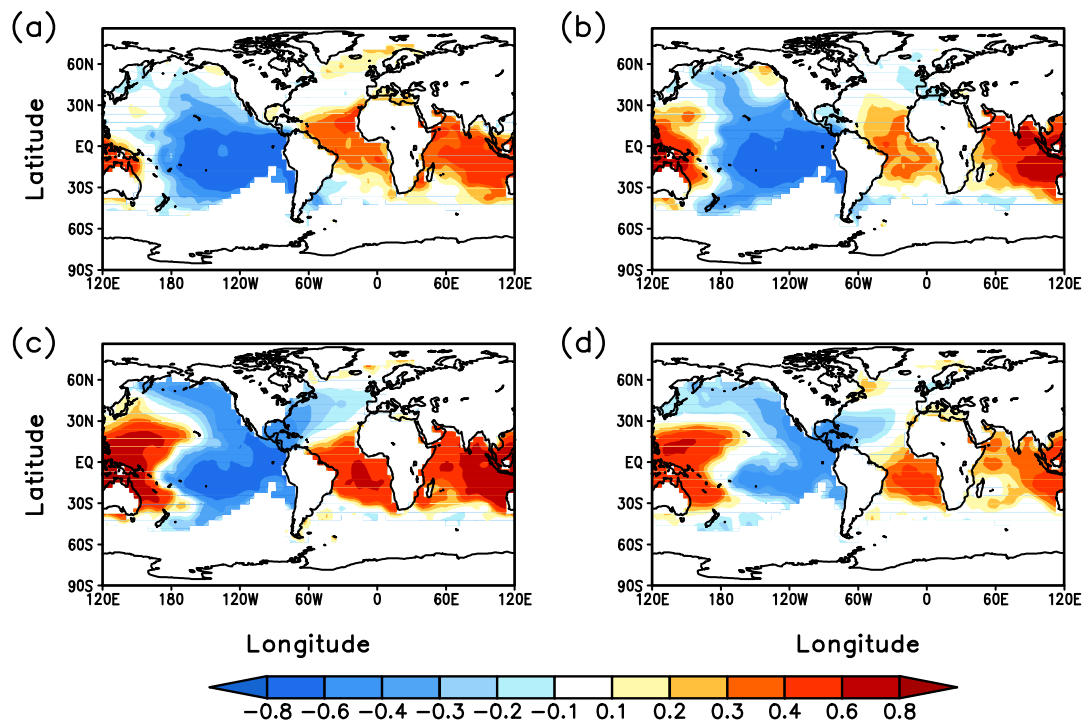


Figure 5.28 As Figure 5.27 but for the correlation maps of Nino3 index with Kaplan SLP [Kaplan *et al.*, 2000] during 1900-1998.

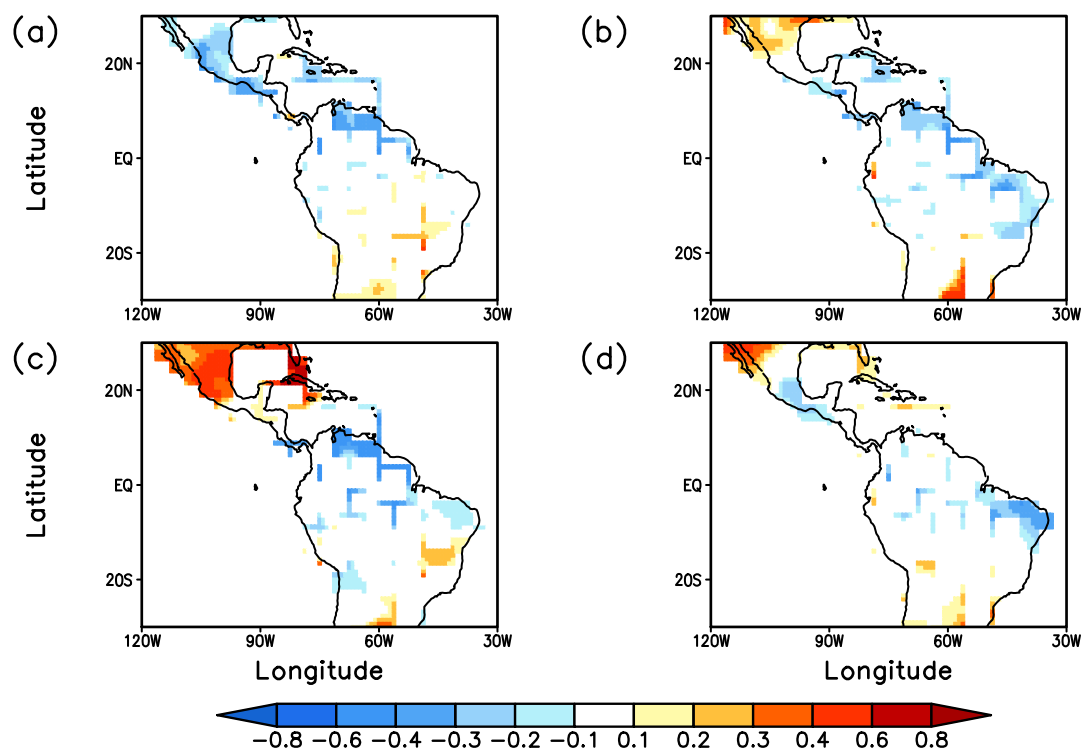


Figure 5.29 As Figure 5.27 but for the correlation maps of Nino3 index with Hulme-CRU [Hulme *et al.*, 1998] precipitation during 1900-1992.

The ENSO signature in CTL, which is demonstrated by correlation between the Nino3 and SST (Figure 5.30), in general, resembles that in the observation for all the seasons (Figure 5.27). The Caribbean SST experiences a warming in phase with a mature warm ENSO (Figure 5.30c,d). However, the model captures a much stronger ENSO signal, with higher values in the correlation maps and warm tongue extended more westward along the tropical Pacific (Figure 5.30). The correlation between the Nino3 index and the SLP in CTL also shows an overall agreement with that in the observation. But the high pressure system over the North Atlantic in the simulation is too strong during the warm ENSO (Figure 5.31c,d), which results in an underestimation of the positive correlation between the Nino3 and the precipitation over the northern Caribbean (Figure 5.32c,d). The negative correlation between Nino3 index and the ITCZ over the Atlantic sector (Figure 5.32) represents quite well the ENSO induced zonal seesaw between the Pacific and Atlantic, which cannot be seen clearly from the observation due to its coarse spatial coverage.

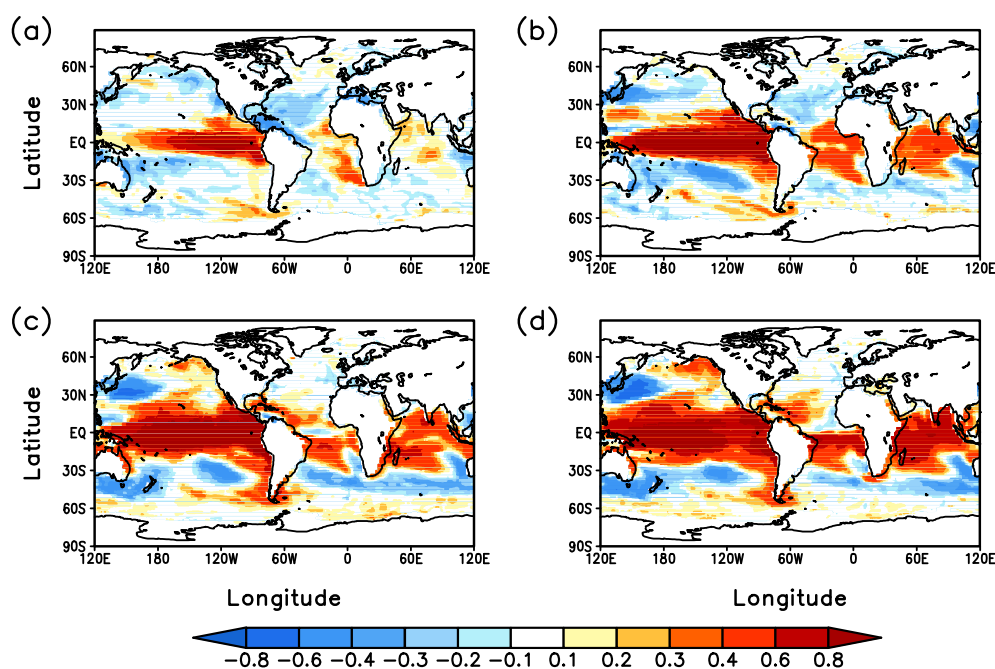


Figure 5.30 Correlation maps of simulated Nino3 index with SST during the last 100 years of the integration in CTL for (a) June-August (0), (b) September-November (0), (c) December (0)-February (+1) and (d) March-May (+1). Here, Nino3 index is defined as the December (0)-February (+1) mean SST anomalies over the area 150° - 90° W, -5° - 5° N. Significance greater than 90% is plotted.

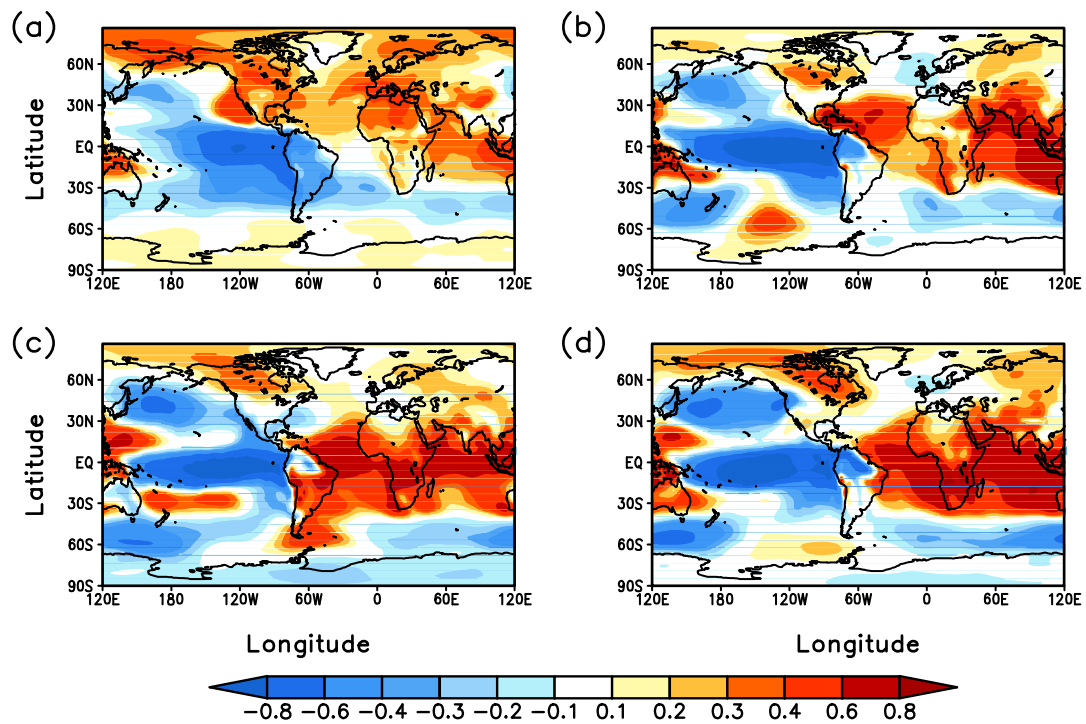


Figure 5.31 As Figure 5.30 but for the SLP

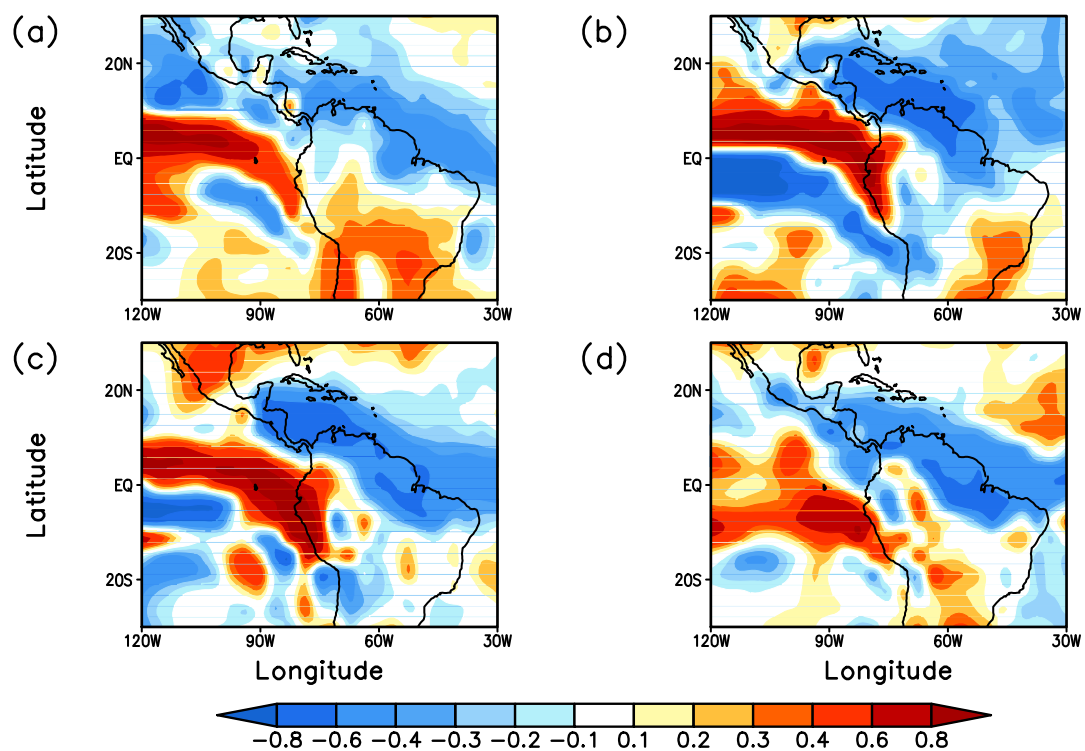


Figure 5.32 As Figure 5.30 but for the precipitation.

To detect possible change of the ENSO and its influence on the Caribbean climate during the Holocene, we apply the same analysis to the mid- and early Holocene experiments. Interestingly, the spatial patterns of the correlation between the Nino3 indices and the SSTs have no considerable change during the Holocene (Figure 5.33, Figure 5.35, Figure 5.37 and Figure 5.39), which also leads to a similar pattern in the correlation maps of Nino3 indices with the precipitation in the Caribbean (Figure 5.34, Figure 5.36, Figure 5.38 and Figure 5.40). This result indicates that the ENSO phenomenon can be a stable forcing factor that controls the seasonal and interannual climate variability in the Caribbean during the Holocene.

The climate variability associated with ENSO in the Caribbean is also documented by several proxy records. A lake sediment record from Southern Ecuador indicates that the ENSO has a continuous influence in this region over the last 12 kyr [Moy *et al.*, 2002]. They also find that changes of the ENSO on its typical 2-8 years frequency become more intensified over the Holocene until 1.2 kyr ago, which is attributed to the orbital induced change. Clement *et al.* [2000] conduct a numerical experiment with tropical Pacific driven by orbital forcing and further conclude that, the ENSO is present throughout the Holocene but undergoes a gradual increase from the mid-Holocene to the present, due to the steady warming of the eastern tropical Pacific.

However, our simulation results are not consistent with their findings. To investigate possible explanation, we analyze the amplitude of the ENSO by calculating the standard deviation (SD) of the Nino3 index and identify its frequency using MTM-spectral analysis. The SDs of the Nino3 indices over 100-year period from the observation and all the simulations are shown in Table 5.1. Notably, the SD values in the simulation are much higher than that in the observation, suggesting that magnitude of the ENSO signal is overestimated in the model. The SD difference between the simulations is relatively small, except that in H9KM the SD value is larger than the others. It might be attributed to the unsteady state of the mean climate when melting of the LIS exists.

Table 5.1 SD of the Nino3 indices based on the observation and simulations

	observation	CTL	H6K	H9KO	H9KT	H9KM
SD _{Nino3}	0.821	1.226	1.221	1.339	1.238	1.519

Results from the MTM-spectral analysis demonstrate that the periodicity of ENSO in the observation is in a range of 2-8 years, as indicated by studies based on both observation and proxies [e.g. *Rasmusson and Carpenter, 1982; Moy et al., 2002*]. However, the spectra of the Nino3 indices exhibit quasi-uniformly strong peaks around 3-4 years in all the simulations, without distinguishable change under different background climate conditions. This unimodal feature of the ENSO periodicity in the simulation might result from the relatively coarse resolution of the ocean model, which is about $5^{\circ} \times 5^{\circ}$ along the equator. As a consequence, the Kelvin waves, which signal the start of an ENSO cycle, cannot be well represented. Thus, we argue that a higher resolution should be used in order to simulate a more realistic ENSO character and its possible change during the Holocene.

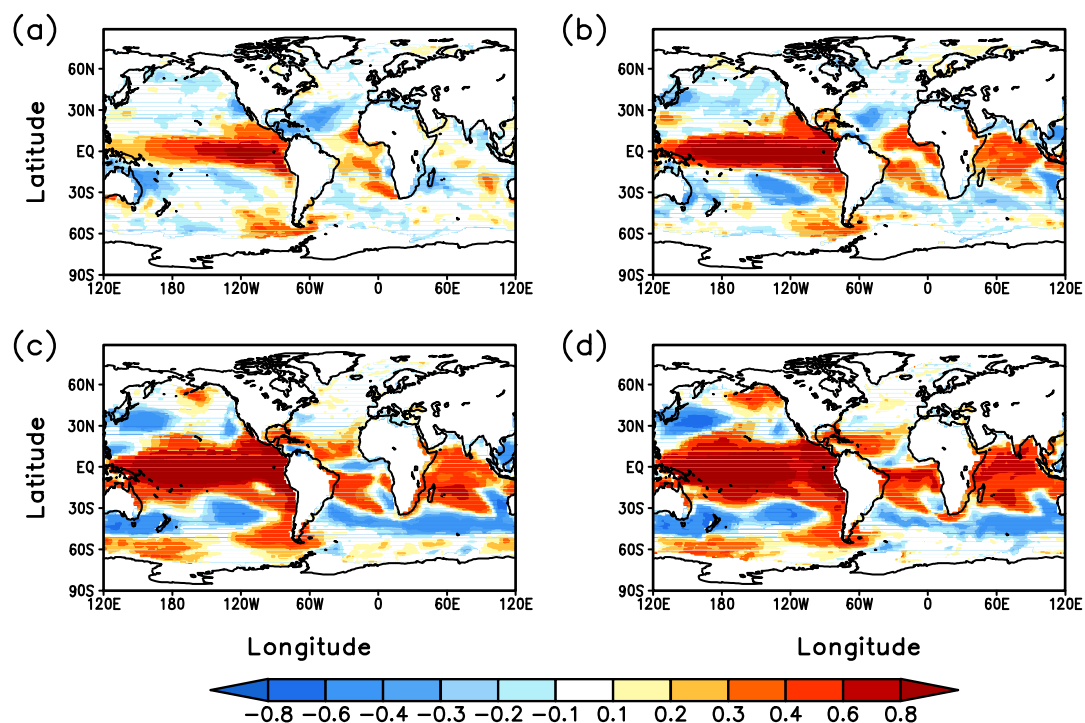


Figure 5.33 As Figure 5.30, but in H6K.

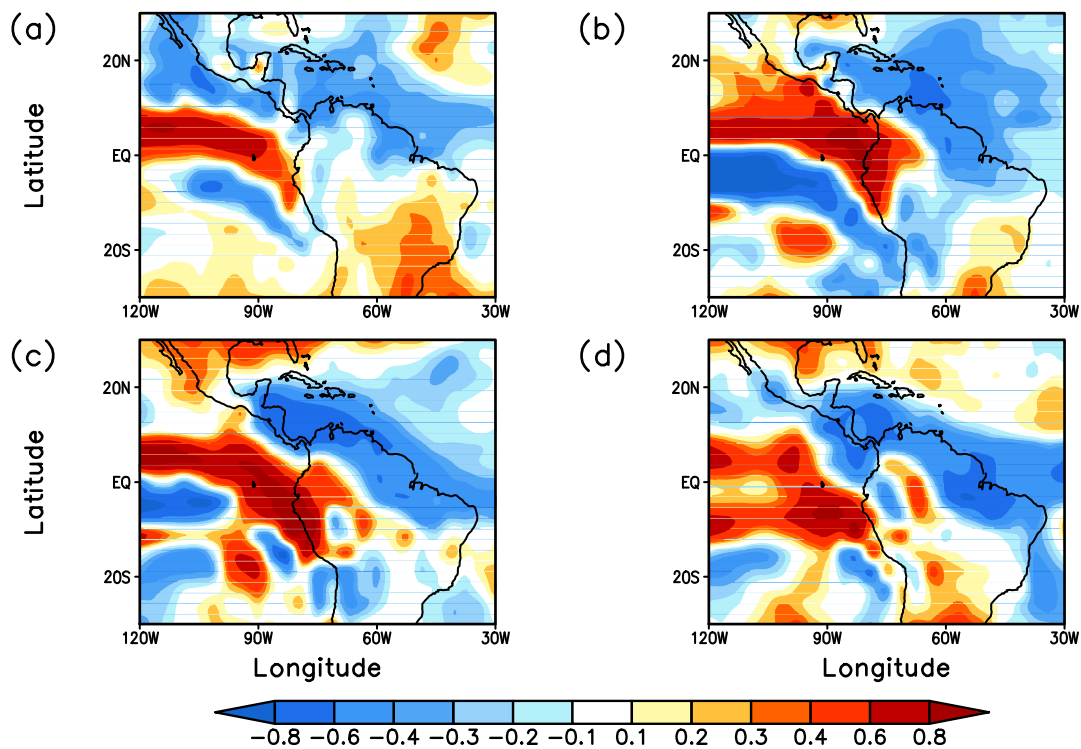


Figure 5.34 As Figure 5.32, but in H6K.

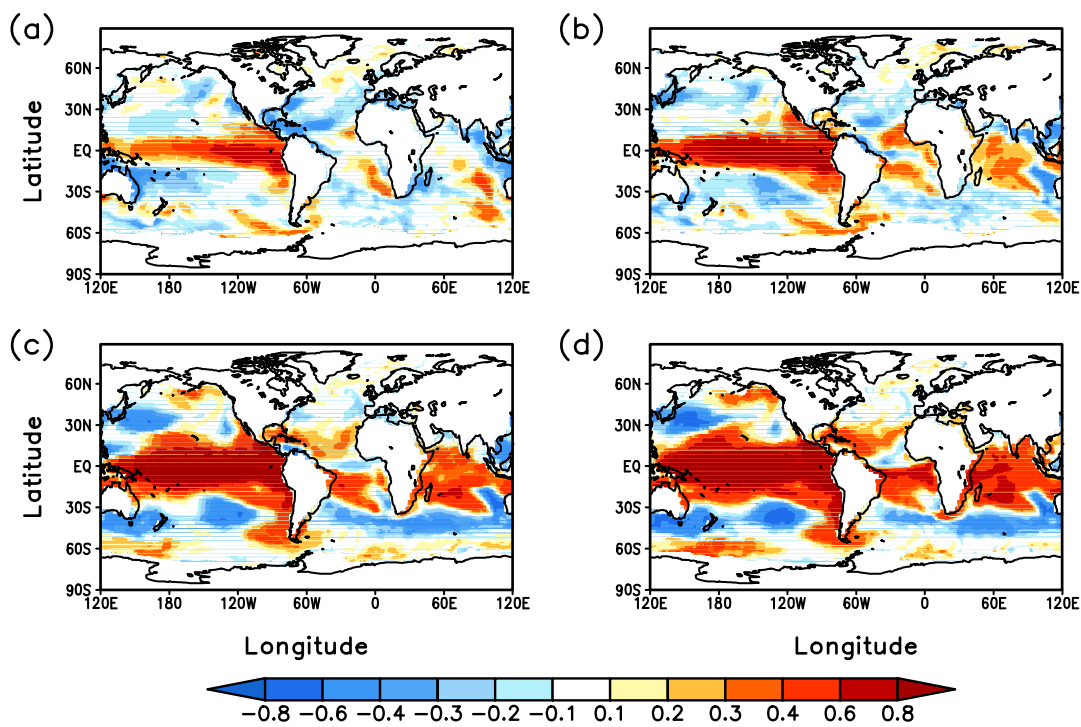


Figure 5.35 As Figure 5.30, but in H9KO.

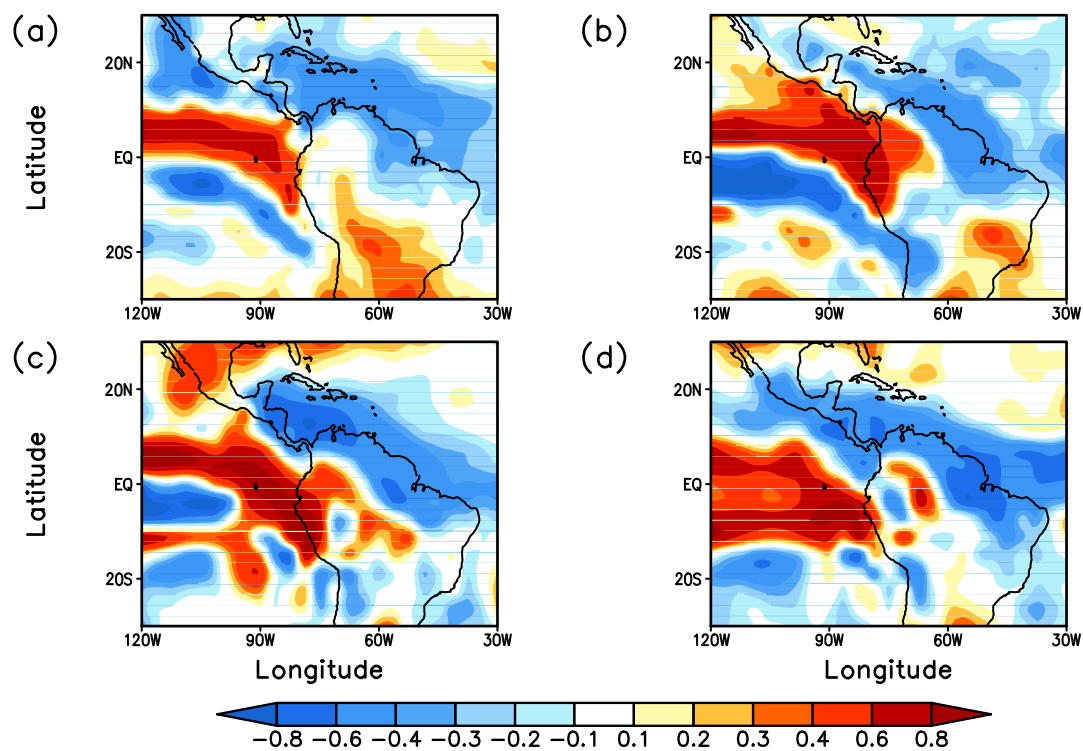


Figure 5.36 As Figure 5.32, but in H9KO.

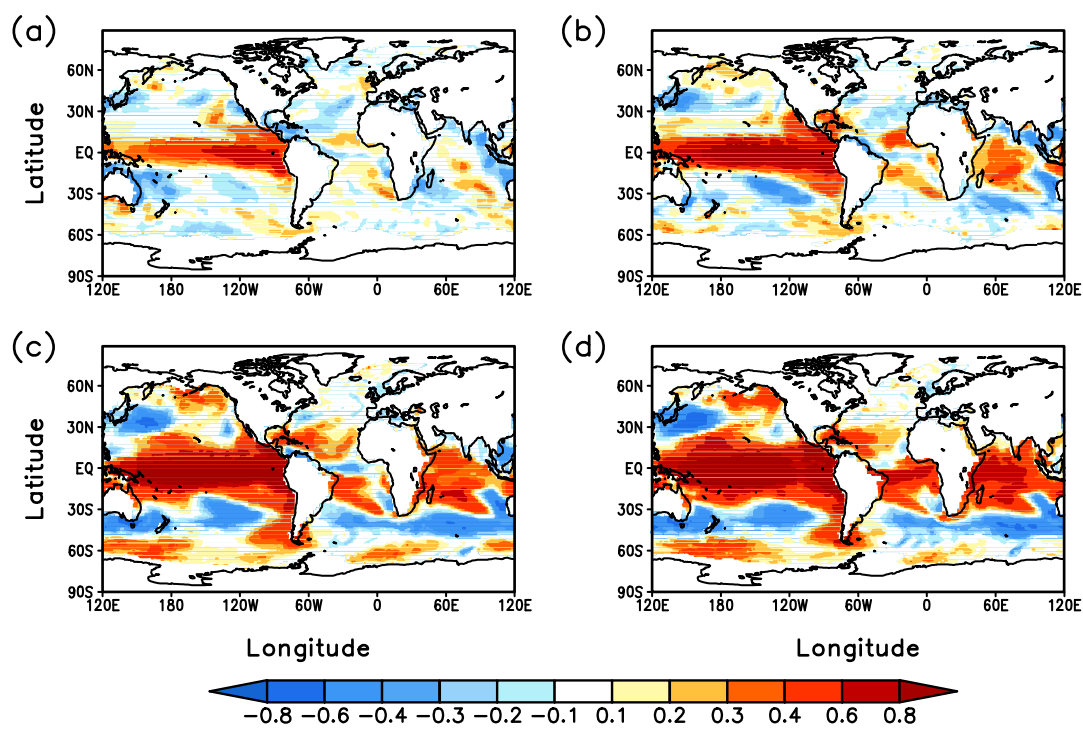


Figure 5.37 As figure 5.30, but in H9KT.

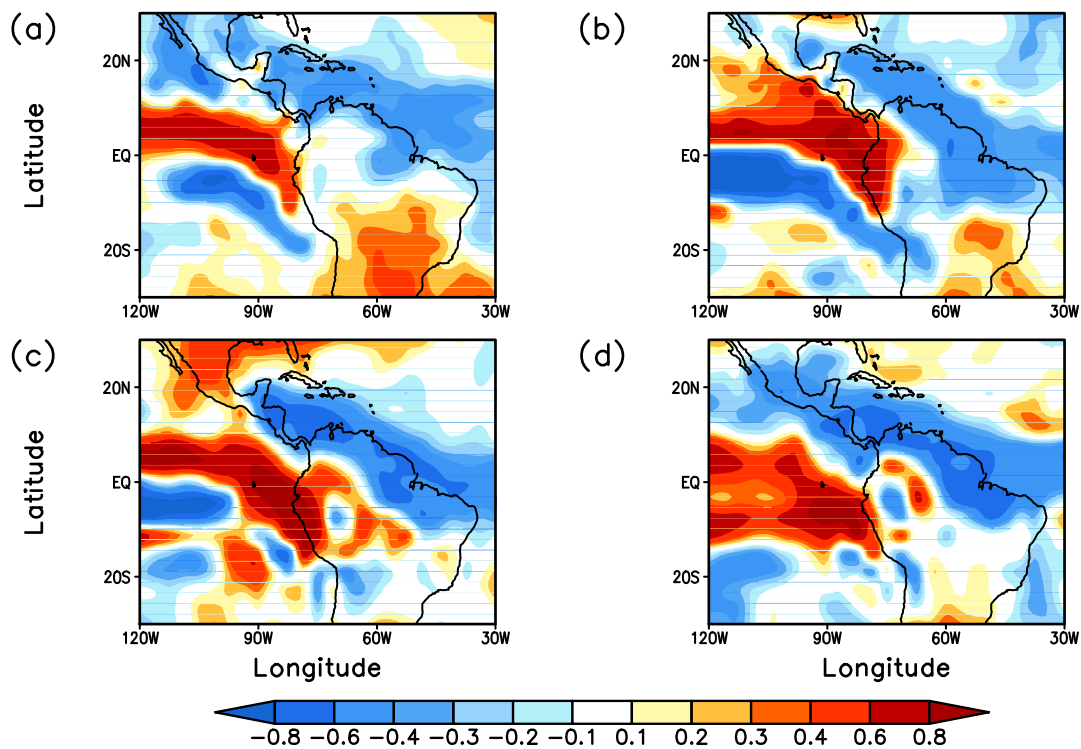


Figure 5.38 As figure 5.32, but in H9KT.

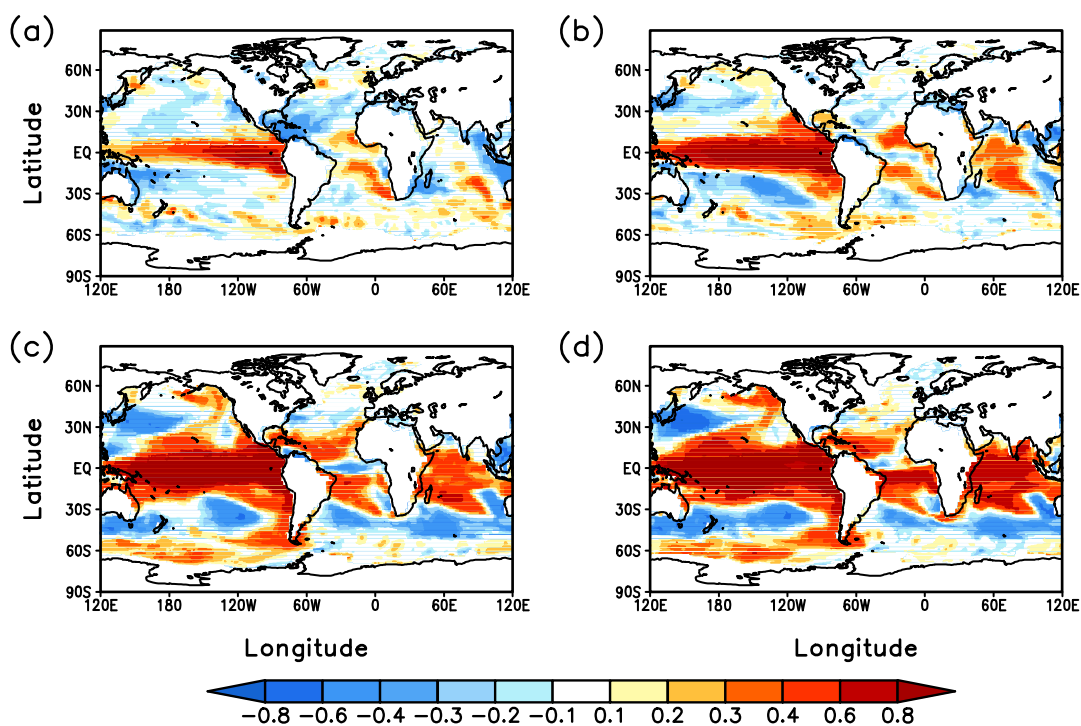


Figure 5.39 As figure 5.30, but in H9KM.

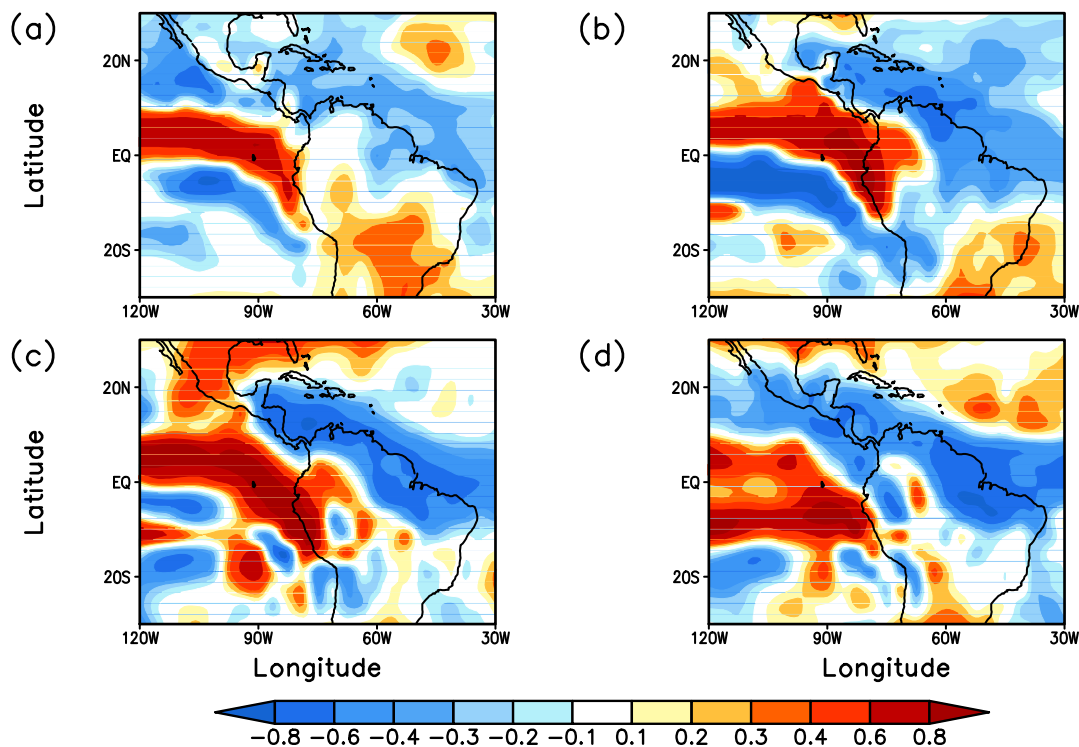


Figure 5.40 As figure 5.30, but in H9KM

To summarize the discussion above, we find that a warming in the SST and a dipole pattern in the precipitation anomalies characterize the Caribbean during a warm ENSO, which is supported by both observations and our simulations. Results from the Holocene experiments show that there is no significant change of the ENSO character and its influence on Caribbean climate during the Holocene. However, it is not consistent with evidences based on proxy records [e.g. *Sandweiss et al.*, 1996; *A. C. Clement et al.*, 2000; *Moy et al.*, 2002], which indicate that ENSO variability has an increasing trend from the mid-Holocene. We attribute this to the low resolution of the ocean model and suggest that higher resolution ocean model is needed for a better understanding of the ENSO during the Holocene.

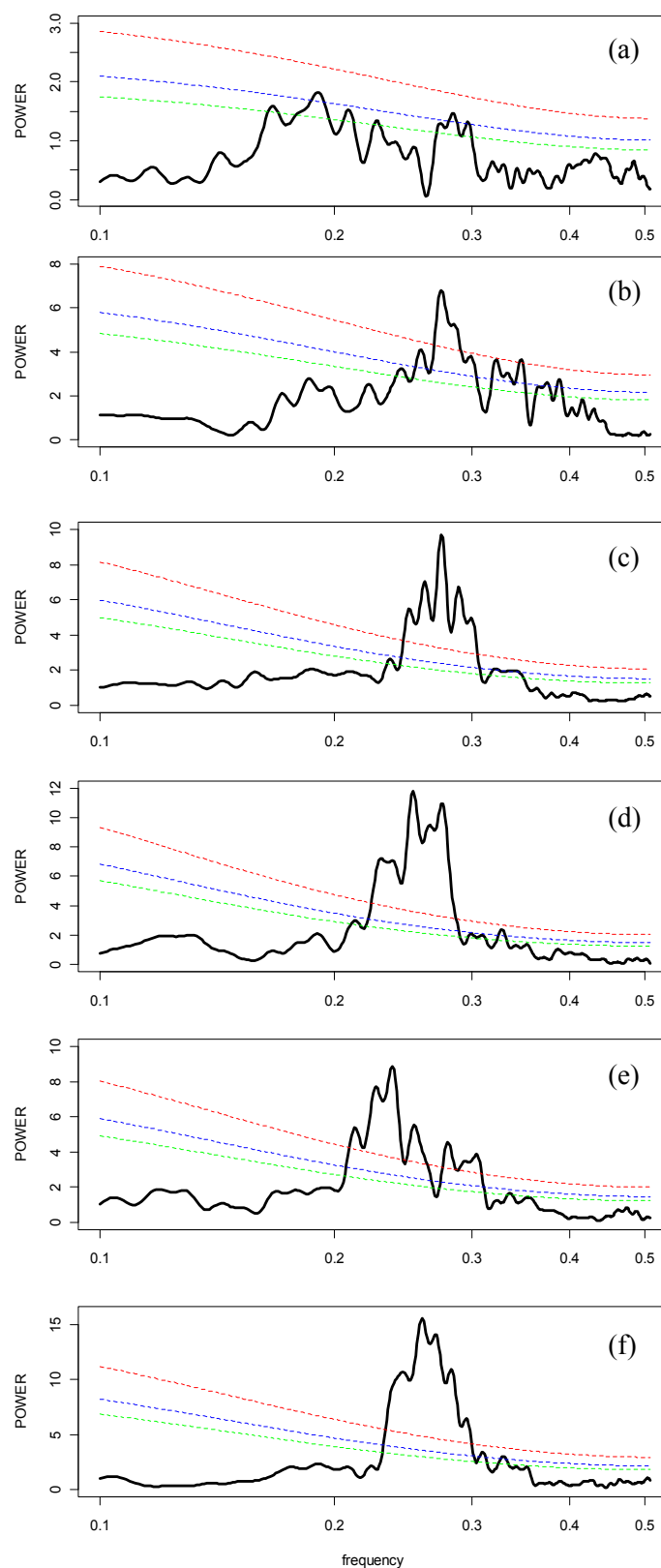


Figure 5.41 MTM spectral analysis of the Nino3 index for (a) observed HadISST, (b) CTL, (c) H6K, (d) H9KO, (e) H9KT and (f) H9KM. The significance levels of 90%, 95% and 99% are plotted by green, blue and red dotted lines, respectively.

5.2.1.2 North Atlantic Oscillation (NAO) controlled variability

The SST and the precipitation in the Caribbean are believed to be negatively related to the North Atlantic high [Hastenrath, 1976]. Anomalously high SLP in the region of the North Atlantic high can be translated into stronger trade winds, hence cooler SSTs, and less Caribbean rainfall [Giannini *et al.*, 2000]. Meanwhile, the North Atlantic high is closely connected to the Icelandic low. Thus, variations in displacement and strength of the high pressure system and the associated trade winds can result in the relationship between the NAO and precipitation patterns in the Caribbean [Malmgren *et al.*, 1998].

Figure 5.42 shows the correlation between the NAO index and SST based on the observation. Here, the NAO index (Figure 5.43) is represented by the principal component (PC) time series of the leading EOF based on the DJF SLP anomalies over the Atlantic sector (20-80°N, 90°W-40°E). The correlation coefficient is much lower in the magnitude than that in the correlation maps of the Nino3 index with the SST, suggesting that NAO plays the secondary role in controlling the Caribbean climate variability on the short timescale. Significant values appear from DJF, with negative correlation with the Caribbean SST. During years of positive NAO, a stronger-than-normal North Atlantic high governs the Caribbean, in particular north of it, and the precipitation in this area is lower than average (Figure 5.44c). During the spring following this positive NAO, drier condition can extend to the whole Caribbean region (Figure 5.44d), due to the colder-than-normal SST (Figure 5.42d).

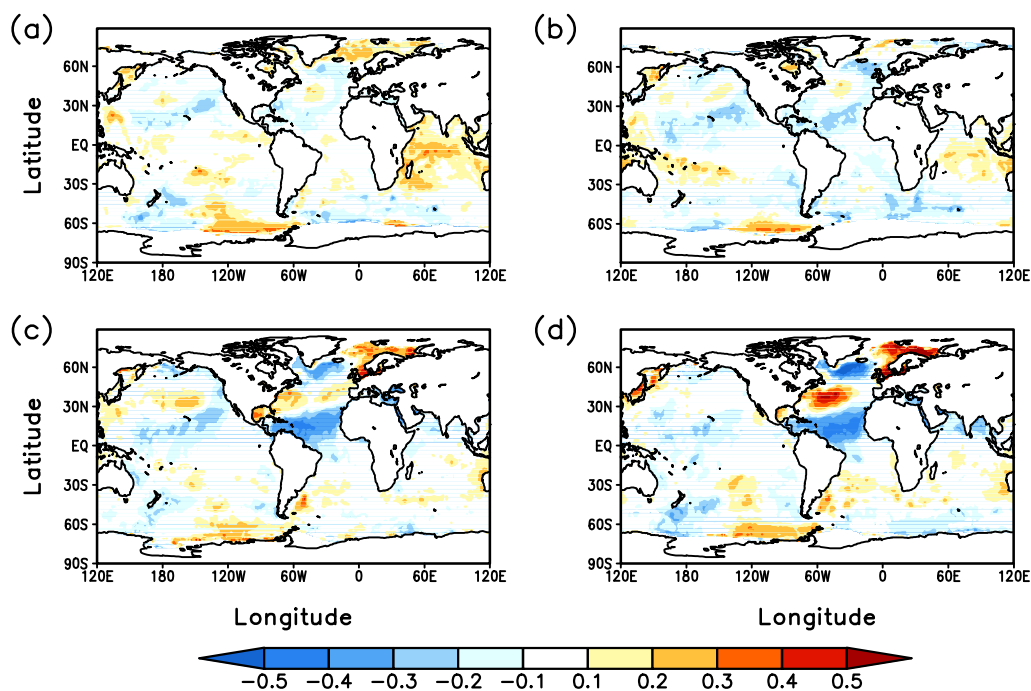


Figure 5.42 Correlation maps of NAO index [Hurrell, 1995] with HadISST [Rayner *et al.*, 2006] during 1900-1998 for (a) June-August (0), (b) September-November (0), (c) December (0)-February (+1) and (d) March-May (+1). Significance greater than 90% is plotted.

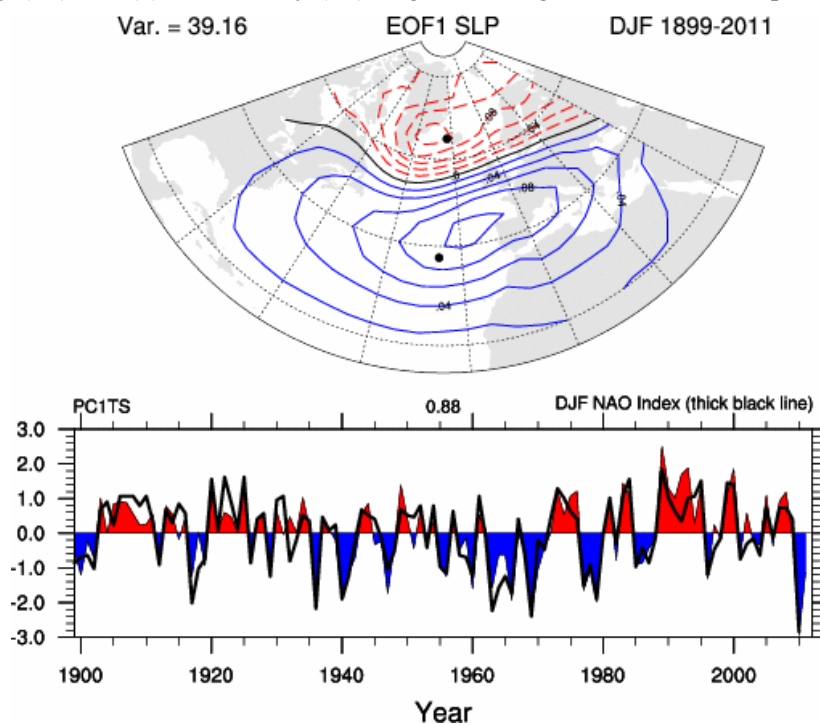


Figure 5.43 NAO index in the observation and its spatial pattern projected to the SLP anomalies over the North Atlantic. NAO Index Data is provided by the Climate Analysis Section, NCAR, Boulder, USA [Hurrell, 1995]. Figure from

<http://www.cgd.ucar.edu/cas/jhurrell/indices.html>

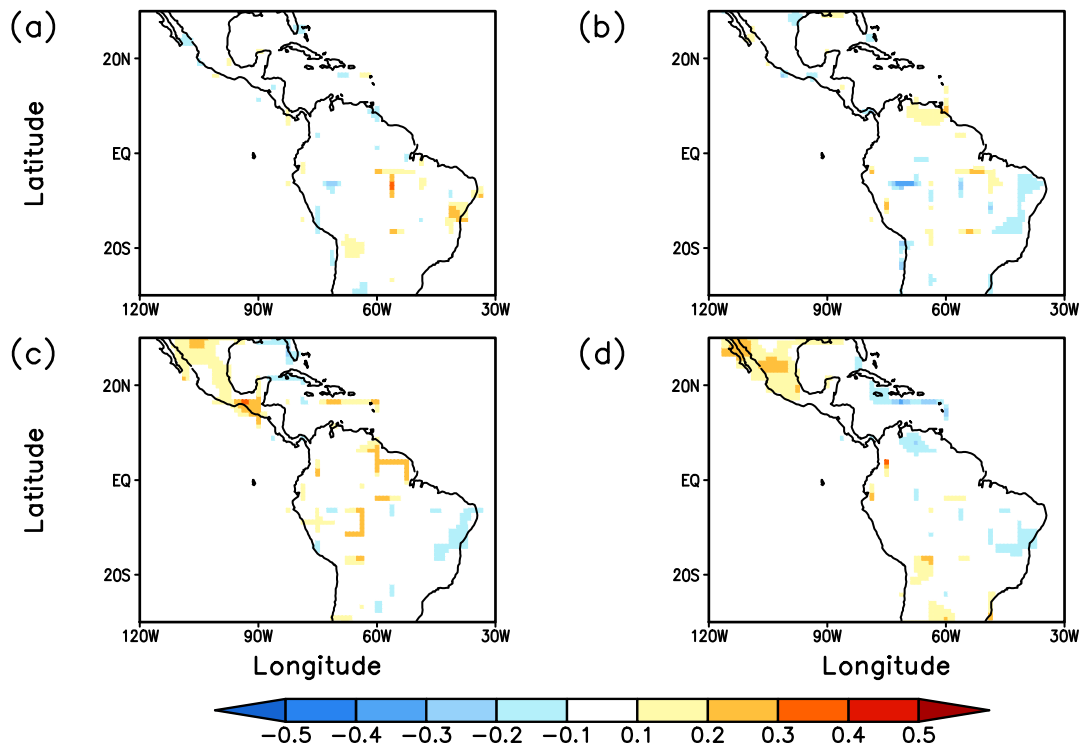


Figure 5.44 As Figure 5.42, but for the correlation maps of NAO index [Hurrell, 1995] with Hulme-CRU [Hulme *et al.*, 1998] precipitation during 1900-1992.

The NAO index in the simulation is calculated using the same method as that in the observation. The spatial pattern of the leading EOF SLP anomalies mode and its principle component in CTL are shown in Figure 5.45.

A positive NAO index phase demonstrates a stronger-than-normal subtropical high pressure center and a deeper-than-normal Icelandic low (Figure 5.45a), suggesting a good agreement with the observed NAO spatial pattern. It is worth mentioning that the leading EOF in the simulation can explain much higher total variance of the SLP anomalies than that in the observation, which is 60.17% and 39.16%, respectively.

Connection between the NAO and the Caribbean climate in the simulation is illustrated by the correlation maps of the NAO index with SST (Figure 5.46) and precipitation (Figure 5.47). For the SST, it shows a very weak correlation with the NAO index in the Caribbean. During a positive phase of NAO, stronger-than-average surface easterlies blow across the subtropical Atlantic into the Caribbean, with anomalous cooling over the Caribbean (Figure 5.46c,d) and more southward position

of the ITCZ over the Atlantic, thus less precipitation (Figure 5.47c,d). The results are in general consistent with observations, although the correlation coefficient over the Caribbean shows a smaller magnitude in the simulation than in the observation.

Throughout the Holocene, the spatial pattern of the NAO remains largely similar with that in CTL (Figure 5.48), implying a persistent and stable NAO during the Holocene. As a consequence, its influence on the Caribbean climate does not change during the Holocene (not shown). However, the SLPs over the northern North Atlantic have a decreasing trend in the simulation (not shown), which is consistent with the finding in previous studies [Rimbu *et al.*, 2003; G. Lohmann *et al.*, 2005] that the orbital change cause a weakening of the NAO from the early to late Holocene.

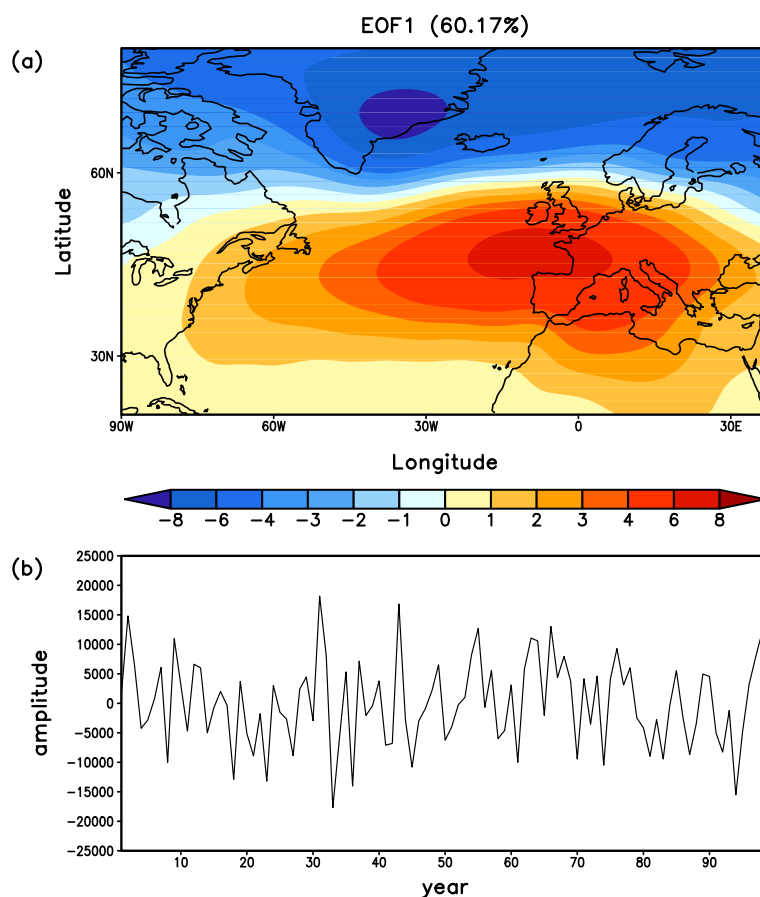


Figure 5.45 (a) The leading mode based on EOF analysis of the DJF SLP anomalies over the North Atlantic sector ($20^{\circ}\text{--}80^{\circ}\text{N}$, 90°W – 40°E) in CTL. (b) The NAO index, which is represented by the time series of the leading EOF mode.

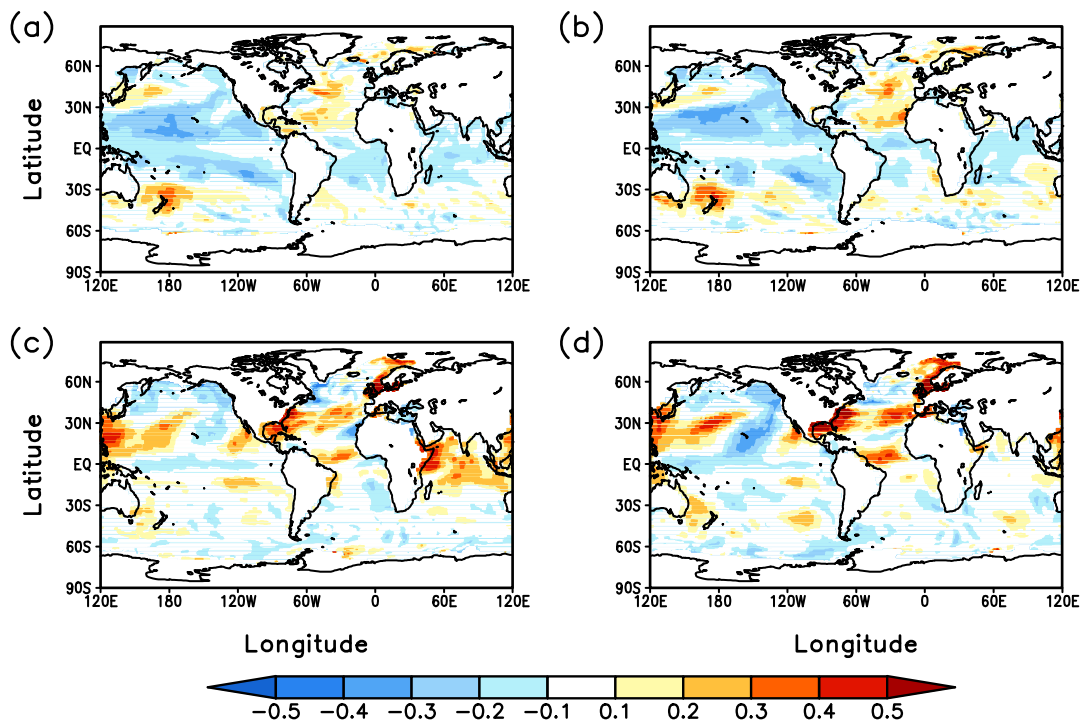


Figure 5.46 Correlation maps of simulated NAO index with SST during the last 100 years of the integration in CTL for (a) June-August (0), (b) September-November (0), (c) December (0)-February (+1) and (d) March-May (+1). Significance greater than 90% is plotted.

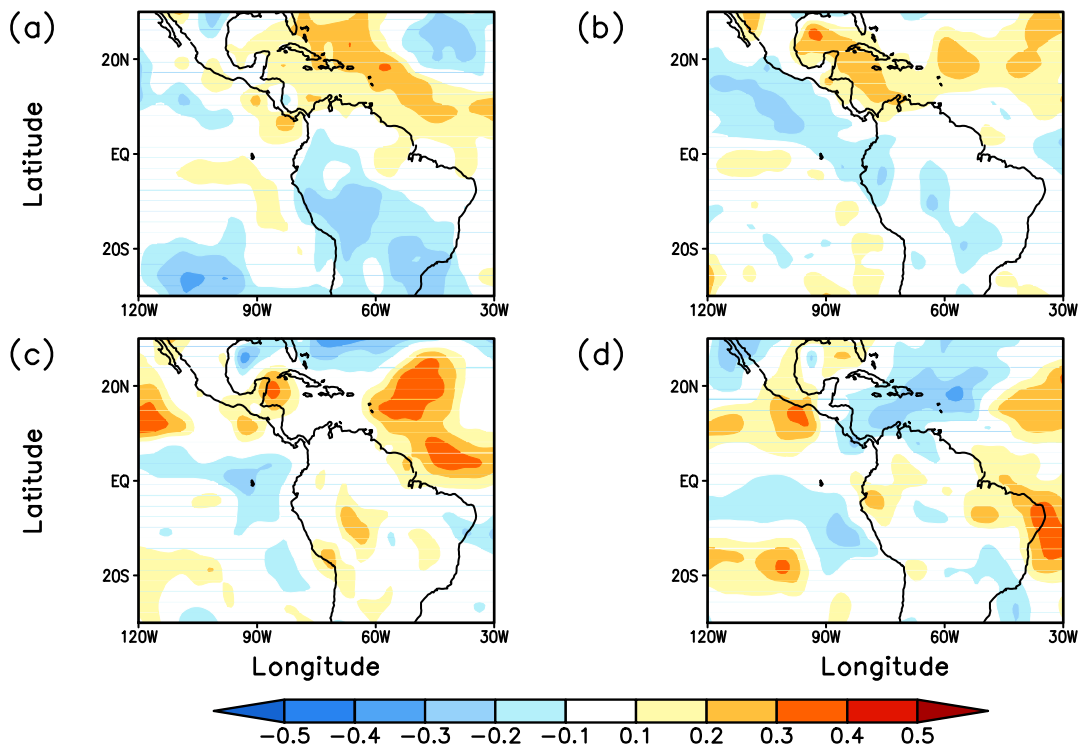


Figure 5.47 As Figure 5.45, but for the precipitation in the Caribbean.

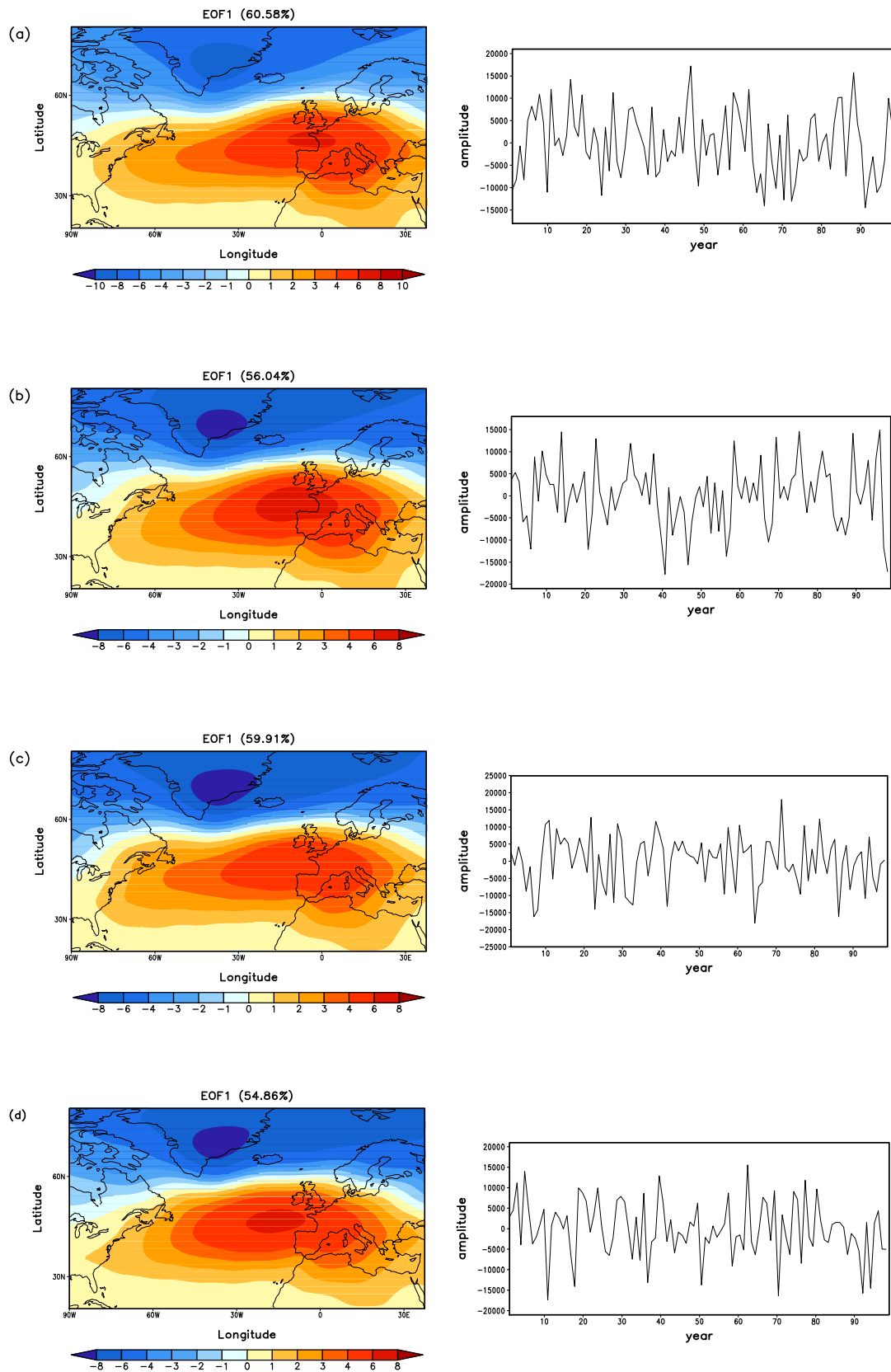


Figure 5.48 As Figure 5.45, but in (a) H6K, (b) H9KO, (c) H9KT and (d) H9KM.

5.2.2 Decadal to centennial variability

On decadal to centennial timescale, the AMO has been considered a major forcing for the climate variability over the North Hemisphere, in particular the high latitude regions [e.g. *Enfield et al.*, 2001; *Schubert et al.*, 2004; *McCabe and Palecki*, 2006]. However, focusing on the precipitation field, one can note that the strongest response to the AMO is the Atlantic ITCZ [e.g. *Sutton and Hodson*, 2005], which is closely linked to the Caribbean climate variability.

Previous studies have indicated that the AMO is driven by the AMOC [*T L Delworth and Mann*, 2000; *Dima and Lohmann*, 2007]. Meanwhile, the Caribbean Current is part of the AMOC, which transports large amount of water and heat from the tropical Atlantic to the Caribbean region. Therefore, direct influence on the Caribbean climate can also be gained by changing the AMOC.

The detailed analyses of the AMO during the Holocene have been conducted in Chapter 3. Here, we concentrate on its climate influence on the Caribbean climate. During a warm phase of the AMO, the Caribbean experiences a warming up to 0.2°C in all the simulation, except that in H9TM this value can reach 0.4 in maximum (Figure 3.6). Considering the relative low seasonal and year-to-year variation in this region, the warming induced by the positive AMO is significant. Associated with the warming, the precipitation in the Caribbean is also increased considerably, with the most pronounced wetter condition in H9KM (Figure 3.8). The AMO influence on the Caribbean climate shows no remarkable change during the Holocene in our simulation, which is evidenced by the quasi-persistent AMO feature based on the proxies through the last 8 kyr [*Knudsen et al.*, 2011]. However, it seems that a colder-than-normal condition in the North Atlantic Ocean (e.g. in H9KM) can generate a larger amplitude in the climate variability due to the less stable mean climate condition, which partly results from a vigorous AMOC fluctuation (Figure 3.7).

5.3 Summary

In this chapter, the Holocene climate variation is investigated by identifying the forcing mechanism controlling the Caribbean climate based on modeling study and model-data comparison. On millennial timescales, the orbital change and melting of the LIS are the major external forcing that modulates the Caribbean climatology. On seasonal and interannual to centennial timescales, the internal variability associated with ENSO, NAO, AMO and AMOC plays more important role in the Caribbean climate variability.

- External forcing induced mean climate change

Due to the orbital associated insolation change, the temperature in the Caribbean shows pronounced seasonality increase during the early and mid-Holocene. This seasonality increase is approximately 1°C during the mid-Holocene in the simulation, further supported by the coral based reconstruction. Influence from the LIS and its melting on the Caribbean can be contradicted, but the combined effect in the end compensates part of the warming due to the insolation.

Meanwhile, the ITCZ shifts to a more northward position in the early and mid-Holocene, resulting in a much wetter condition over the Caribbean. As a consequence, the precipitation $\delta^{18}\text{O}$ is more depleted during the early and mid-Holocene. However, this anomaly induced by the precipitation change cannot fully explain large shift in the $\delta^{18}\text{O}$ signal recorded by Cuban stalagmites. Results from sensitivity experiment, together with other proxy records nearby, suggest that the large shift of the $\delta^{18}\text{O}$ from the stalagmite record can be a combined effect of the precipitation change and local seawater $\delta^{18}\text{O}$ change.

- Internal variability

ENSO is recognized as the dominant mode of the Caribbean climate variability on seasonal and interannual timescales. A warm ENSO phase leads to positive SST anomalies in the Caribbean Sea, thus more convective rainfall. This teleconnection pattern has no detectable change during the Holocene in our simulation, which is not supported by proxy studies [e.g. *Sandweiss et al.*, 1996; *A. C. Clement et al.*, 2000;

Moy et al., 2002]. One possible explanation is attributed to the coarse resolution of the model, which cannot represent the Kelvin waves in a proper way.

NAO plays the secondary role in modulating the short timescale variability in the Caribbean. Associated with a positive phase of NAO, cooler-than-normal SST and less precipitation are the main feature in the Caribbean.

On decadal to centennial timescale, the Caribbean climate variability is linked to AMO and variation in the AMOC. A stronger AMOC can generate a positive phase of AMO, warming up the Caribbean Sea and bringing more precipitation in the basin.

In general, the internal factors controlling the Caribbean climate variability during the Holocene show no significant change. However, results from the early Holocene simulation imply that the response of the Caribbean climate to different forcing can be amplified during a cold period, when larger fluctuation exists in the climate background condition.

6. Conclusions and future perspectives

The aim of this PhD project is to provide new insights into the climate variability during the Holocene, from both the long-term ocean circulation and regional (i.e. the Caribbean region in this study) climate change perspectives. The key findings based on climate modeling and model-data comparisons can be summarized as follows:

- The orbital forcing plays the major role in controlling the climate evolution during the Holocene, which leads to increased seasonality over the North Hemisphere. Existence of the LIS and its melting can generate strong cooling locally, but affect the global climate by ocean-atmosphere circulation. The monsoon system is considerably enhanced during the early and mid-Holocene. Such changes have large impact on the ocean circulation, causing pronounced reduction in the AMOC. However, the AMO, an internal variability associated with the AMOC, shows no remarkable change during the Holocene regarding its typical 50-80 year duration as indicated by the observation. As a consequence, the climate influence of the AMO remains stable among the different Holocene experiments, except showing amplification during the early Holocene, when the background climate condition exhibits more fluctuation due to the cooling by the LIS.
- Two distinct modes in the internal variability of the GMOC, which are closely linked to the SWW anomalies, are found on multidecadal and centennial time scales. The dominant mode is characterized by Southern Ocean dynamics: strengthening or poleward shift of the SWWs associated with a positive phase of the SAM yields Ekman-induced northward mass transport, including a zonally asymmetric response in the SO SST, and a cooling in the tropical Pacific Ocean due to large-scale upwelling. The second mode projects mainly onto the AMOC. It is driven by a combination of SWW variation and buoyancy forcing. Based on

the relationship between the two modes together with the wind perturbation experiments, we emphasize that AMOC response to SWW takes several centuries in our model. The Northern Hemisphere high latitude SST is significantly affected in this mode, showing a large-scale warming. Results from a mid-Holocene experiment imply that both modes are independent from the climate background conditions in the Holocene.

- Up to 1°C increase in the seasonality during the mid-Holocene, previously found in the Bonaire coral Sr/Ca records, is confirmed by our modeling results as a regional feature in the Caribbean due to the insolation change. The northward shift of the ITCZ over the Atlantic and the South America during the early and mid-Holocene brings more precipitation to the Caribbean, which can only explain partly the 2 ‰ shift of the precipitation $\delta^{18}\text{O}$ from the early to mid-Holocene recorded by Cuban stalagmites. Results from the sensitivity experiment suggest that such a shift is mainly attributed to the $\delta^{18}\text{O}$ change in the sea water, because the oxygen isotope fractionation between the ice and sea water makes the sea water more sufficient in ^{18}O , when the LIS forms. On seasonal and interannual timescales, ENSO is the major forcing that controls of the Caribbean climate variability. A warm phase of the ENSO generates positive SST anomalies in the Caribbean Sea, favoring more rainfall due to stronger convection. On decadal to centennial timescales, the Caribbean climate is strongly linked to the AMO and variation in the AMOC. A stronger AMOC results in a positive phase of AMO, warming up the Caribbean Sea and bringing more precipitation in the basin. It is worth mentioning that their impact on the Caribbean climate is independent with the background climate conditions during the Holocene, however, its magnitude can be modulated by the mean climate.

As mentioned in the abstract, studies on the Holocene climate evolution is essential to better constrain the projection of the anthropogenic influence onto the future climate. The natural next step is to examine how the external forcing and internal variability,

elaborated in this study, work under the future climate condition. Preliminary result from a simulation with doubled CO_2 using the same model setup with the Holocene ones demonstrates a strong global warming (Figure 6.1). Such a warming can reach $4.5\text{ }^\circ\text{C}$ on the global average, in the range of estimation by IPCC A2 scenario [Solomon *et al.*, 2007].

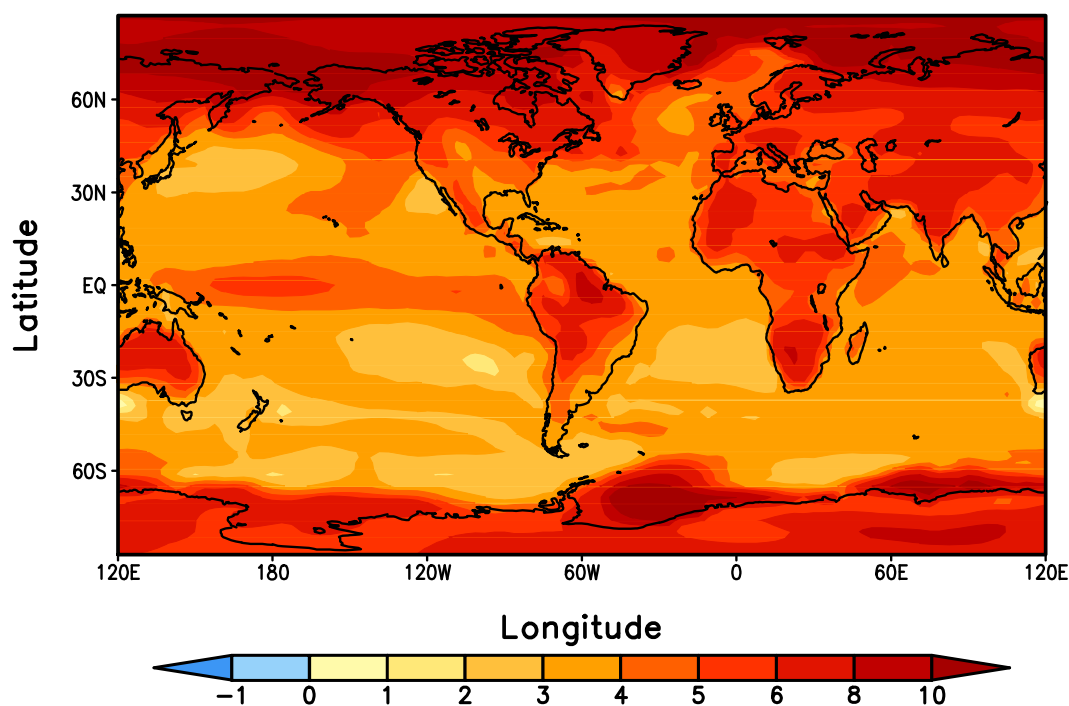


Figure 6.1 Surface air temperature anomalies (in $^\circ\text{C}$) in the simulation with double CO_2 relative to CTL. In this simulation, all the boundary conditions are identical to CTL, except that CO_2 concentration is doubled, from 280ppm to 560ppm.

However, the shortcomings of current predictive models limit our ability to project sea level change during this century and beyond. One crucial issue is that knowledge on the full effects of changes in ice sheet flow is still lacking, which hampers the assessment of a best estimate for sea level rise. Currently, an ice sheet model has been successfully coupled to COSMOS. Results from this new model setup will enable us to have more comprehensive understanding of the ice sheet dynamics, eventually more credible prediction of the future climate change.

Reference

Angeles, M. E., J. E. Gonzalez, D. J. Erickson III, and J. L. Hernández (2007), Predictions of future climate change in the caribbean region using global general circulation models, *International Journal of Climatology*, 27(5), 555-569.

Böning, C., A. Dispert, M. Visbeck, S. Rintoul, and F. Schwarzkopf (2008), The response of the Antarctic Circumpolar Current to recent climate change, *Nature Geoscience*, 1(12), 864-869.

Bak, R. (1977), Coral reefs and their zonation in Netherlands Antilles, *Stud Geol*, 4, 3-16.

Behre, K. E. (2003), *Eine neue Meeresspiegelkurve für die südliche Nordsee*, Probleme der Küstenforschung im südlichen Nordseegebiet, Isensee.

Berger, A. L. (1978), Long-term variations of daily insolation and Quaternary climatic changes, *Journal of Atmospheric Sciences*, 35, 2362-2367.

Biastoch, A., C. Böning, and J. Lutjeharms (2008), Agulhas leakage dynamics affects decadal variability in Atlantic overturning circulation, *Nature*, 456(7221), 489-492.

Biastoch, A., C. Böning, F. Schwarzkopf, and J. Lutjeharms (2009), Increase in Agulhas leakage due to poleward shift of Southern Hemisphere westerlies, *Nature*, 462(7272), 495-498.

Black, D. E., M. A. Abahazi, R. C. Thunell, A. Kaplan, E. J. Tappa, and L. C. Peterson (2007), An 8-century tropical Atlantic SST record from the Cariaco Basin: Baseline variability, twentieth-century warming, and Atlantic hurricane frequency, *Paleoceanography*, 22(26), 4204.

Braconnot, P., B. Otto-Bliesner, S. Harrison, S. Joussaume, J. Y. Peterchmitt, A. Abe-Ouchi, M. Crucifix, E. Driesschaert, T. Fichefet, and C. Hewitt (2007), Results of PMIP2 coupled simulations of the Mid-Holocene and Last Glacial Maximum-Part 1: experiments and large-scale features, *Climate of the Past*, 3(2), 261-277.

Brook, E. J., S. Harder, J. Severinghaus, E. J. Steig, and C. M. Sucher (2000), On the origin and timing of rapid changes in atmospheric methane during the last glacial period, *Global Biogeochemical Cycles*, 14(2), 559-572.

Carlson, A. E., A. N. LeGrande, D. W. Oppo, R. E. Came, G. A. Schmidt, F. S. Anslow, J. M. Licciardi, and E. A. Obbink (2008), Rapid early Holocene deglaciation of the Laurentide ice

sheet, *Nature Geoscience*, 1(9), 620-624.

Chen, A. A., and M. A. Taylor (2002), Investigating the link between early season Caribbean rainfall and the El Niño + 1 year, *International Journal of Climatology*, 22(1), 87-106.

Chiang, J. C. H. (2009), The tropics in paleoclimate, *Annual Review of Earth and Planetary Sciences*, 37, 263-297.

Chylek, P., C. K. Folland, G. Lesins, M. K. Dubey, and M. Wang (2009), Arctic air temperature change amplification and the Atlantic Multidecadal Oscillation, *Geophysical Research Letters*, 36(14), L14801.

Clement, A. C., R. Seager, and M. A. Cane (2000), Suppression of El Niño during the Mid-Holocene by Changes in the Earth's Orbit, *Paleoceanography*, 15(6), 731-737.

Clement, A. C., R. Seager, and M. A. Cane (2000), Suppression of El Niño during the mid-Holocene by changes in the Earth's orbit, *Paleoceanography*, 15(6), 731-737.

Crucifix, M., P. Braconnot, S. P. Harrison, and B. Otto-Bliesner (2005), Second Phase of Paleoclimate Modelling Intercomparison Project, *Eos Trans. AGU*, 86(28).

Döös, K., and D. J. Webb (1994), The Deacon cell and the other meridional cells of the Southern Ocean, *Journal of Physical Oceanography*, 24, 429-429.

Dansgaard, W. (1964), Stable isotopes in precipitation, *Tellus*, 16(4), 436-468.

Dansgaard, W., S. Johnsen, H. Clausen, D. Dahl-Jensen, N. Gundestrup, C. Hammer, C. Hvidberg, J. Steffensen, A. Sveinbjörnsdóttir, and J. Jouzel (1993), Evidence for general instability of past climate from a 250-kyr ice-core record, *Nature*, 364(6434), 218-220.

De Ruijter, W. (1982), Asymptotic analysis of the Agulhas and Brazil Current systems, *J. Phys. Oceanogr.*, 12(4), 361-373.

Deacon, S. (1937), *The hydrology of the Southern Ocean*, Cambridge University Press.

Delworth, T., and F. Zeng (2008), Simulated impact of altered Southern Hemisphere winds on the Atlantic meridional overturning circulation, *Geophysical Research Letters*, 35(20), L20708.

Delworth, T., S. Manabe, and R. Stouffer (1993), Interdecadal variations of the thermohaline circulation in a coupled ocean-atmosphere model, *Journal of Climate*, 6(11), 1993-2011.

Delworth, T. L., and R. J. Greatbatch (2000), Multidecadal thermohaline circulation variability driven by atmospheric surface flux forcing, *Journal of Climate*, 13(9), 1481-1495.

Delworth, T. L., and M. E. Mann (2000), Observed and simulated multidecadal variability in the Northern Hemisphere, *Climate Dynamics*, 16(9), 661-676.

Dima, M., and G. Lohmann (2007), A hemispheric mechanism for the Atlantic Multidecadal Oscillation, *Journal of Climate*, 20(11), 2706-2719.

Dima, M., and G. Lohmann (2010), Evidence for two distinct modes of large-scale ocean circulation changes over the last century, *Journal of Climate*, 23(1), 5-16.

Donnelly, J. P., and J. D. Woodruff (2007), Intense hurricane activity over the past 5,000 years controlled by El Nino and the West African monsoon, *Nature*, 447(7143), 465-468.

Downes, S. M., N. L. Bindoff, and S. R. Rintoul (2010), Changes in the Subduction of Southern Ocean Water Masses at the End of the Twenty-First Century in Eight IPCC Models, *Journal of Climate*, 23(24), 6526-6541.

Eischeid, J. K., H. Diaz, R. Bradley, and P. Jones (1991), A comprehensive precipitation data set for global land areas *Rep.*, Massachusetts Univ., Amherst, MA (USA).

Enfield, D., A. Mestas-Nunez, and P. Trimble (2001), The Atlantic multidecadal oscillation and its relation to rainfall and river flows in the continental U. S., *Geophysical Research Letters*, 28(10), 2077-2080.

Fairbanks, R. G. (1989), A 17, 000-year glacio-eustatic sea level record: influence of glacial melting rates on the Younger Dryas event and deep-ocean circulation, *Nature*, 342(6250), 637-642.

Farneti, R., and T. L. Delworth (2010), The Role of Mesoscale Eddies in the Remote Oceanic Response to Altered Southern Hemisphere Winds, *Journal of Physical Oceanography*, 40(10), 2348-2354.

Farneti, R., T. Delworth, A. Rosati, S. Griffies, and F. Zeng (2010), The role of mesoscale eddies in the rectification of the Southern Ocean response to climate change, *Journal of Physical Oceanography*.

Feng, S., Q. Hu, and R. J. Oglesby (2009), AMO-like variations of holocene sea surface temperatures in the North Atlantic Ocean, *Clim Past Discuss*, 5, 2465-2496.

Feng, S., Q. Hu, and R. J. Oglesby (2010), Influence of Atlantic sea surface temperatures on persistent drought in North America, *Climate Dynamics*, 1-18.

Fensterer, C. (2011), Holocene Caribbean climate variability reconstructed from speleothems from western Cuba, *PhD dissertation*, University of Heidelberg, Germany, 1-173.

Fensterer, C., D. Scholz, D. Hoffmann, A. Mangini, and J. M. Pajón (2010), 230Th/U-dating of a late Holocene low uranium speleothem from Cuba, IOP Publishing.

Fischer, N., and J. JungCLAUS (2009), Effects of orbital forcing on atmosphere and ocean heat transports in Holocene and Eemian climate simulations with a comprehensive Earth system model, *Climate of the Past Discussions*, 5, 2311-2341.

FolkINS, I., and C. Braun (2003), Tropical Rainfall and Boundary Layer Moist Entropy, *Journal of Climate*, 16(11), 1807-1820.

Folland, C., T. Palmer, and D. Parker (1986), Sahel rainfall and worldwide sea temperatures, 1901-85, *Nature*, 320(6063), 602-607.

Folland, C. K., A. W. Colman, D. P. Rowell, and M. K. Davey (2001), Predictability of northeast Brazil rainfall and real-time forecast skill, 1987-98, *Journal of Climate*, 14(9), 1937-1958.

Fyfe, J., and O. Saenko (2006), Simulated changes in the extratropical Southern Hemisphere winds and currents, *Geophys. Res. Lett.*, 33, L06701.

Fyfe, J., O. Saenko, K. Zickfeld, M. Eby, and A. Weaver (2007), The role of poleward-intensifying winds on Southern Ocean warming, *Journal of Climate*, 20(21), 5391-5400.

Ganachaud, A., and C. Wunsch (2000), Improved estimates of global ocean circulation, heat transport and mixing from hydrographic data, *Nature*, 408(6811), 453-457.

Gent, P., J. Willebrand, T. McDougall, and J. McWilliams (1995), Parameterizing eddy-induced tracer transports in ocean circulation models, *Journal of Physical Oceanography*, 25(4), 463-474.

Giannini, A., Y. Kushnir, and M. A. Cane (2000), Interannual Variability of Caribbean Rainfall, ENSO, and the Atlantic Ocean*, *Journal of Climate*, 13(2), 297-311.

Giannini, A., Y. Kushnir, and M. Cane (2001), Seasonality in the impact of ENSO and the North Atlantic high on Caribbean rainfall, *Physics and Chemistry of the Earth, Part B: Hydrology, Oceans and Atmosphere*, 26(2), 143-147.

Giannini, A., J. C. H. Chiang, M. A. Cane, Y. Kushnir, and R. Seager (2010), The ENSO Teleconnection to the Tropical Atlantic Ocean: Contributions of the Remote and Local SSTs to Rainfall Variability in the Tropical Americas*.

Gibson, J. K., P. Kållberg, S. Uppala, A. Hernandez, A. Nomura, and E. Serrano (1997), *ERA-15 Project Report Series, ERA Description, 1*.

- Giry, C. (2011), Tropical Atlantic climate variability during the mid- to late Holocene: insights from monthly resolved coral records, *PhD dissertation, University of Bremen, Germany*.
- Giry, C., T. Felis, M. Kölling, and S. Scheffers (2010a), Geochemistry and skeletal structure of *Diploria strigosa*, implications for coral-based climate reconstruction, *Palaeogeography, Palaeoclimatology, Palaeoecology*.
- Giry, C., T. Felis, S. Scheffers, and C. Fensterer (2010b), Assessing the potential of Southern Caribbean corals for reconstructions of Holocene temperature variability, IOP Publishing.
- Giry, C., T. Felis, M. Kölling, D. Scholz, W. Wei, and S. Scheffers (2011), Mid- to late Holocene changes in tropical Atlantic temperature seasonality and interannual to multidecadal variability documented in southern Caribbean coral records, *Submitted to Earth and Planetary Science Letters*.
- Gnanadesikan, A., and R. Hallberg (2000), On the relationship of the Circumpolar Current to Southern Hemisphere winds in coarse-resolution ocean models, *Journal of Physical Oceanography*, 30(8), 2013-2034.
- Gnanadesikan, A., R. Slater, P. Swathi, and G. Vallis (2005), The energetics of ocean heat transport, *Journal of Climate*, 18(14), 2604-2616.
- Goldenberg, S. B., C. W. Landsea, A. M. Mestas-Núñez, and W. M. Gray (2001), The recent increase in Atlantic hurricane activity: Causes and implications, *Science*, 293(5529), 474.
- Gong, D., and S. Wang (1999), Definition of Antarctic oscillation index, *Geophysical Research Letters*, 26(4), 459-462.
- Gray, S. T., L. J. Graumlich, J. L. Betancourt, and G. T. Pederson (2004), A tree-ring based reconstruction of the Atlantic Multidecadal Oscillation since 1567 AD, *Geophysical Research Letters*, 31(12), L12205.
- Grosfeld, K., G. Lohmann, N. Rambu, K. Fraedrich, and F. Lunkeit (2007), Atmospheric multidecadal variations in the North Atlantic realm: proxy data, observations, and atmospheric circulation model studies, *Climate of the Past*, 3(1), 39-50.
- Hagemann, S., and L. Dümenil (1998), A parametrization of the lateral waterflow for the global scale, *Climate Dynamics*, 14(1), 17-31.
- Hagemann, S., and L. Gates (2003), Improving a subgrid runoff parameterization scheme for climate models by the use of high resolution data derived from satellite observations, *Climate Dynamics*, 21(3), 349-359.

Hallberg, R., and A. Gnanadesikan (2006), The role of eddies in determining the structure and response of the wind-driven Southern Hemisphere overturning: Results from the Modeling Eddies in the Southern Ocean (MESO) project, *Journal of Physical Oceanography*, 36(12), 2232-2252.

Hartmann, D. L., J. M. Wallace, V. Limpasuvan, D. W. J. Thompson, and J. R. Holton (2000), Can ozone depletion and global warming interact to produce rapid climate change?, *Proceedings of the National Academy of Sciences of the United States of America*, 97(4), 1412.

Hastenrath, S. (1976), Variations in low-latitude circulation and extreme climatic events in the tropical Americas, *Journal of Atmospheric Sciences*, 33, 202-215.

Haug, G. H., K. A. Hughen, D. M. Sigman, L. C. Peterson, and U. Röhl (2001), Southward migration of the Intertropical Convergence Zone through the Holocene, *Science*, 293(5533), 1304.

Haug, G. H., D. Günther, L. C. Peterson, D. M. Sigman, K. A. Hughen, and B. Aeschlimann (2003), Climate and the Collapse of Maya Civilization, *Science*, 299(5613), 1731-1735.

Herold, M., and G. Lohmann (2009), Eemian tropical and subtropical African moisture transport: an isotope modelling study, *Climate Dynamics*, 33(7), 1075-1088.

Heslop, D., and A. Paul (2010), Can oceanic paleothermometers reconstruct the Atlantic Multidecadal Oscillation?, *Climate of the Past Discussions*, 6, 2177-2197.

Hetzinger, S., M. Pfeiffer, W.-C. Dullo, E. Ruprecht, and D. Garbe-Schönberg (2006), Sr/Ca and $d^{18}O$ in a fast-growing *Diploria strigosa* coral: Evaluation of a new climate archive for the tropical Atlantic, *Geochemistry Geophysics Geosystems*, 7, Q10002, doi:10.1029/2006GC001347.

Hetzinger, S., M. Pfeiffer, W. C. Dullo, N. Keenlyside, M. Latif, and J. Zinke (2008), Caribbean coral tracks Atlantic Multidecadal Oscillation and past hurricane activity, *Geology*, 36(1), 11.

Hibler III, W. (1979), A dynamic thermodynamic sea ice model, *Journal of Physical Oceanography*, 9(4), 815-846.

Hirabara, M., H. Ishizaki, and I. Ishikawa (2007), Effects of the Westerly Wind Stress over the Southern Ocean on the Meridional Overturning, *Journal of Physical Oceanography*, 37(8), 2114-2132.

Hodell, D. A., J. H. Curtis, and M. Brenner (1995), Possible role of climate in the collapse of Classic Maya civilization, *Nature*, 375(6530), 391-394.

Hodell, D. A., J. H. Curtis, G. A. Jones, A. Higuera-Gundy, M. Brenner, M. W. Binford, and K. T. Dorsey (1991), Reconstruction of Caribbean climate change over the past 10,500 years.

Hoffmann, G., M. Werner, and M. Heimann (1998), Water isotope module of the ECHAM atmospheric general circulation model: A study on timescales from days to several years, *Journal of Geophysical Research*, *103*(D14), 16871-16816,16896.

Hogg, A. M. C., M. P. Meredith, J. R. Blundell, and C. Wilson (2008), Eddy heat flux in the Southern Ocean: response to variable wind forcing, *Journal of Climate*, *21*(4), 608-620.

Horn, C. (2010), Spatial variations of the phaseshift between ocean surface warming, evaporation and changes of continental ice volume at terminations I and II, *PhD dissertation, IFM-GEOMAR, Leibniz Institute for Marine Sciences, Kiel. In prep.*

Hu, Q., and S. Feng (2008), Variation of the North American Summer Monsoon Regimes and the Atlantic Multidecadal Oscillation, *Journal of Climate*, *21*(11), 2371-2383.

Hulme, M., T. J. Osborn, and T. C. Johns (1998), Precipitation sensitivity to global warming: Comparison of observations with HadCM2 simulations, *Geophysical Research Letters*, *25*, 3379-3382.

Hurrell, J. W. (1995), Decadal Trends in the North Atlantic Oscillation: Regional Temperatures and Precipitation, *Science*, *269*(5224), 676-679.

Indermühle, A., T. Stocker, F. Joos, H. Fischer, H. Smith, M. Wahlen, B. Deck, D. Mastroianni, J. Tschumi, and T. Blunier (1999), Holocene carbon-cycle dynamics based on CO₂ trapped in ice at Taylor Dome, Antarctica, *Nature*, *398*.

Ionita, M., G. Lohmann, N. Rimbu, and K. Wiltshire (2008), The influence of large-scale atmospheric circulation on the variability of salinity at Helgoland Roads station, *Tellus A*, *60*(5), 1103-1108.

Jeffreys, H. (1925), On the formation of water waves by wind, *Proceedings of the Royal Society of London. Series A, Containing Papers of a Mathematical and Physical Character*, *107*(742), 189-206.

Johnson, H., and D. Marshall (2004), Global teleconnections of meridional overturning circulation anomalies, *Journal of Physical Oceanography*, *34*, 1702-1722.

Jury, M., B. A. Malmgren, and A. Winter (2007), Subregional precipitation climate of the Caribbean and relationships with ENSO and NAO, *Journal of Geophysical Research*, *112*(D16), D16107.

Kalnay, E., M. Kanamitsu, R. Kistler, W. Collins, D. Deaven, L. Gandin, M. Iredell, S. Saha,

G. White, and J. Woollen (1996), The NMC/NCAR 40-year reanalysis project, *Bull. Amer. Meteor. Soc.*, 77, 437-471.

Kaplan, A., Y. Kushnir, and M. A. Cane (2000), Reduced space optimal interpolation of historical marine sea level pressure, *J. Clim.*, 13, 2987-C3002.

Kerr, R. A. (2000), A North Atlantic climate pacemaker for the centuries, *Science*, 288(5473), 1984.

Kerr, R. A. (2000), A North Atlantic Climate Pacemaker for the Centuries, *Science*, 288(5473), 1984-1985.

Klinger, B., and C. Cruz (2009), Decadal response of global circulation to Southern Ocean zonal wind stress perturbation, *Journal of Physical Oceanography*, 39, 1888-1904.

Knaff, J. A. (1997), Implications of summertime sea level pressure anomalies in the tropical Atlantic region, *Journal of Climate*, 10(4), 789-804.

Knight, J. R., C. K. Folland, and A. A. Scaife (2006), Climate impacts of the Atlantic multidecadal oscillation, *Geophys. Res. Lett.*, 33, L17706.

Knight, J. R., R. J. Allan, C. K. Folland, M. Vellinga, and M. E. Mann (2005), A signature of persistent natural thermohaline circulation cycles in observed climate, *Geophys. Res. Lett.*, 32(L20708).

Knorr, G., and G. Lohmann (2003), Southern Ocean origin for the resumption of Atlantic thermohaline circulation during deglaciation, *Nature*, 424(6948), 532-536.

Knorr, G., and G. Lohmann (2007), Rapid transitions in the Atlantic thermohaline circulation triggered by global warming and meltwater during the last deglaciation, *Geochemistry Geophysics Geosystems*, 8(12), Q12006.

Knudsen, M. F., M. S. Seidenkrantz, B. H. Jacobsen, and A. Kuijpers (2011), Tracking the Atlantic Multidecadal Oscillation through the last 8,000 years, *Nature Communications*, 2, 178.

Kuhlbrodt, T., A. Griesel, M. Montoya, A. Levermann, M. Hofmann, and S. Rahmstorf (2007), On the driving processes of the Atlantic meridional overturning circulation, *Reviews of Geophysics*, 45(2).

Kutzbach, J., and Z. Liu (1997), Response of the African monsoon to orbital forcing and ocean feedbacks in the middle Holocene, *Science*, 278(5337), 440.

Lachniet, M. S. (2009), Climatic and environmental controls on speleothem oxygen-isotope

values, *Quaternary Science Reviews*, 28(5-6), 412-432.

Lachniet, M. S., S. J. Burns, D. R. Piperno, Y. Asmerom, V. J. Polyak, C. M. Moy, and K. Christenson (2004), A 1500-year El Nino/Southern Oscillation and rainfall history for the Isthmus of Panama from speleothem calcite, *Journal of Geophysical Research*, 109(D20117).

Latif, M., et al. (2004), Reconstructing, Monitoring, and Predicting Multidecadal-Scale Changes in the North Atlantic Thermohaline Circulation with Sea Surface Temperature, *Journal of Climate*, 17(7), 1605-1614.

Lea, D. W., D. K. Pak, L. C. Peterson, and K. A. Hughen (2003), Synchronicity of tropical and high-latitude Atlantic temperatures over the last glacial termination, *Science*, 301(5638), 1361.

LeGrande, A. N., and G. A. Schmidt (2006), Global gridded data set of the oxygen isotopic composition in seawater, *Geophysical Research Letters*, 33(12), L12604.

Licciardi, J. M., J. T. Teller, and P. U. Clark (1999), Freshwater routing by the Laurentide Ice Sheet during the last deglaciation, *Mechanisms of global climate change at millennial time scales*, 112, 177-C201.

Lohmann, G. (2003), Atmospheric and oceanic freshwater transport during weak Atlantic overturning circulation, *Tellus A*, 55(5), 438-449.

Lohmann, G., N. Rimbu, and M. Dima (2004), Climate signature of solar irradiance variations: analysis of long-term instrumental, historical, and proxy data, *International Journal of Climatology*, 24(8), 1045-1056.

Lohmann, G., S. Lorenz, and M. Prange (2005), Northern high-latitude climate changes during the Holocene as simulated by circulation models, *The Nordic seas: an integrated perspective: oceanography, climatology, biogeochemistry, and modeling*, 273.

Lorenz, E. (1956), Empirical orthogonal functions and statistical weather prediction. Statistical Forecasting Project Scientific Rep.1, Defense Doc. Center 110268, Massachusetts Institute of Technology, 49.

Lorenz, S. J., and G. Lohmann (2004), Acceleration technique for Milankovitch type forcing in a coupled atmosphere-ocean circulation model: method and application for the Holocene, *Climate Dynamics*, 23(7), 727-743.

Lorenz, S. J., J. H. Kim, N. Rimbu, R. R. Schneider, and G. Lohmann (2006), Orbitally driven insolation forcing on Holocene climate trends: Evidence from alkenone data and climate modeling, *Paleoceanography*, 21(1), PA1002.

- Lovenduski, N. S., and N. Gruber (2005), Impact of the Southern Annular Mode on Southern Ocean circulation and biology, *Geophys. Res. Lett.*, *32*(11), L11603.
- Lu, R., B. Dong, and H. Ding (2006), Impact of the Atlantic Multidecadal Oscillation on the Asian summer monsoon, *Geophys. Res. Lett.*, *33*, L24701.
- Ma, H., L. Wu, and C. Li (2010), The role of southern high latitude wind stress in global climate, *Advances in Atmospheric Sciences*, *27*(2), 371-381.
- Malmgren, B. A., A. Winter, and D. Chen (1998), El Nino-southern oscillation and North Atlantic oscillation control of climate in Puerto Rico, *Journal of Climate*, *11*(10), 2713-2717.
- Mangini, A., P. Blumbach, P. Verdes, C. Spill, D. Scholz, H. Machel, and S. Mahon (2007), Combined records from a stalagmite from Barbados and from lake sediments in Haiti reveal variable seasonality in the Caribbean between 6.7 and 3 ka BP, *Quaternary Science Reviews*, *26*(9-10), 1332-1343.
- Mann, M., J. Park, and R. Bradley (1995), Global interdecadal and century-scale climate oscillations during the past five centuries, *Nature*, *378*(6554), 266-270.
- Mann, M. E., J. Park, and R. Bradley (1995), Global interdecadal and century-scale climate oscillations during the past five centuries, *Nature*, *378*(6554), 266-269.
- Marshall, G. J. (2003), Trends in the Southern Annular Mode from observations and reanalyses, *Journal of Climate*, *16*(24), 4134-4143.
- Marshall, G. J., P. A. Stott, J. Turner, W. M. Connolley, J. C. King, and T. A. Lachlan-Cope (2004), Causes of exceptional atmospheric circulation changes in the Southern Hemisphere, *Geophysical Research Letters*, *31*(14), L14205.
- Marsland, S., H. Haak, J. Jungclaus, M. Latif, and F. Riske (2003), The Max-Planck-Institute global ocean/sea ice model with orthogonal curvilinear coordinates, *Ocean Modelling*, *5*(2), 91-127.
- Martis, A., G. J. van Oldenborgh, and G. Burgers (2002), Predicting rainfall in the Dutch Caribbean—more than El Niño?, *International Journal of Climatology*, *22*(10), 1219-1234.
- McCabe, G. J., and M. A. Palecki (2006), Multidecadal climate variability of global lands and oceans, *International Journal of Climatology*, *26*(7), 849-865.
- McCabe, G. J., M. A. Palecki, and J. L. Betancourt (2004), Pacific and Atlantic Ocean influences on multidecadal drought frequency in the United States, *Proceedings of the National Academy of Sciences of the United States of America*, *101*(12), 4136.

- McDermott, D. (1996), The regulation of northern overturning by Southern Hemisphere winds, *Journal of Physical Oceanography*, 26(7), 1234-1255.
- Moy, C. M., G. O. Seltzer, D. T. Rodbell, and D. M. Anderson (2002), Variability of El Niño/Southern Oscillation activity at millennial timescales during the Holocene epoch, *Nature*, 420(6912), 162-165.
- Munk, W., and C. Wunsch (1998), Abyssal recipes II: energetics of tidal and wind mixing, *Deep-Sea Research Part I*, 45(12), 1977-2010.
- Oglesby, R. J., S. Feng, Q. Hu, and R. C. (2011), Medieval drought in North America: The role of the Atlantic Multidecadal Oscillation, *PAGES news*, 19(1), 18-20.
- Orsi, A., G. Johnson, and J. Bullister (1999), Circulation, mixing, and production of Antarctic Bottom Water, *Progress in Oceanography*, 43(1), 55-109.
- Park, J. (1992a), Envelope estimation for quasi-periodic geophysical signals in noise: A multitaper approach, *Statistics in the Environmental and Earth Sciences*, 189-219.
- Park, J. (1992b), Envelope estimation for quasi-periodic geophysical signals in noise: A multitaper approach, *Statistics in the Environmental and Earth Sciences*, 189-219.
- Park, W., and M. Latif (2008), Multidecadal and multicentennial variability of the meridional overturning circulation, *Geophysical Research Letters*, 35(22), L22703.
- Peltier, W. (2004), Global glacial isostasy and the surface of the ice-age Earth: the ICE-5G (VM2) model and GRACE, *Annu. Rev. Earth Planet. Sci.*, 32, 111-149.
- Poore, R. Z., K. L. DeLong, J. N. Richey, and T. M. Quinn (2009), Evidence of multidecadal climate variability and the Atlantic Multidecadal Oscillation from a Gulf of Mexico sea-surface temperature-proxy record, *Geo-Marine Letters*, 29(6), 477-484.
- Portig, W. (1965), Central American rainfall, *Geographical Review*, 55(1), 68-90.
- Prange, M., G. Lohmann, and A. Paul (2003), Influence of vertical mixing on the thermohaline hysteresis: Analyses of an OGCM, *Journal of Physical Oceanography*, 33(8), 1707-1721.
- Rühlemann, C., S. Mulitza, P. J. Müller, G. Wefer, and R. Zahn (1999), Warming of the tropical Atlantic Ocean and slowdown of thermohaline circulation during the last deglaciation, *Nature*, 402(6761), 511-514.
- Rühlemann, C., S. Mulitza, G. Lohmann, A. Paul, M. Prange, and G. Wefer (2004), Intermediate depth warming in the tropical Atlantic related to weakened thermohaline

circulation: Combining paleoclimate data and modeling results for the last deglaciation, *Paleoceanography*, 19(1).

Raddatz, T., C. Reick, W. Knorr, J. Kattge, E. Roeckner, R. Schnur, K. Schnitzler, P. Wetzel, and J. Jungclaus (2007), Will the tropical land biosphere dominate the climate–Carbon cycle feedback during the twenty-first century?, *Climate Dynamics*, 29(6), 565-574.

Rahmstorf, S., M. Crucifix, A. Ganopolski, H. Goosse, I. Kamenkovich, R. Knutti, G.

Lohmann, R. Marsh, L. Mysak, and Z. Wang (2005), Thermohaline circulation hysteresis: A model intercomparison, *Geophys. Res. Lett.*, 32, L23605.

Rasmusson, E. M., and T. H. Carpenter (1982), Variations in tropical sea surface temperature and surface wind fields associated with the Southern Oscillation/El Niño, *Mon. Wea. Rev.*, 110(5), 354-384.

Raynaud, D., J. Barnola, J. Chappellaz, T. Blunier, A. Indermöhle, and B. Stauffer (2000), The ice record of greenhouse gases: a view in the context of future changes, *Quaternary Science Reviews*, 19(1-5), 9-17.

Rayner, N., P. Brohan, D. Parker, C. Folland, J. Kennedy, M. Vanicek, T. Ansell, and S. Tett (2006), Improved analyses of changes and uncertainties in sea surface temperature measured in situ since the mid-nineteenth century: the HadSST2 dataset, *Journal of Climate*, 19(3), 446-469.

Renssen, H., H. Goosse, X. Crosta, and D. M. Roche (2010), Early Holocene Laurentide Ice Sheet deglaciation causes cooling in the high-latitude Southern Hemisphere through oceanic teleconnection, *Paleoceanography*, 25(3), PA3204.

Renssen, H., H. Sepp, O. Heiri, D. Roche, H. Goosse, and T. Fichefet (2009), The spatial and temporal complexity of the Holocene thermal maximum, *Nature Geoscience*, 2(6), 411-414.

Rimbu, N., G. Lohmann, J. Kim, H. Arz, and R. Schneider (2003), Arctic/North Atlantic Oscillation signature in Holocene sea surface temperature trends as obtained from alkenone data, *Geophysical Research Letters*, 30(6), 1280.

Rimbu, N., G. Lohmann, S. J. Lorenz, J. Kim, and R. Schneider (2004), Holocene climate variability as derived from alkenone sea surface temperature and coupled ocean-atmosphere model experiments, *Climate Dynamics*, 23(2), 215-227.

Roeckner, E., R. Brokopf, M. Esch, M. Giorgetta, S. Hagemann, L. Kornbluh, E. Manzini, U. Schlese, and U. Schulzweida (2004), The atmospheric general circulation model ECHAM5 Part II: Sensitivity of simulated climate to horizontal and vertical resolution, *Max-Planck-Institute for Meteorology, MPI-Report*, 354.

Roeckner, E., et al. (2003), The Atmospheric General Circulation Model ECHAM5. Part One: Model Description Report No.349, *Max Planck Institute for Meteorology*.

Rowell, D. P., C. K. Folland, K. Maskell, and M. N. Ward (1995), Variability of summer rainfall over tropical North Africa (1906-92): Observations and modelling, *Quarterly Journal of the Royal Meteorological Society*, 121(523), 669-704.

Russell, J., K. Dixon, A. Gnanadesikan, R. Stouffer, and J. Toggweiler (2006), The Southern Hemisphere westerlies in a warming world: Propping open the door to the deep ocean, *Journal of Climate*, 19(24), 6382-6390.

Saenko, O., A. Schmittner, and A. Weaver (2004), The Atlantic-Pacific seesaw, *Journal of Climate*, 17(11), 2033-2038.

Sallée, J. B., K. G. Speer, and R. Morrow (2008), Response of the Antarctic Circumpolar Current to Atmospheric Variability, *Journal of Climate*, 21(12), 3020-3039.

Sallée, J. B., K. G. Speer, and S. R. Rintoul (2010), Zonally asymmetric response of the Southern Ocean mixed-layer depth to the Southern Annular Mode, *Nature Geoscience*, 3(4), 273-279.

Sandweiss, D. H., J. B. Richardson, E. J. Reitz, H. B. Rollins, and K. A. Maasch (1996), Geoarchaeological Evidence from Peru for a 5000 Years B.P. Onset of El Niño, *Science*, 273(5281), 1531-1533.

Santoso, A., M. H. England, and A. C. Hirst (2006), Circumpolar deep water circulation and variability in a coupled climate model, *Journal of Physical Oceanography*, 36(8), 1523-1552.

Schewe, J., and A. Levermann (2010), The role of meridional density differences for a wind-driven overturning circulation, *Climate Dynamics*, 34(4), 547-556.

Schlesinger, M. E., and N. Ramankutty (1994), An oscillation in the global climate system of period 65-70 years, *Nature*, 367(6465), 723-726.

Schmittner, A., M. Latif, and B. Schneider (2005), Model projections of the North Atlantic thermohaline circulation for the 21st century assessed by observations, *Geophysical Research Letters*, 32.

Schubert, S. D., M. J. Suarez, P. J. Pegion, R. D. Koster, and J. T. Bacmeister (2004), Causes of long-term drought in the US Great Plains, *Journal of Climate*, 17(3), 485-503.

Screen, J. A., N. P. Gillett, D. P. Stevens, G. J. Marshall, and H. K. Roscoe (2009), The role of eddies in the Southern Ocean temperature response to the Southern Annular Mode, *Journal of Climate*, 22(3), 806-818.

- Sen Gupta, A., and M. H. England (2006), Coupled Ocean–Atmosphere–Ice Response to Variations in the Southern Annular Mode, *Journal of Climate*, 19(18), 4457-4486.
- Sen Gupta, A., and M. H. England (2007), Coupled Ocean–Atmosphere Feedback in the Southern Annular Mode, *Journal of Climate*, 20(14), 3677-3692.
- Sijp, W., and M. England (2008), The effect of a northward shift in the southern hemisphere westerlies on the global ocean, *Progress in Oceanography*, 79(1), 1-19.
- Sijp, W., and M. England (2009), Southern Hemisphere westerly wind control over the ocean's thermohaline circulation, *Journal of Climate*, 22(5), 1277-1286.
- Solomon, S., D. Qin, M. Manning, Z. Chen, M. Marquis, K. Averyt, M. Tignor, and H. Miller (2007), IPCC, 2007: Climate change 2007: The physical science basis. Contribution of Working Group I to the fourth assessment report of the Intergovernmental Panel on Climate Change, edited, New York: Cambridge University Press.
- Sowers, T., R. B. Alley, and J. Jubenville (2003), Ice core records of atmospheric N₂O covering the last 106,000 years, *Science*, 301(5635), 945.
- Speer, K., S. R. Rintoul, and B. Sloyan (2000), The Diabatic Deacon Cell*, *Journal of Physical Oceanography*, 30(12), 3212-3222.
- Spence, P., J. C. Fyfe, A. Montenegro, and A. J. Weaver (2010), Southern Ocean response to strengthening winds in an eddy-permitting global climate model, *Journal of Climate*.
- Straub, D. (1993), On the transport and angular momentum balance of channel models of the Antarctic Circumpolar Current, *Journal of Physical Oceanography*, 23(4), 776-782.
- Sutton, R. T., and D. L. R. Hodson (2005), Atlantic Ocean forcing of North American and European summer climate, *Science*, 309(5731), 115.
- Taylor, M. A., D. B. Enfield, and A. A. Chen (2002), Influence of the tropical Atlantic versus the tropical Pacific on Caribbean rainfall, *J. Geophys. Res.*, 107(C9), 3127.
- Thompson, D. W. J., and S. Solomon (2002), Interpretation of recent Southern Hemisphere climate change, *Science*, 296(5569), 895.
- Toggweiler, J., and B. Samuels (1995), Effect of Drake Passage on the global thermohaline circulation, *Deep Sea Research Part I: Oceanographic Research Papers*, 42(4), 477-500.
- Toggweiler, J., and B. Samuels (1998), On the ocean's large-scale circulation near the limit of no vertical mixing, *Journal of Physical Oceanography*, 28(9), 1832-1852.

Toggweiler, J., and J. Russell (2008), Ocean circulation in a warming climate, *Nature*, 451(7176), 286-288.

Toggweiler, J. R., and B. Samuels (1993), Is the Magnitude of the Deep Outflow from the Atlantic Ocean Actually Governed by Southern Hemisphere Winds?, *The Global Carbon Cycle*, M.Heimann, Ed.Springer, 333-366.

Treguier, A., J. Le Sommer, J. Molines, and B. De Cuevas (2010), Response of the Southern Ocean to the Southern Annular Mode: interannual variability and multidecadal trend, *Journal of Physical Oceanography*.

Turner, J., S. R. Colwell, G. J. Marshall, T. A. Lachlan-Cope, A. M. Carleton, P. D. Jones, V. Lagun, P. A. Reid, and S. Iagovkina (2005), Antarctic climate change during the last 50 years, *International Journal of Climatology*, 25(3), 279-294.

Valcke, S. (2006), OASIS3 User Guide (oasis3_prism_2-5), *PRISM Support Initiative Report No 3*, CERFACS, Toulouse, France. 64 pp.

Varma, V., M. Prange, F. Lamy, U. Merkel, and M. Schulz (2011), Solar-forced shifts of the Southern Hemisphere Westerlies during the Holocene, *Clim. Past*, 7(2), 339-347.

Vuille, M., R. Bradley, M. Werner, R. Healy, and F. Keimig (2003a), Modeling $\delta^{18}\text{O}$ in precipitation over the tropical Americas: 1. Interannual variability and climatic controls, *Journal of Geophysical Research*, 108(D6), 4174.

Vuille, M., R. Bradley, M. Werner, R. Healy, and F. Keimig (2003b), Modeling $\delta^{18}\text{O}$ in precipitation over the tropical Americas: 1. Interannual variability and climatic controls, *Journal of Geophysical Research*, 108(D6), 4174.

Waliser, D., and N. Graham (1993), Convective cloud systems and warm-pool sea surface temperatures- Coupled interactions and self-regulation, *Journal of Geophysical Research*, 98(D7), 12,881-812,893.

Wan, X., P. Chang, R. Saravanan, R. Zhang, and M. W. Schmidt (2009), On the interpretation of Caribbean paleo-temperature reconstructions during the Younger Dryas, *Geophys. Res. Lett.*, 36, L02701.

Wang, C., and S. Lee (2007), Atlantic warm pool, Caribbean low-level jet, and their potential impact on Atlantic hurricanes, *Geophysical Research Letters*, 34(2), 2703.

Wang, C., D. B. Enfield, S. Lee, and C. W. Landsea (2006), Influences of the Atlantic warm pool on Western Hemisphere summer rainfall and Atlantic hurricanes, *Journal of Climate*, 19(12), 3011-3028.

Wanner, H., J. Beer, J. Bütikofer, T. J. Crowley, U. Cubasch, J. Flückiger, H. Goosse, M. Grosjean, F. Joos, and J. O. Kaplan (2008), Mid-to Late Holocene climate change: an overview, *Quaternary Science Reviews*, 27(19-20), 1791-1828.

Wei, W., G. Lohmann, and M. Dima (2011), Distinct modes of internal variability in the Global Meridional Overturning Circulation associated to the Southern Hemisphere westerly winds, *Submitted to Journal of Physical Oceanography*.

Werner, M., M. Heimann, and G. Hoffmann (2001), Isotopic composition and origin of polar precipitation in present and glacial climate simulations, *Tellus B*, 53(1), 53-71.

Werner, M., P. Langebroek, T. Carlsen, M. Herold, and G. Lohmann (2011), Stable water isotopes in the ECHAM5 general circulation model: Towards high-resolution isotope modeling on a global scale, *J. Geophys. Res.*, (in press).

Winter, A., A. Paul, J. Nyberg, T. Oba, J. Lundberg, D. Schrag, and B. Taggart (2003), Orbital control of low-latitude seasonality during the Eemian, *Geophysical Research Letters*, 30, 1163, doi:10.1029/2002GL016275.

Wunsch, C. (1998), The work done by the wind on the oceanic general circulation, *Journal of Physical Oceanography*, 28(11), 2332-2340.

Wunsch, C., and R. Ferrari (2004), Vertical mixing, energy, and the general circulation of the oceans.

Xie, P., and P. A. Arkin (1997), Global precipitation: A 17-year monthly analysis based on gauge observations, satellite estimates, and numerical model outputs, *Bulletin of the American Meteorological Society*, 78(11), 2539-2558.

Zhang, R., and T. L. Delworth (2006), Impact of Atlantic multidecadal oscillations on India/Sahel rainfall and Atlantic hurricanes, *Geophys. Res. Lett.*, 33, L17712.

Zhang, R., and T. L. Delworth (2007), Impact of the Atlantic multidecadal oscillation on North Pacific climate variability, *Geophys. Res. Lett.*, 34, L23708.

Zhao, Y., P. Braconnot, O. Marti, S. Harrison, C. Hewitt, A. Kitoh, Z. Liu, U. Mikolajewicz, B. Otto-Bliesner, and S. Weber (2005), A multi-model analysis of the role of the ocean on the African and Indian monsoon during the mid-Holocene, *Climate Dynamics*, 25(7), 777-800.

Zhu, X., and J. Jungclaus (2008), Interdecadal variability of the meridional overturning circulation as an ocean internal mode, *Climate Dynamics*, 31(6), 731-741.